2022

DEVELOPMENT OF ADVANCED MODELS FOR PRE-IGNITION PREDICTION IN GAS ENGINES AND ANALYTICAL MODEL FOR WALLFILM EVAPORATION

Ankith Ullal
Michigan Technological University, ullal@mtu.edu

DEVELOPMENT OF ADVANCED MODELS FOR PRE-IGNITION PREDICTION IN GAS ENGINES AND ANALYTICAL MODEL FOR WALLFILM EVAPORATION

By

Ankith Ullal

A DISSERTATION

Submitted in partial fulfillment of the requirements for the degree of

DOCTOR OF PHILOSOPHY

In Mechanical Engineering-Engineering Mechanics

MICHIGAN TECHNOLOGICAL UNIVERSITY

2022

This dissertation has been approved in partial fulfillment of the requirements for the Degree of DOCTOR OF PHILOSOPHY in Mechanical Engineering-Engineering Mechanics.

Department of Mechanical Engineering-Engineering Mechanics

Dissertation Advisor: *Dr. Youngchul Ra*

Committee Member: *Dr. Chunpei Cai*

Committee Member: *Dr. Seong-Young Lee*

Committee Member: *Dr. Pradeep K. Agrawal*

Department Chair: *Dr. William W. Predebon*

Table of Contents

List of Figures vi

List of Tables xii

Author contribution statement xiii

Acknowledgements xiv

List of Abbreviations xv

Abstract xvi

1 Introduction 1

1.1 Literature survey 6

1.1.1 Pre-ignition 6

1.1.2 Wall film evaporation 9

2 Methodology and model development 11

2.1 Pre-ignition 11

2.1.1 Experimental and grid setup 12

2.1.2 Mixing fan model 13

2.1.3 Mesh refinement module 14

2.1.4 Refined mesh computations 18

2.1.4.1 Mass sharing 18

2.1.4.2 Transport effect 22

2.1.4.3 Combustion computations 23
2.1.4.4 Kernel initialization and flame propagation 23
2.1.5 Reaction mechanism 24
2.1.6 Overall workflow of SPIC model 26
2.1.7 SPIC model modifications for moving mesh 27
2.1.7.1 Snapping process 28
2.1.7.2 Rezone process 32
2.1.8 Lube oil film analysis 35
2.1.8.1 Lube oil film domain model 35
2.1.8.2 Lube oil film dynamics model 36
2.1.8.3 Lube oil stripping model 37
2.2 Wall film evaporation 39
2.2.1 Model setup and formulation 39
2.2.2 Unity Lewis number model 43
2.2.3 Non unity Lewis number model 46
2.2.4 Non unity Lewis number with correction 50
2.2.5 Energy balance equation 51
3 Results and discussions 53
3.1 Pre-ignition 53
3.1.1 Mixing fan simulation 53
3.1.2 Drop ignition 54
3.1.3 Effect of methane on ignition 56

3.1.4 Flame propagation 60
3.1.5 Gas injection 61
3.1.6 Oil film dynamics 72
3.1.6.1 Effect of initial film thickness.....78
3.1.6.2 Effect of initial film velocity.....79
3.1.7 Lube oil stripping.....83
3.1.8 SPIC model in engine 85
3.2 Wall film evaporation.....92

4 Conclusions.....105
4.1 Pre-ignition.....105
4.2 Wall film evaporation.....106

5 Future Work.....108
5.1 Pre-ignition.....108
5.2 Wall film evaporation.....109

References.....110

A Appendix: Calculation of $\boldsymbol{f\eta}$ and Lewis number 118
A.1 Calculation of $\boldsymbol{f(\eta)}$ 118
A.2 Calculation of Lewis number 121

List of Figures

Figure 1: Comparison of pressure profile between LSPI and normal cycle 3

Figure 2: Oil pre-ignition mechanism.....4

Figure 3: CVCC experimental and simulation setup with dimensions in cm.....13

Figure 4: Mixing fan region setup for center fan grid 14

Figure 5: Mesh refinement module.....15

Figure 6: a) Original parent hexahedral cell b) Level 1 refinement on parent cell.....18

Figure 7: a) Drop vapor sharing in refined cells b) Refined cell combustion calculation .23

Figure 8: a) Ignition delay for stoichiometric equivalence ratio b) Mechanism decomposition schematic 25

Figure 9: SPIC cycle workflow.....26

Figure 10: Grid snapping 27

Figure 11: Grid rezone 28

Figure 12: Refined cell snapping cases.....28

Figure 13: Parent (a) and refined cells (b) - case 3 snap operation.....31

Figure 14: Refined cell rezoning cases 34

Figure 15: Lube oil film domain model.....36

Figure 16: Oil film dynamics and evaporation model 37

Figure 17: Problem setup 40

Figure 18: a) Analytical temperature distribution, b) Analytical distribution of species-i mass fraction, c) Numerical domain temperature distribution d) Numerical domain distribution of species-i mass fraction 41

Figure 19: a) Flow velocity field produced by fan b), c) flow velocity field in more detail 54

Figure 20: a) drop simulated b) Experimental and c) simulation drop path and ignition comparison 55

Figure 21: Total accumulated vapor for various different equivalence ratios 57

Figure 22: a) Profiles of lube-oil density in the ignition subcell for different initial methane equivalence ratios. b) Variation of peak lube-oil and corresponding methane density with initial methane equivalence ratio 58

Figure 23: Reactivity of ignition cells (a) without, and (b) with lube oil vapor (with unity initial methane equivalence ratio). 59

Figure 24: Ignition time pattern on drop entering subcell for different initial methane conditions 60

Figure 25: Velocity vectors caused by the fan and gas injection 62

Figure 26: front and top views of a) Case 1 55 ms drop injection with drop velocity 2.53 m/s b) Case 2 60 ms drop injection with drop velocity 2.53 m/s c) Case 3 72 ms drop injection with drop velocity 5 m/s d) Case 1 refined and parent cell temperature vs time e) Case 1 refined and parent cell equivalence ratio f) Case 2

refined and parent cell temperature vs time g) Case 2 refined and parent cell equivalence ratio h) Case 3 refined and parent cell temperature vs time i) Case 3 refined and parent cell equivalence ratio 65

Figure 27: Flow field in plane of drop at injection a) adiabatic b) non-adiabatic 67

Figure 28: Drop path tracing a) front view b) top view at 66, 74, 80 82, 86 ms for non-adiabatic ignition case c) enlarged view showing flow and drop velocity at 82 ms 70

Figure 29: a) kernel growth after ignition b) flame speed after transition to turbulent flame propagation model c) turbulent kinetic energy plots in chamber at 95 ms d) turbulent kinetic energy plots in chamber at 116 ms e) Laminar flame speed f) ratio of turbulent to laminar flame speed vs time 71

Figure 30: flame surface tracking in chamber at a) 95 ms b) 105 ms c) 116 ms.....71

Figure 31: Grids used a) Isometric view b) Top view c) bottom view d) Cut section with crevice detail 73

Figure 32: Zoomed in view of oil film cell dynamics 74

Figure 33: a) velocity of piston and film (11,33) b) relative velocity of film with respect to piston.....76

Figure 34: a) Film thickness b) Film temperature vs CA 77

Figure 35: Effect of initial film thickness on a) film (11,33) thickness, b) relative velocity of film (10,33), c) relative velocity of film (11,33), d) film (11,33) temperature .79

Figure 36: Effect of initial film velocity on a) relative film (11,33) velocity, b) relative film (1,33) velocity, c) film (11,33) thickness, d) film (1,33) thickness, e) film (10,33) relative velocity, f) film (2,33) relative velocity 82

Figure 37: Effect of initial film velocity on film (11,33) temperature.....83

Figure 38: Critical angle vs CA for different initial film velocity of film (11,33) 84

Figure 39: Stripped parcel (not to scale) injection detail a) 3D grid, b) at cut plane y=0 .86

Figure 40: Cut plane y=0 distribution with parcel (black) of a) lube mass fraction b) parent cell temperature at -18° CA, c) lube mass fraction d) parent temperature at -9 ° CA, e) lube mass fraction b) parent cell temperature at -3° CA 88

Figure 41: Variation of a) injected parcel temperature b) injected parcel radius with crank angle.....88

Figure 42: a) Equivalence ratio b) Temperature variation of parcel-containing cell vs crank angle 90

Figure 43: Igniting parent cell (red legend) location in the chamber at 0 CA 90

Figure 44: Igniting refined cell temperature vs crank angle 92

Figure 45: Isometric and section views of a square channel with wallfilm.....93

Figure 46: Steady state velocity field in wallfilm containing x-z cut plane 93

Figure 47: a) Ambient temperature variation, b) Lewis number variation for NU-Le model.....95

Figure 48: a) Wallfilm surface temperature variation for NU-Le model, b) Wallfilm interior temperature variation for NU-Le model 95

Figure 49: Variation of properties used in Lewis number a) thermal conductivity, b) density, c) specific heat, d) diffusivity.....96

Figure 50: a) External heat flux for neat n-heptane, b) wallfilm surface and wallfilm interior temperature for neat n-heptane for NU-Le model.....97

Figure 51: a) External heat flux for neat iso-octane, b) wallfilm surface and wallfilm interior temperature for neat iso-octane for NU-Le model.....98

Figure 52: a) External heat flux of the 50nC7/50iC8 blend, b) External heat flux for comparison for NU-Le model.....98

Figure 53: Evaporation flux variation for NU-Le model.....99

Figure 54: a) External heat flux for tetradecane, b) Evaporation flux of tetradecane for NU-Le model 100

Figure 55: a) Lewis number variation of tetradecane for NU-Le model, b) External heat flux for tetradecane 102

Figure 56: a) External heat flux for flash boiling of neat n-heptane, b) Lewis number variation for flash boiling of neat n-heptane.....102

Figure 57: a) Evaporation flux of neat n-heptane flash boiling for NU-Le model, b) zoomed in view of (a) 103

Figure 58: a) Wallfilm interior temperature (T_f), wallfilm surface temperature (T_s), saturation temperature (T_{sat}) variation for flash boiling of neat n-heptane, b) zoomed in view of (a) 104

List of Tables

Table 1: Pre-burn mixture composition 12

Table 2: Lube-oil oxidation reactions in the reduced mechanism 25

Table 3: Ignition times for different equivalence ratios 56

Table 4: Gas injection parameters 61

Table 5: Ignition time with change in initial drop temperature 72

Table 6: Grid properties 74

Table 7: Initial composition of ambient gas 93

Table 8: wallfilm surface and wallfilm interior temperatures at 13 ms 96

Author contribution statement

The results presented in this work broadly fall into two categories. The first deals with pre-ignition phenomenon caused by lubricant oil drops. The work relating to this is published in the International journal of engine research. The citation details are given below.

Ullal, A., et al., *Numerical investigation of oil droplet combustion using single particle ignition cell model.* International Journal of Engine Research, 2021. **22**(5): p. 1465-1483.

Ullal, A. and Y. Ra, *Numerical study of lubricant oil drop induced pre-ignition in engines.* International Journal of Engine Research, 2022, *Manuscript accepted for publication.*

The second part is regarding the development of an analytical model for predicting the external heat flux to the gas-liquid interface. This work is published in the International journal of heat and mass transfer. The citation is as follows.

Ullal, A. and Y. Ra, *Analytical model for multicomponent wall film evaporation with non-unity Lewis number.* International Journal of Heat and Mass Transfer, 2021. **176**: p. 121485.

Acknowledgements

I would like to thank my advisor Dr. Youngchul Ra for giving me this opportunity to participate in the PhD research program at Michigan Technological University, providing financial support and guiding me throughout this work. The discussions and debates regarding research approach we had, helped me deepen my understanding in the subject.

The support from Ford Motor Company and Mitsubishi Heavy Industries both financially and in terms research of collaboration is highly appreciated.

I would like to acknowledge Dr. Chunpei Cai, Dr. Seong-Young Lee and Dr. Pradeep K. Agrawal for serving in my advisory committee and scrutinizing this work.

I also greatly appreciate and thank our research group members Arash Jamali, Oudumbar Rajput, Ashwin Karthik Purushothaman, Sai Prashanth Kumar and Hyejun Won for helping me in formulating ideas and having very insightful discussions. I did learn a lot from these sessions.

Last but not the least I thank my parents and family members for their constant and unwavering support.

List of Abbreviations

SPIC	Single particle ignition cell
RON	Research octane number
PDF	Probability density function
GDI	Gasoline direct injection
GCI	Gasoline compression ignition
CVCC	Constant volume combustion chamber
OF	OpenFoam
DPIK	Discrete particle ignition kernel
U-Le	Unity Lewis number
NU-Le	Non unity Lewis number
NU-Le-corr	Non unity Lewis number with correction
BDC	Bottom dead center
TDC	Top dead center
CA	Crank angle
LSPI	Low speed pre-ignition

Abstract

Ever-changing regulations aimed at improving efficiency and reducing harmful emissions have resulted in many power-generation device (engine) manufacturers to adopt new strategies. Computer simulation of these new strategies of power generation requires more accurate and higher fidelity modelling tools. In the present study, two such models are developed. The first model deals with pre-ignition phenomena driven by lubricant (lube) oil in natural gas engines and the second model is relevant to prediction of wallfilm evaporation by employing analytical solutions to transport governing equations for boundary layers.

Pre-ignition in engines has been the subject of current research with the advent of boosted engines for reduced fuel consumption and emissions. It can be caused by lube-oil drops or carbon deposits within the engine. A computational study of pre-ignition by lube-oil drops in a constant volume chamber and a production natural gas marine engine was done. For CFD simulations, an in-house version of KIVA4 code was used. Oil throw-off into the combustion chamber was modeled with an oil stripping model, in which the criteria for lube-oil drops to be stripped from the piston rings/crevice regions and enter the combustion chamber are calculated. To capture the timing of ignition caused by lube-oil drops precisely, single particle ignition cell (SPIC) model that utilizes grid refinement for drop containing cells was used. For modelling chemical kinetics, a reduced reaction mechanism for lube oil vapor oxidation was developed. Factors affecting lube-oil stripping and subsequent ignition processes were studied and discussed. Based on these studies

recommendations for possible mitigation strategies of pre-ignition in the marine engines are given.

For the new wallfilm model, an analytical expression for the external heat flux from ambient gases to the wallfilm-gas interface and the phase change rates at the interface are derived from first principles of transport phenomena. The model was coded into a computer program and applied to simulate transient evaporation of liquid wallfilms placed on the bottom wall of a square channel. Normal and flash boiling evaporation conditions were considered for various composition of the wallfilms. Simulation results are presented and the characteristics of phase change behavior are discussed.

1 Introduction

Energy consumption in the 21st century is predicted to grow further as more countries transition from developing to newly industrialized economies. Despite this growth, due to environmental concerns, there is a need to shift from conventional to cleaner energy generation and production methods. Energy generation and the transportation sector are looking to reduce their carbon footprint by transitioning to using less polluting or completely get rid of fossil fuels. This requires designing new machines and processes which can run or work on cleaner fuels. Often this process involves extra economic costs on research and development and take time to perfect. Part of the research and development costs include developing new and more accurate computer models of these newly designed processes. This also includes solving new problems that may arise from time to time.

In this work, new models for solving two such issues are developed. The first deals with a model for prediction of pre-ignition in natural gas engines. In the quest for increasing thermal efficiency, internal combustion (IC) engine manufacturers are leaning towards running downsized engines in boosted configuration. In addition to this, to comply with ever stringent emission regulations, cleaner fuels such as natural gas are replacing traditionally used diesel in high torque applications such as trucks and ships [1, 2]. Diesel engines dominate high torque engine applications such as those used in the trucking and marine industries. Marine engines also use more heavier and polluting fuel oil in addition to diesel. Natural gas as a fuel source has been gaining popularity in recent times due to its clean combustion characteristics. Natural gas engines are seen as an alternative to diesel engines as the latter has been the main culprit for increased soot and particulate matter

(PM) emissions. The marine industry has traditionally been lagging the trucking industry in terms of adapting natural gas. However, this trend is changing. According to a study by the International Maritime Organization (IMO) emissions caused by the shipping industry may lead to health risks for exposed populations mainly comprising of coastal areas [1]. In terms of economics, the price difference between natural gas and fuel oil has been decreasing steadily. The construction and improvement of natural gas infrastructure is expected to further decrease operating cost [1]. This has already led many newly constructed vessels to be run by natural gas. However, just as in spark ignition (SI) engines, natural gas engines are also prone to abnormal combustion events.

Abnormal combustion is detrimental to the life of an IC engine. Abnormal combustion in engines can be broadly categorized as knocking and pre-ignition. Knocking is associated with SI engines and happens when part of the fuel air mixture is burnt by end gas auto-ignition, instead of the flame initiated by the spark plug. Pre-ignition occurs when an ignition event is caused by a rogue ignition source such as fuel deposits, hotspots or oil droplets. It happens before the spark plug ignition event in the compression stroke, often causing rapid and high rise in pressure and temperature damaging the engine. This results in the engine trying to compress expanding gas, thus putting tremendous load on the piston and causes significant drop in engine output efficiency. It can damage engine components such as piston, connecting rods, bearings and spark plugs. **Figure 1** taken from Ref. [3] shows a comparison of the in-cylinder pressure for a normal and an abnormal cycle. The red pressure curve is a low speed pre-ignition (LSPI) event. Clearly seen in the figure is

the large increase in the cylinder pressure (indicated by ΔP) due to the pre-ignition, compared to the normal cycle range (indicated by grey).

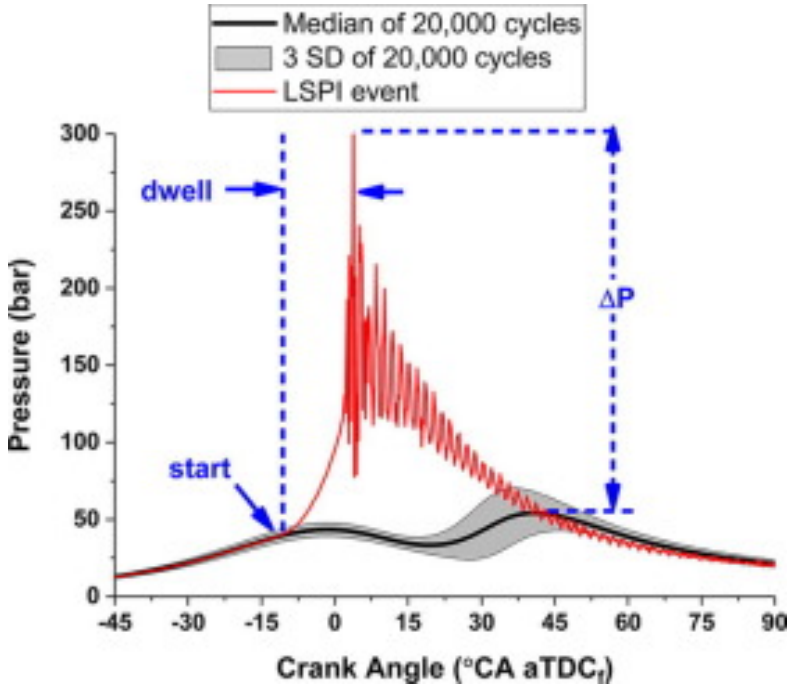

Figure 1: Comparison of pressure profile between LSPI and normal cycle

Oil is used as a lubricant for engines and can also act as a pre-ignition source. Recent experimental studies revealed that oil droplets that are released during the compression stroke are a possible source of pre-ignition [4]. Although the exact mechanism of pre-ignition is complex, it can be conceptually explained. As shown in **Figure 2**, lubricant oil mixtures (possibly diluted by fuel) are attached on the piston top-land during the compression stroke. When the piston is rapidly decelerating while moving up or accelerating while moving down, the oil is stripped from the piston walls due to its inertia with the help of gas flow though the piston ring gap. Disintegration of this oil strip forms oil droplets entrained into the charge mixture in the cylinder. Near the top dead center, the

in-cylinder gases are at high temperatures and help vaporize the oil droplets. Since the oil components are likely to be heavy hydrocarbons that have high reactivity, oil vapor can react easily to lead to ignition that initiates flame propagation in the ambient charge mixture. **Sec. 1.1.1** presents the literature survey and the novelty of model developed in this work.

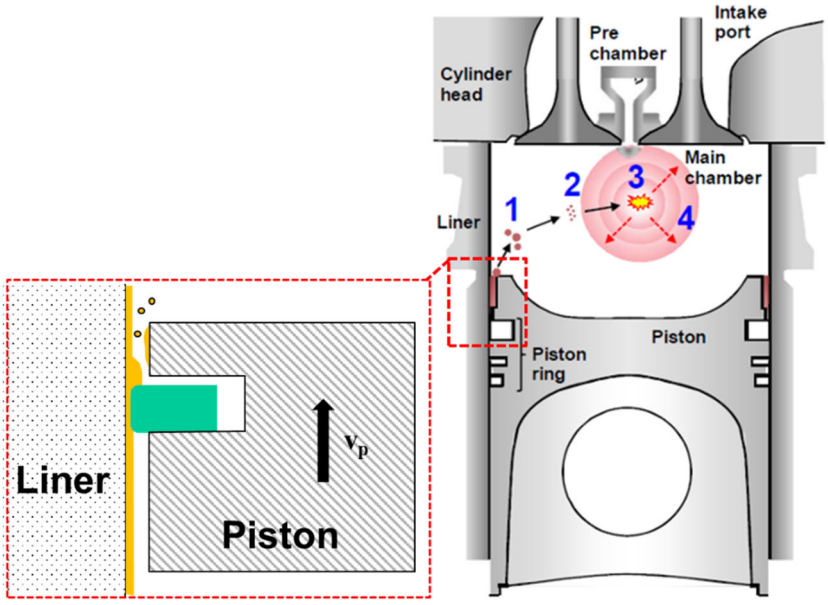

Figure 2: Oil pre-ignition mechanism

The second topic studied in this work is pertaining to the evaporation of wall films. Phase change of multi-component liquid film in air forms an important part of many engineering processes. Accurate understanding of the multiphase heat and mass transfer physics of phase change can result in efficient design and thereafter improved economics for these processes. Multicomponent liquid films are those films which contain a mixture of two or more pure liquid components. Few examples of these include gasoline, rubbing alcohol (iso-propyl alcohol + water), diesel, refrigerant R410a (50% CH_2F_2 + 50% CHF_2CF_3).

Wallfilm is formed when a liquid encounters and coats a solid surface. Practical examples of this are cooking oil poured into a hot pan, refrigerant/water flowing in condenser and boiler tubes, injected fuel droplets hitting the walls of a combustion chamber of both internal combustion and gas turbine engines [5-8]. Any machinery containing moving parts use lube oil for cooling and lubrication purposes. The moving parts, which are coated with lube oil are also examples of multicomponent wall-films [9-11]. Wallfilm physics involves heat and mass transfer characteristics of three phases namely – ambient gas, liquid film and solid surface. For the accurate prediction of the phase change rate and heat fluxes between phases, the interface (liquid and gas, solid and liquid) equations are coupled and to be solved simultaneously. For the liquid and vapor phases, these are conservation equations for mass, momentum (the Naiver stokes equation) and energy. It is well known among the academic community, analytically solving these equations without any simplifying assumptions are extremely difficult due to their nonlinear nature. In engine operation, injected fuel/oil can form a liquid film on the cylinder walls or piston surfaces. These films are exposed to surrounding hot gases due to which vaporization of liquid film takes place through heat transfer. Excessive wall film fuel can cause pool flame, which deteriorates engine performance and emissions. Most of the unburned hydrocarbons are produced by burning of these films. The accuracy of modelling emissions is thus dependent on the heat and mass transfer models used to model wallfilm physics. **Sec 1.1.2** looks at the literature survey on this topic.

1.1 Literature survey

In this section, the literature survey is done in two parts, the first focusing on the pre-ignition followed by the wall film evaporation. The novelty of the models developed in this work in comparison to the research already carried out is also explained in this section.

1.1.1 Pre-ignition

Zahdeh et al. [4] argued that the combustion of oil droplets is the leading theory of pre-ignition. They showed that there is a threshold end-of-compression temperature for the pre-ignition to occur and identified major parameters that have a direct and crucial role in the onset of pre-ignition, such as liner wetting, injection targeting, stratification, mixture motion and oil formulation, as well as secondary parameters including ring dynamics, ring tension, spark plug electrode temperature and coolant temperature.

Takeuchi et al. [12] and Fujimoto et al. [13] investigated the effects of oil formulation and its degradation on pre-ignition. They found that the auto ignition temperature of lubricant oil correlated well with pre-ignition frequency, indicating that the oxidation stability of the oil is a key factor to the pre-ignition propensity, and that the engine oil degradation increased the pre-ignition frequency. Based on their findings, Fujimoto et al. [13] showed that an optimal formulation of base oil and additives such as calcium-based detergent and anti-oxidants could reduce the pre-ignition frequency substantially. According to Park et al. [14] pre-ignition was also effected by fuel and lubricant type as well as coolant temperature. They compared 3 fuels (RON-90,92 and 95) with different lubricant grades for coolant temperatures of 50°C and 90°C respectively. They observed that RON-95 fuel

has higher propensity for pre-ignition when compared to RON-90 and RON-92. Coolant temperature of 50°C had comparatively more pre-ignition events. They also found that lubricants containing Ca, Zn and Mo have the greatest effect on the onset of pre-ignition. Kuboyama et al. [15] visualized the pre-ignition process using direct photography and light induced fluorescence imaging of lubricant oil droplets. They observed abnormal ignition caused by glowing particles and deposit fragments. They also observed luminous flame around the piston crevice during the exhaust stroke that is likely to be formed by burning of lubricant oil and fuel coming out of the crevice region during the expansion stroke and a potential source of the glowing particles. Although they found that the pre-ignition occurred mostly as a single-cycle event, they also observed sequential occurrence of pre-ignition and postulated the heating of the residual particles of the previous cycle during the subsequent cycle as a mechanism of multiple pre-ignition.

Pre-ignition also has shown dependence on air-fuel ratio. A rich mixture was found to reduce frequency of pre-ignition [4]. According to Amann et al [16], fuel composition also effects pre-ignition characteristics. Fuels with high levels of aromatics increase the likelihood of pre-ignition. In contrast oxygenated fuels with low level of aromatics reduced pre-ignition frequency.

Analyzing oil ignition experimentally is difficult as local fuel distribution and temperatures are to be monitored. Oil pre-ignition is still an area of current research and is often difficult to study due to its stochastic nature [17]. The location of pre-ignition is also deemed to be randomly distributed throughout the combustion chamber. The above mentioned studies indicate that pre-ignition is a complex phenomenon affected by many factors and chain of

events. Modeling tools can be used to supplement understanding of pre-ignition mechanism and fill in the gaps of experiments.

Recently, with improvement of computational capability, more attention has been being paid to numerical investigation of the onset of pre-ignition. For example, Lauer et al. [18] employed the 0-D stochastic reactor model with detailed chemistry, along with 3-D CFD simulations to obtain the initial particle PDF's of the reactor model. Based on the predicted chemistry of the oil/fuel droplets, they argued that the pre-ignition could be correlated with the first stage combustion of the oil drop. However, full 3-D CFD simulations of the pre-ignition event driven by either oil droplets or heated deposits in real engine geometries were not developed. Therefore, along with further experimental investigation, it is desirable to have a numerical tool to predict the occurrence of pre-ignition reliably that allows clarification of the detailed mechanism, and thus provide guidelines to improve the engine design to suppress/control the onset of pre-ignition.

Previous versions of the KIVA code employed various sub models for multicomponent liquid sprays in diesel/gasoline engines [19, 20]. These sub models use parcels to represent the properties of a bag of droplets. They are effective in simulation of sprays, where the number of liquid droplets is very large. However, pre-ignition by lube oil is likely to be caused by few drops. Having such a small number of drops in a large cell, artificially leans out the lube oil vapor, preventing accurate prediction of pre-ignition. New models are required for accurate CFD prediction of oil drop pre-ignition. As pre-ignition is dependent on local fuel and temperature conditions, mesh refinement feature is necessary to strike a chord between accuracy and computation time. To solve this a new single particle ignition

cell (SPIC) model is developed. It includes a mesh refinement module as well as its data handling routines which were added to the KIVA4 code, currently not available in the open source versions. For mesh refinement, a novel approach of using the refineMesh feature already available in OpenFOAM® (OF) within the KIVA4 code through inter-code communication was developed. A reduced chemical kinetics mechanism for lube oil was also developed. The newly developed routines were integrated and tested/validated with constant volume combustion chamber (CVCC) pre-ignition experiments. The SPIC model is also expanded to be used in engine grids. Oil film dynamics and stripping models are also implemented in the KIVA4-CFD code and conditions for lube oil stripping are investigated and a pre-ignition case is demonstrated.

1.1.2 Wall film evaporation

Various evaporation models have been considered for normal evaporation. The most basic formulation for wallfilm model is the Stefan problem as explained in Ref. [21]. It involves writing the energy balance equation for the gas phase at the vapor-liquid interface assuming equilibrium conditions. On considering diffusion of multicomponent species in the vapor phase leads to the Shvab-Zeldovich energy equations [21]. However, these equations assume thermal and mass diffusivity to be equal, i.e., unity Lewis number, to simplify the form of the governing equations. O'Rourke and Amsden [22, 23] proposed a wallfilm model which is widely used in numerical simulation of practical phase change application. They couple the effect of the liquid and gas phase by utilizing source terms in the numerical scheme. Zeng & Lee extended this approach further to multicomponent liquids [24]. They use a third order polynomial for temperature distribution in the liquid film, from which the

temperature gradient at the liquid-vapor interface is computed. In the extension of the same work further, Lee et al. [25] have modeled multicomponent wall-film evaporation using the continuous thermodynamics approach. To reduce computation cost, properties of multicomponent liquids are modeled with probability density functions. Yan et al. [26] have developed an unsteady wallfilm evaporation model considering the liquid film coupled with the vapor domain. However, they use correlations to calculate the convection coefficient for heat transfer to the vapor domain. Ra and Reitz [27] have investigated vaporization models for discrete multicomponent fuel drops, but their formulation did not consider the effect of Lewis number explicitly. Sazhin et al. [28] have used correlations for calculation of convective heat transfer coefficient in the gas phase. From this they consider the effect of Lewis number by obtaining the mass transfer coefficient using Chilton-Colburn analogy [29]. They have used analytical solutions which was slightly modified from Liye et al. [30] for solving the temperature distributions and multicomponent species distribution in the liquid film. Liu et al. [31] simplified the approach developed by Sazhin et al. for unity Lewis numbers. However, no work dealt with analytic expression for temperature and species distribution in boundary layer of the gas phase with non-unity Lewis number. Although the assumption of unity Lewis number simplifies the solution to the transport equations, it is not realistic and limits accuracy. Thus, there is a need to take into consideration the effect of fluid condition with non-unity Lewis number. This work attempts to obtain a generalized analytical solution with and without the unity Lewis number assumption. Simulations are also performed to demonstrate the performance of the model. In **Sec. 2**, the model formulation and computational setup are described.

2 Methodology and model development

In this section detailed description of the newly developed models is described in two sub-sections. **Sec. 2.1** deals with development relevant to pre-ignition prediction. Models such as Mixing fan model, which was developed to model the experimental setup considered in the validation simulations (not directly related to pre-ignition process) is also included in this section. All these models were implemented into an in house MTU-KIVA-4 CFD code. **Sec. 2.2** deals with the wallfilm heat transfer model; first, the description of the problem setup, and followed by the derivation of the analytic solutions to boundary layer equations for wallfilm external heat flux. The derivation is carried out in three sub-sections for, namely, i) a unity Lewis number model, ii) a non-unity Lewis number model, and iii) a model of non-unity Lewis number with correction. The new models were implemented to an in house MTU-KIVA-3V code.

2.1 Pre-ignition

A brief description of the experimental setup for which validation simulations are performed is explained in the first sub-section (**Sec. 2.1.1**). The knowledge of this setup helps understand the context for some of the models developed. Further, the model development process can be divided into two stages. The first step involves model development with respect to grids for stationary devices such as constant volume combustion chamber (CVCC). Once the models are implemented and validated for the stationary grids, certain modifications/upgradations needed for grids with boundary motion

(engine meshes), which is described in **Sec. 2.1.7**. In **Sec. 2.1.8** lube oil film setup and modification of models with respect to moving grids (engine meshes) are described.

2.1.1 Experimental and grid setup

The CVCC experimental setup used for validation simulations is shown in **Figure 3**, alongside with the equivalent computational grid and the dimensions of the fan region in centimeters. The dimension of the chamber is 10.63x10.63x10.63 cm^3. It consists of a fan (used for mixing) running at a constant speed of 5000 rev/min, which can be placed at the center or offset accordingly. In this work the fan is in the offset position as shown in **Figure 3**. The oil drop generator is placed at the center of the right wall. The gas injector is placed at center of the bottom wall. The initial composition (obtained from the experimental setup) before oil droplets are injected is a pre-burn mixture obtained by combustion of acetylene carried to obtain the initial pressure and temperature conditions before oil injection. The mixture composition is provided in **Table 1**. The average cell size (without refinement) was 2 mm. The number of cells and vertices were 95,085 and 101,528, respectively. Note that the shaft of the fan is solid and other parts are in the fluid domain.

Table 1: Pre-burn mixture composition

Composition	Mole fraction
O_2	0.19
N_2	0.66
CO_2	0.10
H_2O	0.05

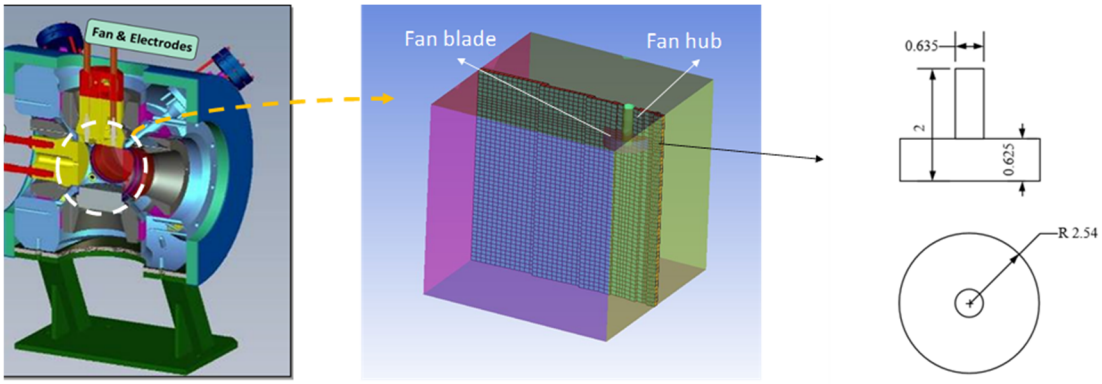

Figure 3: CVCC experimental and simulation setup with dimensions in cm

2.1.2 Mixing fan model

Along with the pre-burn mixture, the flow field generated by the fan must be simulated to match the experimental initial conditions. In simulations of the mixture conditions in the CVCC with methane direct injection and lube oil injection, the effects of mixing fan are deemed to be non-negligible. Since the gas flow over the moving fan blades is not resolved in the current simulations, the effects of continuous fan operation are modeled by modifying the flow velocity field to account for the fan-induced flow. This is done by identifying nodes in a local computational domain that corresponds to the region occupied by the rotating fan blades, as shown in **Figure 4**. Then, at every time step, the velocity of all the nodes enclosed within the volume of the fan region is numerically constrained to have a constant velocity that is equivalent to the flow rate induced by the fan in the velocity solver of the code. With the confinement, the rest of the flow field is calculated by the velocity field solver of the code (vsolve.f).

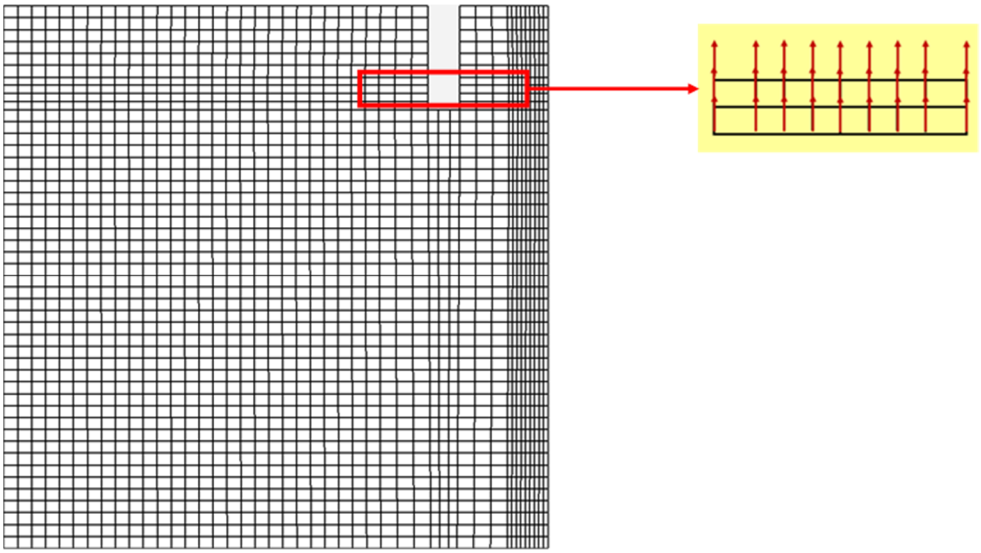

Figure 4: Mixing fan region setup for center fan grid

The number, location and dimensions of fan region are input by the user. The velocity components generated by the fan are specified based on the fan performance specification. In the model, the fan-induced velocities are fixed and not disturbed by flow change outside of the fan region. Due to this, the fan region plays a role of wall when a high-speed flow approaches the fan, which redirects the approaching flow around the fan region. The user-defined input of the model includes number of fan regions, dimension of fan regions (height and radius), position vector of fan locations (center of the bottom plane of the fan region) and three components of fan velocities in the cylindrical coordinate system.

2.1.3 Mesh refinement module

As discussed in **Sec. 1.1.1**, mesh cells containing the oil droplets must be refined. For this purpose, the mesh refinement module was developed. An overview flowchart of the refinement module is shown in **Figure 5**. The steps are elaborated below:

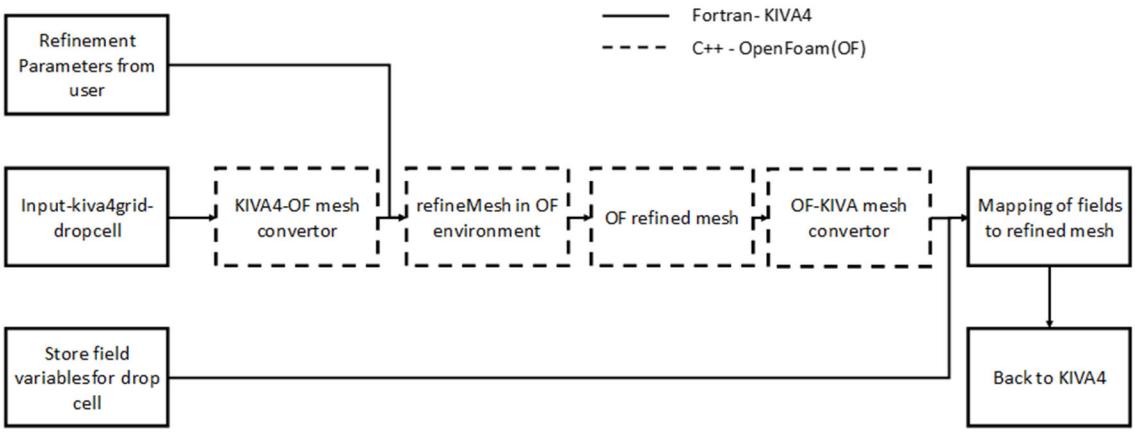

Figure 5: Mesh refinement module

1. Input from KIVA: For every cycle, initially, the cells containing oil droplets are identified to be sent to the refinement module. The mesh file (kiva4grid) containing the connectivity and coordinate information of its vertices is written in the KIVA working folder (run directory) for each cell containing or previously contained droplets. Note that refinement is done one cell at a time. The cell-centered field (pressure, temperature, internal energy, volume) variables of the parent cells are stored separately.

2. Refinement parameters (refinement level) are set by the user. For example, level 1 would generate 8 refined cells from 1 parent cell, level 2 would generate 64 refined cells from 1 parent cell and so on. Each of the created refined cells have the same volume.

3. Field variables of parent cells stored are required for generating field variables of refined cells through interpolation. This is explained in detail in point 8.

4. KIVA4-OF mesh convertor (kiva4ToFoam): As explained in the **Sec. 1.1.1** section, there is a requirement for communication of information between the KIVA program and OF. This is done by the KIVA4-OF mesh convertor. This convertor is coded in C++ in the OF

environment as indicated by the dashed box in **Figure 5**. The input here is the mesh information of the drop-containing or previously drop contained parent cell (kiva4grid). This mesh information is used to generate the unstructured mesh files used in OF format (points, owner, neighbor, boundary, faces).

5. OF mesh refinement: The OpenFoam mesh refinement feature refineMesh is used. The OF refineMesh uses Oct (one to eight cells) refinement concept. Ahmad Baniabedalruhman [32] discusses in detail regarding the working of refineMesh. Based on the number of times this module is run, the level of refinement can be adjusted (level 1, 2, ..., etc.). The output is the refined mesh in OF format (points, owner, neighbor, boundary, faces) which must be converted to KIVA4 format (kiva4grid).

6. OF-KIVA4 mesh convertor (foamToKiva4): This program reads in the OF refined mesh information and outputs the equivalent refined kiva4grid in the OF code working directory. Note that KIVA4 and OF codes are running in different directories. The refined mesh kiva4grid is then copied to the KIVA4 working directory.

7. Reading refined mesh: The refined cell mesh is read separately, and all connectivity information is stored. The running KIVA4 program has the mesh information of the original grid and the refined grid of the drop-containing parent cell.

8. Mapping fields to refined mesh: Linear interpolation is used to obtain the field values of refined grids. An example for level 1 refinement is explained. Consider a hexahedral cell shown in **Figure 6 (a)**. This undergoes level 1 (one to eight cells) cell refinement, shown after refinement in **Figure 6 (b)**. There are six neighboring cells designated as left (l), front (f), bottom (b), right (r), derriere (d) and top (t). For each of the eight subcells, three closest

neighbors (N1, N2, N3) are selected. For example, if the variable temperature T is considered, then the top-left-front subcell in **Figure 6(b)** (sub1) would have the three closest neighbors (top, left, front) with temperatures T_t, T_f, T_l. If T_c is the temperature of the center (parent) cell, then T_{sub1} is given by terms in **Eq. 1** and **Eq. 2**

$$T_{sub1} = \frac{1}{3}(T_{sub1t} + T_{sub1l} + T_{sub1f}) + \Delta T_{corr.} \quad \text{Eq. 1}$$

Where

$$\begin{gathered} T_{sub1t} = f_t T_c + (1 - f_t) T_t \\ T_{sub1f} = f_f T_c + (1 - f_f) T_f \\ T_{sub1l} = f_l T_c + (1 - f_l) T_l \\ f_t = \frac{d_{sub1t}}{d_{ct}}, f_f = \frac{d_{sub1f}}{d_{cf}}, f_l = \frac{d_{sub1l}}{d_{cl}} \end{gathered} \quad \text{Eq. 2}$$

d_{sub1t}, d_{sub1l}, and d_{sub1f} are the distance between center of top-left-front subcell and top, left, front cells, respectively. d_{ct}, d_{cl}, and d_{cf} are the distance between center parent cell and top, left, front cells, respectively.

$\Delta T_{corr.}$ is the temperature correction added to all subcells to ensure that the average of the temperatures of all subcells equals T_c. Once, the 8 refined cell temperatures are obtained ($T_1, T_2, T_3 \ldots \ldots T_8$), the expression for ΔT_{corr} is obtained from **Eq. 3** and **Eq. 4**.

$$8(T_c - \Delta T_{corr}) = \sum_{n=1}^{8} T_n \quad \text{Eq. 3}$$

$$\Delta T_{corr} = T_c - \frac{1}{8}\sum_{n=1}^{8} T_n \quad \text{Eq. 4}$$

Similarly, temperature and other fields are calculated for the remaining 7 subcells. This completes the mesh refinement module, and the control returns to the KIVA4 program which has the refined cell coordinates as well as interpolated field variables.

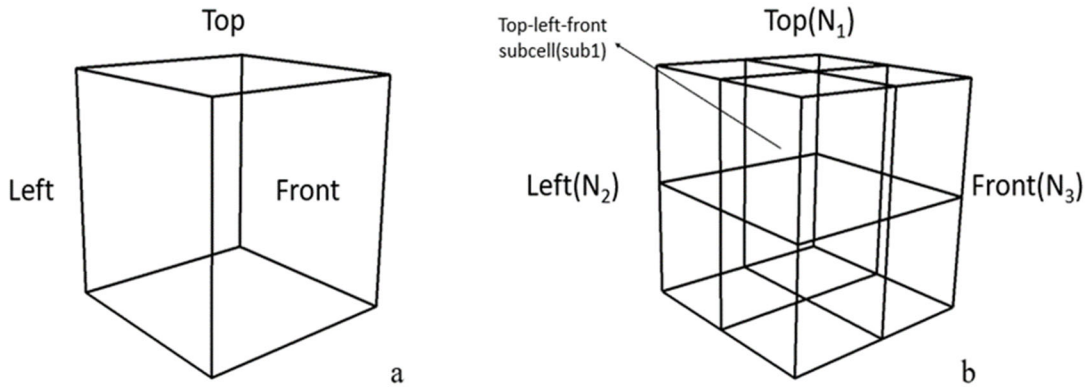

Figure 6: a) Original parent hexahedral cell b) Level 1 refinement on parent cell

2.1.4 Refined mesh computations

The evaporated mass from the drop/parcel is originally calculated in the subroutine evap.f [33]. This subroutine was modified to calculate the evaporated mass based on the refined cell conditions instead of the parent cells. The sharing of the evaporated mass among the subcells is handled by a newly added subroutine evap_refine.f. which is explained in the following sections.

2.1.4.1 Mass sharing

As mass diffusion equations are not solved at the refined cell level, a model is required for sharing of the evaporated mass among refined cells. Consider the steady state convection-diffusion equation in radial coordinates as shown in **Eq. 5**.

$$\frac{1}{r^2}\frac{d}{dr}\left(r^2\rho v y_f\right) = \frac{\rho\bar{D}}{r^2}\ \frac{d}{dr}\left(r^2\frac{dy_f}{dr}\right) \qquad \text{Eq. 5}$$

Where y_f is the fuel mass fraction, v is the velocity, ρ is the density of the mixture, $\bar{D}$ is the average diffusion coefficient.

Then $r^2\rho v = m_0$ for quasi-steady flow. On integration the expression for y_f is given by **Eq. 6**

$$y_f = \frac{y_{f,\infty} - y_{f,0}}{e^{-\frac{m_0}{\rho\bar{D}r_\infty}} - e^{-\frac{m_0}{\rho\bar{D}r_0}}}\left(e^{-\frac{m_0}{\rho\bar{D}r}} - e^{-\frac{m_0}{\rho\bar{D}r_0}}\right) + y_{f,0} \qquad \text{Eq. 6}$$

where the boundary conditions are at $r = r_\infty$, $y_f = y_{f,\infty}$ and $r = r_0$, $y_f = y_{f,0}$. Let the characteristic distance from the drop center by which fuel vapor is transported through diffusion be known as the radius of influence (r_{infl}). To calculate r_{infl} from **Eq. 6**, an assumption for the value of y_f at r_{infl} must be made. For example, if $r_{infl} = r_\infty$, then $y_f = y_{f,\infty}$. In **Figure 7 (a)**, the radius of influence is indicated by the orange circle. Once r_{infl} is obtained the volume enclosed by the sphere of influence can be calculated as V_{infl}. The neighboring cell volume is modeled as an equivalent sphere having volume V_{ngbr}. The intersection volume (V_{insct}) between the spheres V_{infl} and V_{ngbr} is calculated [34]. The mass present in the intersected volume represents the mass that should be shared with the neighboring cell. In three dimensions, this would amount to 27 cells (for level 2 refinement), including the center cells. Sharing is done if the intersection volume is above a certain minimum threshold value. Although r_{infl} provides us with the limit for sharing, it doesn't give information regarding the distribution of mass within the intersected volume. As a simplified model we assume a linear distribution. For simplicity in the

following illustration only the six cell neighbors – left, front, bottom, right, back, top is considered. Let m_{evap} be the total evaporated mass, and $V_1, V_2 \ldots . V_6$, and $f_1', f_2' \ldots f_6'$ be the intersection volume and mass distribution fraction of the neighboring cells, respectively. V_7 and f_7' be the volume and the mass distribution fraction of the drop containing cell. Then the expression for $f_1', f_2' \ldots f_7'$ is given by **Eq. 7** and **Eq. 8**.

$$f_1 = \frac{V_1}{d_1} C_{wt}, \qquad f_2 = \frac{V_2}{d_2} C_{wt}, \ldots \ldots , f_6 = \frac{V_6}{d_6} C_{wt} , f_7 = \frac{V_7}{d_7} \qquad \text{Eq. 7}$$

$$f_1 + f_2 \ldots . . f_7 = f_{tot}$$

$$f_1' = \frac{f_1}{f_{tot}}, f_2' = \frac{f_2}{f_{tot}}, \ldots . . f_7' = \frac{f_7}{f_{tot}}$$

$$C_{wt} = \min(1, k_1) \qquad \text{Eq. 8}$$

$d_1, d_2, \ldots, d_7$ are the distance from the drop to the cell centers, respectively. By varying k_1 between 0 and 1, the amount of sharing can be varied. For example, a special case of $k_1 = 0$, would be for no sharing between neighboring cells. The length scale calculated every cycle which is defined by the ratio of $\frac{D}{v_0}$, (where D is average diffusivity and v_0 is the Stefan flow convective velocity) was used as a gage to indicate if sharing is required or not. The corresponding evaporation cooling energy is subtracted from the internal energy of the drop containing subcell.

Adding mass to a subcell and its neighbors would increase their pressure. As transport equations are not solved for the refined cells, a model for equilibrating pressure within these subcells was developed and is explained in the following paragraph.

The local increase in pressure would cause mass diffusion. Let Δp be the pressure rise after pressure equilibrium is attained within the entire refined cell, which is the same for every subcell. Then, from the ideal gas law (**Eq. 9**) for each subcell the pressure rise Δp

$$\Delta p V_i = \Delta n_i R T_i \qquad \text{Eq. 9}$$

Where T_i is the subcell temperature, R is the universal gas constant, V_i is the sub cell volume and Δn_i is the increase in the number of moles of the i[th] subcell.

If, Δn_{totvap} is the moles of fuel vapor added, then it is calculated as given in **Eq. 10** and **Eq. 11**

$$\Delta n_{totvap} = \sum_{i=1}^{N} \Delta n_i \qquad \text{Eq. 10}$$

where N is the total number of subcells.

Since the volume of every subcell is the same from the refinement algorithm $V_1 = V_2 = \cdots V_{sub}$

$$\Delta n_{totvap} = \frac{\Delta p V_{sub}}{R} \sum_{i=1}^{n} \frac{1}{T_i} \qquad \text{Eq. 11}$$

If $\frac{\Delta p V_{sub}}{R} = \tilde{C}$ then **Eq. 11** is simplified to **Eq. 12**

$$\tilde{C} = \frac{\Delta n_{totvap}}{\sum_{i=1}^{n} \frac{1}{T_i}} \qquad \text{Eq. 12}$$

From **Eq. 9**, expression for Δn_i is simplified to Eq. 13

$$\Delta n_i = \frac{\tilde{C}}{T_i} \qquad \text{Eq. 13}$$

This Δn_i is added to every subcell. Note that the fuel is not distributed in this process to other cells as fuel sharing algorithm already takes account of this. For each subcell the redistributed species is proportional to that species mole fraction.

For the subcell calculations to be reflected in the parent cell, they must be coupled. The new mass fraction for all species which is calculated from the subcells is multiplied to the parent (par) cell species density as in **Eq. 14** and **Eq. 15**.

$$\rho_{par,isp} = \rho_{par} \times y_{isp} \qquad \text{Eq. 14}$$

and

$$y_{isp} = \frac{\sum_{sub=1}^{64} \rho_{sub,isp} V_{sub}}{\sum_{isp=1}^{n} \sum_{sub=1}^{64} \rho_{sub,isp} V_{sub}} \qquad \text{Eq. 15}$$

where $\rho_{par,isp}$ is the updated parent cell density for species isp, ρ_{par} is the overall parent cell density. $\rho_{sub,isp}$ is the subcell density for species isp and V_{sub} is the subcell volume.

2.1.4.2 Transport effect

The transport equations are not solved for the subcell. Thus, the transport equations solved at the parent cell level must be reflected in the subcell. This is carried out in the KIVA subroutine state.f at the end of every cycle. The difference in the field variables (internal energy, species density) of the parent cell before and after solving the transport equations are evenly distributed within all the subcells of the respective parent cell.

2.1.4.3 Combustion computations

For each of the subcells, of a drop containing parent cell, combustion calculations are performed. A separate subroutine (chem_para_AMR.f) was developed to handle this task. The subroutine is based on CHEMKIN library [35]. Combustion calculations at the refined level are applied to drop-containing subcells as well as those subcells through which the drops have traversed. For example, in **Figure 7 (b)**, parent cell no. 3 contains the droplet after passing through cell 1 and 2. In this case combustion calculations will be performed for parent cells 1, 2 and 3. If level 2 refinement is chosen this would result in combustion calculations for 192 subcells.

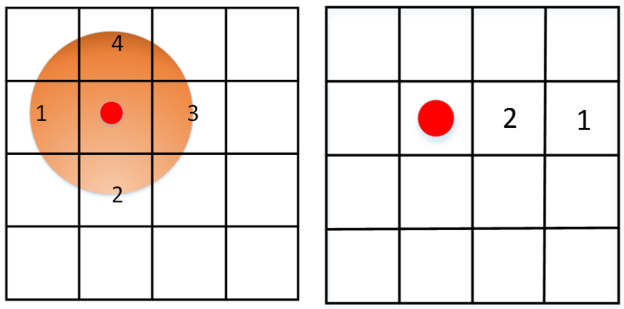

Figure 7: a) Drop vapor sharing in refined cells b) Refined cell combustion calculation

2.1.4.4 Kernel initialization and flame propagation

To determine ignition, an ignition criterion must be set. 2000 K is high enough temperature, which when attained lube oil vapor will ignite. If for example, a lower temperature such as 1000K is taken as an ignition criterion, depending on conditions favorable for ignition, the temperature may increase and eventually reach 2000K or die down (not reach) and eventually not ignite. In this case it would be erroneous to consider 1000 K as ignition

criterion. Thus, a high temperature value such as 2000K is chosen as reference for ignition criterion. Refined cell calculations are discontinued at this point. The center of the ignited subcell is considered as the point for kernel initiation. The DPIK model [36] is used to calculate the kernel growth rate. After ignition kernel exceeds a critical diameter, the ignition model is switched to a flame propagation model [37].

2.1.5 Reaction mechanism

A 129 species and 559 reaction reduced mechanism for $C_{21}H_{44}$ was extracted from Ra at. al [38] and used to model lube-oil oxidation. In the mechanism, the generic reaction method [39] is employed to describe the reaction paths from lube-oil to n-hexadecane and n-hexadecyl radicals. The reaction rate constants of these reactions were adjusted to capture the reactivity of lube oil, considering typical lube-oil contains hydrocarbons heavier than C_{21}. **Table 2** shows the lube oil reactions and **Figure 8 (b)** shows the decomposition schematic. The mechanism takes into consideration the multicomponent kinetics effect [40]. A case study of this is presented below using natural gas (methane) and lube oil. A homogenous reactor using the CHEMKIN [35] tool was used for this study. The input fuel (methane + lube) equivalence ratio was stoichiometric with the percentages between the two varied to demonstrate the multicomponent effect. Note that methane being the shortest hydrocarbon has low reactivity, on the other hand lube oil being heavy hydrocarbon has high reactivity. The percentages of methane were varied from 100 % to 0 % with the remaining being lube. **Figure 8 (a)**, shows the ignition delay results for these cases. The reactivity difference between methane and lube oil is evident from the large difference in their respective ignition delay times. The blending percentage effects the ignition delay

times non-linearly. From a kinetics perspective, increasing methane percentage suppresses reactivity of the fuel. This is caused due to competition for consumption of OH radical. Ra et al. [40] have explained this effect with syngas (lower reactivity) and n-heptane (higher reactivity) in their paper. Similar analogy can be applied to the methane-lube oil case.

Table 2: Lube-oil oxidation reactions in the reduced mechanism

1. lube+h=c16h33+c2h4+c3h6+h2
2. lube+h=c16h34+c5h11
3. lube+oh=c16h33+c2h4+c3h6+h2o
4. lube+oh=c16h34+c4h9+ch2o
5. lube+ho2=c16h33+c2h4+c3h6+h2o2
6. lube+ho2=c16h34+c4h9+hco+oh
7. lube+o2=c16h33+c2h4+c3h6+ho2
8. lube+o2=c16h34+c4h9+hco+o
9. lube+o=c16h33+c2h4+c3h6+oh
10. lube+o=c16h34+c4h9+hco
11. lube=c16h33+c5h11

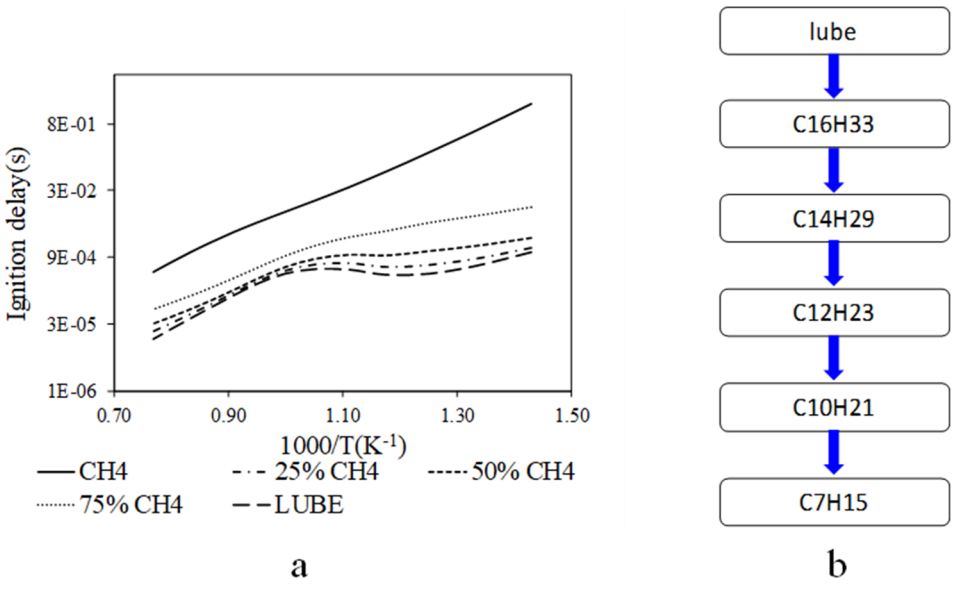

Figure 8: a) Ignition delay for stoichiometric equivalence ratio b) Mechanism decomposition schematic

2.1.6 Overall workflow of SPIC model

Figure 9 shows the overall workflow sequence employing all the models developed for a simulation cycle. A typical SPIC cycle begins with tracing the drop containing cells. If all subcell temperatures are below 2000 K (ignition criteria), which indicates that no ignition is reached in the current cycle, the SPIC model is continued with the next cycle. On the other hand, if the temperature of at least one subcell reaches 2000 K, the center of that subcell is chosen as the initial location of ignition kernel. At this point, the SPIC model (refined cell) calculations are stopped.

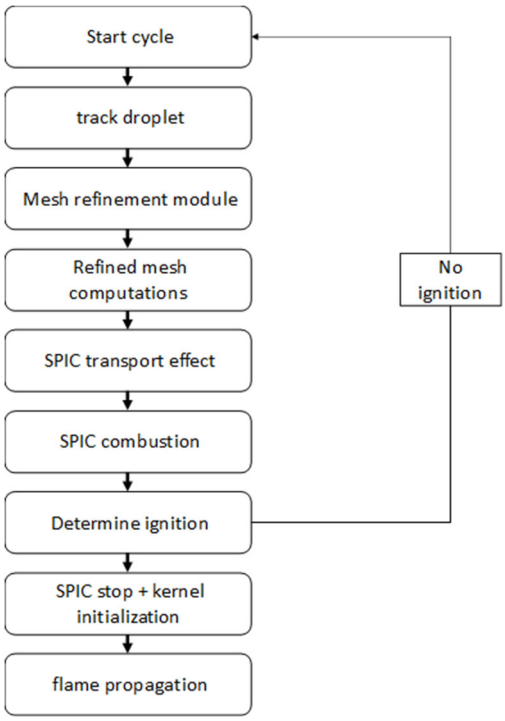

Figure 9: SPIC cycle workflow

2.1.7 SPIC model modifications for moving mesh

Engine grid simulations employ moving mesh techniques and operations. In KIVA, these include grid snapping and rezone [41]. Grid snapping involves removal and addition of bottom cell layers just above the piston surface as it moves up and down respectively. Thus, this operation changes the number of active cells in the computational domain. Rezone (accordion method) redistributes the layers of the cell along the moving direction (z), keeping the number of layers and cells the same. **Figure 10** shows removal and addition of cell layers as part of snapping operations. **Figure 11** shows the grid before rezone and after rezone operation. Both these grid modification operations must be reflected in the refined cell data.

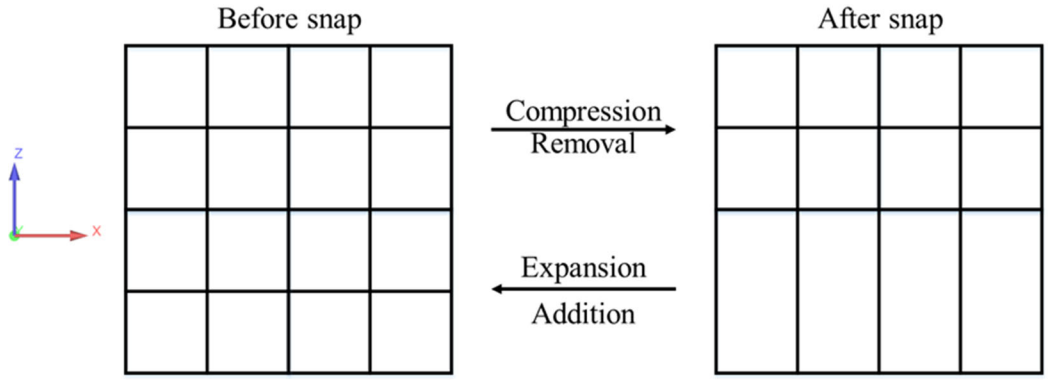

Figure 10: Grid snapping

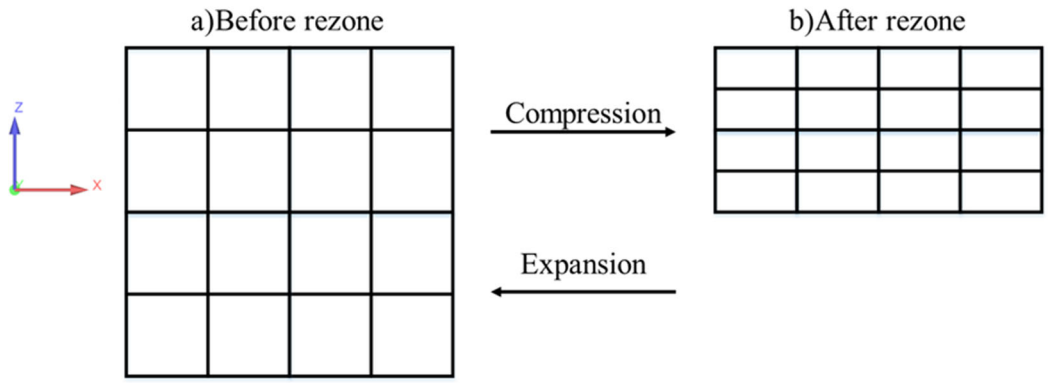

Figure 11: Grid rezone

2.1.7.1 Snapping process

Snapping operations consist of removal of a single layer of cells at a time during the compression stroke and addition of the same layer during the expansion stroke.

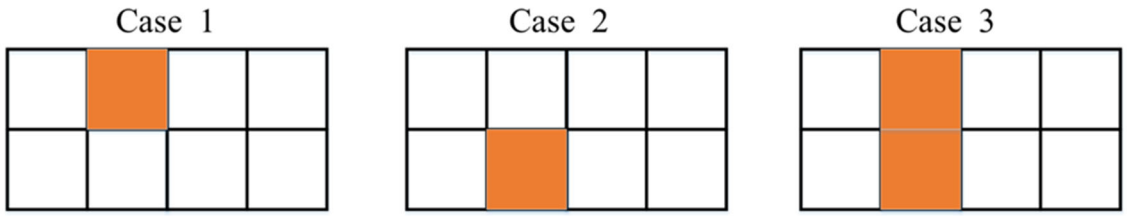

Figure 12: Refined cell snapping cases

In the context of engine simulation, removal of a layer of cells above the piston surface takes place on satisfying the snapping criteria. This implies two of the bottommost cell layers above the piston are combined to form a single layer (**Figure 10**). In the SPIC model, the cells through which the droplet has traversed are refined and this information is stored for the subsequent cycles. This refined cell array size needs to be updated if any of the drop traversed cells lie in the bottom 2 layers above the piston surface as these cells are going to be merged. This can occur in 3 cases as shown in **Figure 12**. The orange color

indicates that these parent cells have been refined earlier (lube drops have traversed these cells). For case 3, the total number of parent cells traversed by the drop need to be reduced by 1. Consequently, the refined cells must also be correspondingly reduced. For example, in case 3, after snapping for refinement level of 2, the total number of refined cells decrease by 64. In case 1 and 2, they would remain the same. The new parent cell after snapping operation is sent for refinement again, and the new coordinates are updated. The new cell centered values of variables such as specific internal energy, pressure, turbulent kinetic energy, dissipation rate and species density after snapping must be calculated. This can be done in two ways, namely simple and spline mapping. The first method is by simple mapping. In **Figure 13 (b)**, for instance, if specific internal energy (U) is taken as an example for a cell centered variable. Then after snapping operation, the specific internal energy for cell indices 1 & 5 are obtained as in **Eq. 16** & **Eq. 17**.

$$\rho_{1,a}V_{1,a}U_{1,a} = \rho_{1,b}V_{1,b}U_{1,b} + \rho_{5,b}V_{5,b}U_{5,b} \quad \text{Eq. 16}$$

$$\rho_{5,a}V_{5,a}U_{5,a} = \rho_{9,b}V_{9,b}U_{9,b} + \rho_{13,b}V_{13,b}U_{13,b} \quad \text{Eq. 17}$$

The subscript- $1,a$ indicates the 1st cell index after snapping. Similarly, $1,b$ indicates the 1st cell before snapping. ρ and V indicate the cell density and volume, respectively. For case 2 (**Figure 12**), both $U_{1,a}, U_{5,a}$ are initialized with the corresponding parent cell values. Similarly, for case 1 (**Figure 12**) $U_{9,a}, U_{13,a}$ are initialized with the corresponding parent cell values.

For the second method of spline mapping, new cell values are obtained by using the cubic spline interpolation in the z direction. For example, consider **Figure 13 (b)**. Let $z_{1,b}$, $z_{5,b}$, $z_{9,b}$ .... be the z coordinates of the subcell centers before snapping of subcells 1, 5, 9 .... The

properties namely specific internal energy (U), density (ρ), turbulent kinetic energy (k), dissipation rate (ε), at these points are used to generate the spline interpolated values at $z_{1,a}$ (z coordinate of cell 1 after snapping) after snapping. In order to ensure conservation of the cell centered values, the after snapping cell values are corrected in a similar method as explained in Ref. [11]. In this work, spline mapping is used as simple mapping has low accuracy when the resolution of the bottommost two cell layers above the piston are different.

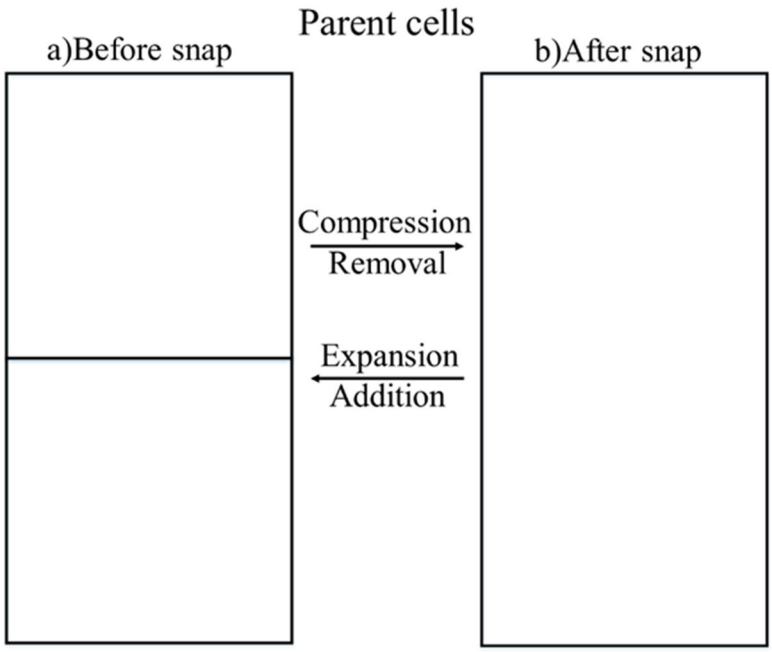

a

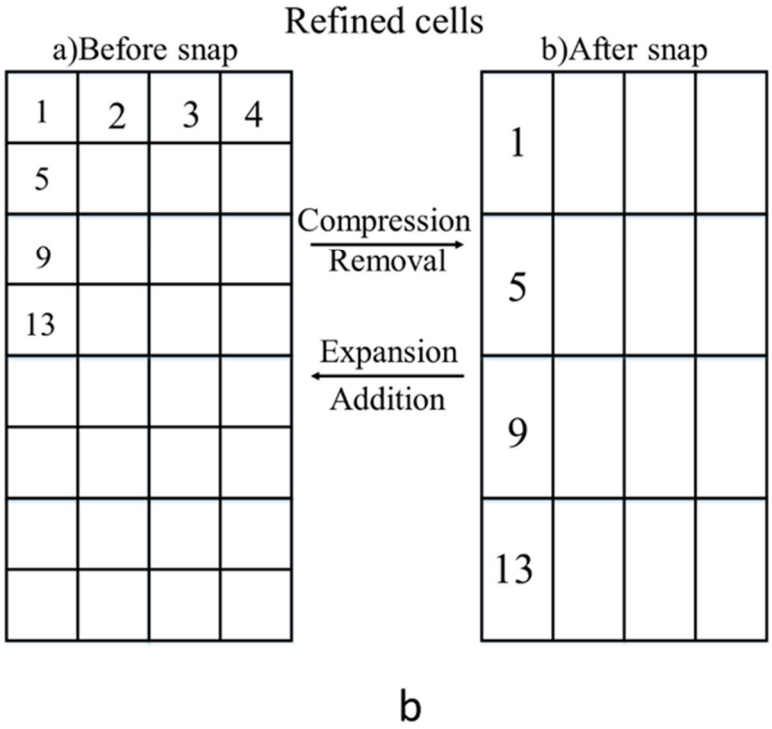

b

Figure 13: Parent (a) and refined cells (b) - case 3 snap operation

After removing a layer of cells, the drop-containing cell index changes, and thus needs to be updated. Spline mapping can similarly be used for cases 1 & 2 when only one of the cells are refined.

When the piston is moving down during the expansion stroke, the resolution is gradually increased. This implies cell layers must be added. The refined cell array in this case is thus increased accordingly. Consider the same example shown in **Figure 13**. For simple mapping, the properties specific internal energy (U), density (ρ), turbulent kinetic energy (k), dissipation rate (ε) are updated as shown in **Eq. 18**

$$\rho_{1,b} = \rho_{1,a} = \rho_{5,a}, U_{1,b} = U_{1,a} = U_{5,a}, k_{1,b} = k_{1,a} = k_{5,a}, \varepsilon_{1,b} = \varepsilon_{1,a} = \varepsilon_{5,a} \quad \text{Eq. 18}$$

Spline mapping can similarly be applied as explained in the piston moving up case.

2.1.7.2 Rezone process

The rezone behavior shown in **Figure 11**, is to be reflected in the refined cells. Since rezone adjusts the z coordinates of all the parent cells, the z coordinates of the corresponding refined cell are also adjusted. For non-drop-containing cells the changes associated with the rezoned parent cells are evenly distributed among the refined cells. However, for drop-containing cells, a model needs to be developed for redistribution of fuel vapor. The case where a drop shifts among refined cells due to rezoning of parent cell is shown in **Figure 14.** The source and target cells are identified. The source cell is the cell which contained the drop before rezone. Target cell is the cell to which the drop shifts after rezone. These cells are noted. If the source cell is denoted as C_1 and the target cell as C_2, then for case 1

and case 2 (**Figure 14**), the properties for internal energy are updated as shown in **Eq. 19** and **Eq. 20**

$$U_{c1new} = w_1 U_{c1} + w_2 U_{c2} \quad \text{Eq. 19}$$

$$U_{c2new} = w_2 U_{c1} + w_1 U_{c2} \quad \text{Eq. 20}$$

where w_1 and w_2 are weighting functions such that their sum equals unity. If n_{si} is the initial number of drops in the source cell and n_{sf} is the number of drops in the source cell after rezone, then w_1 and w_2 are calculated as shown in **Eq. 21** and **Eq. 22**

$$w_1 = \frac{n_{sf}}{n_{si}} \quad \text{Eq. 21}$$

$$w_2 = 1 - w_1 \quad \text{Eq. 22}$$

Other quantities are updated similarly. For case 3, where in the target cell is an unrefined cell (drop never entered this cell), it is now added to the list of refined cells. This would encompass calling the refinement routine, including interpolation of properties from neighboring cells [11]. After this, similar operations as used for case 1 and 2 are carried to modify the source and target properties.

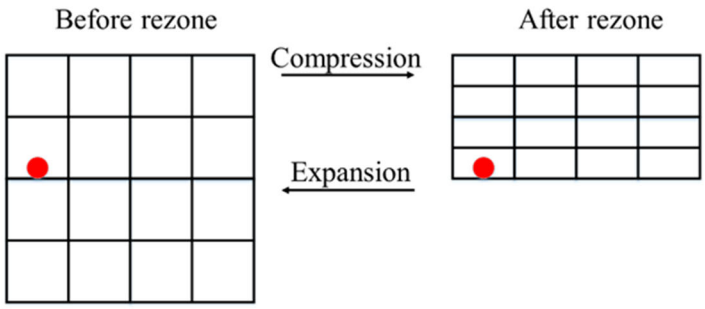

Case 1: Drop stays within the same parent cell

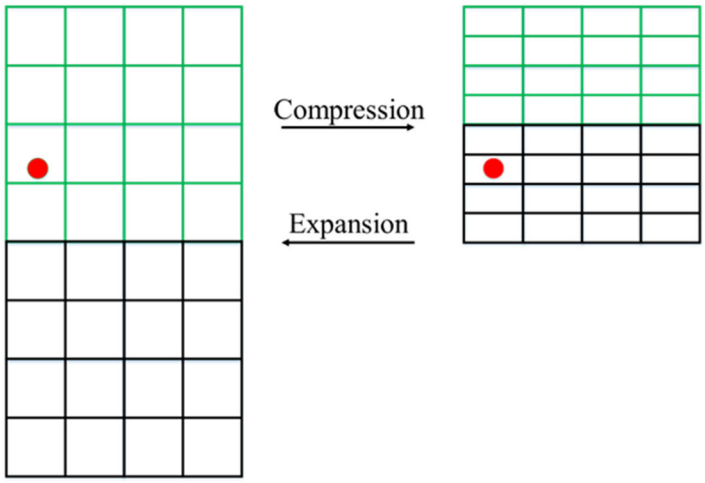

Case 2: Drop moves to a new refined parent cell

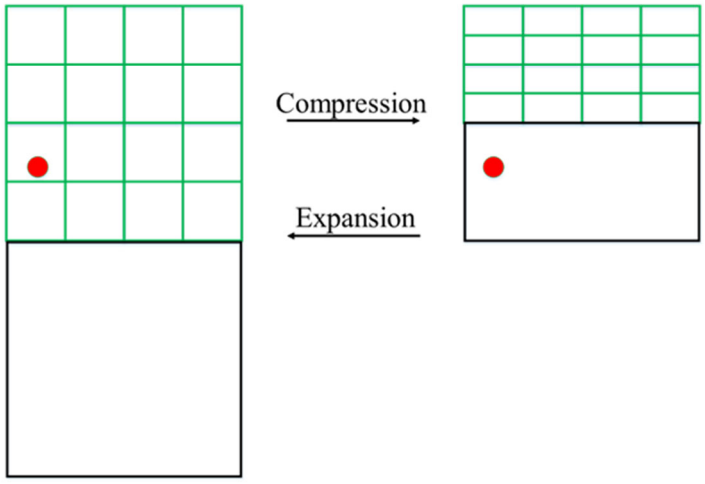

Case 3: Drop moves to a new unrefined parent cell

Figure 14: Refined cell rezoning cases

2.1.8 Lube oil film analysis

In engines, the cylinder liners and piston skirts contain a lubricating layer of oil to prevent metal to metal contact. They are lubricated and can be the source of rogue oil droplets being stripped which can induce pre-ignition as mentioned in the introduction section. Thus, various models are required to predict oil film dynamics, oil film stripping, vaporization and heat transfer which is explained in this section.

2.1.8.1 Lube oil film domain model

The KIVA4 code uses a snapping technique for moving boundaries that deletes a layer of cells in the middle of the numerical grid during the compression stroke and adds a layer of cells at the bottom of the grid during the expansion stroke. In the existing version of the CFD code, this makes it difficult to track and monitor the change of lube-oil film conditions on the cylinder walls during the calculation if those values are assigned to and stored in the KIVA numerical grid. This is because the information assigned to cells are lost when the cells are deactivated or no previous information exists when the cells are newly activated. To resolve this difficulty, separate computational domains where oil film dynamics, heat and mass transfer and phase change occur were built. As shown in **Figure 15**, two oil film domains are generated at the beginning of the computation in a two-dimensional coordinate system: one for the cylinder liner and the other for the piston topland. The piston domain is modeled to move with piston motion, i.e., the entire domain remains active during the simulation, while the unexposed/newly-exposed parts of the liner domain are deactivated/activated as piston moves up/down.

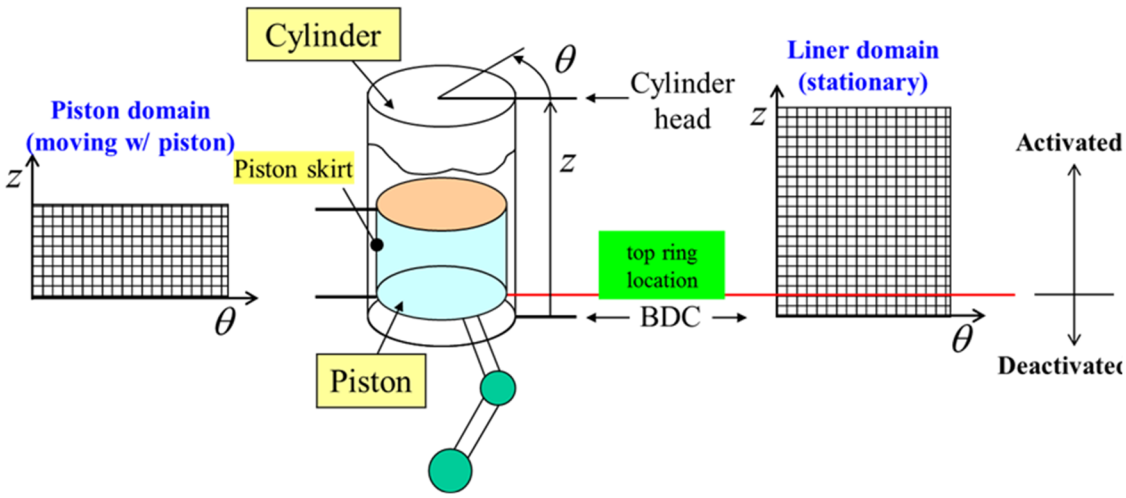

Figure 15: Lube oil film domain model

The oil-film domain is initialized at the start of the compression stroke according to an appropriate distribution obtained from experimental measurements or other estimations. Also, at the start of the expansion stroke, the oil-film on the liner domain is re-initialized to a fixed thickness and temperature, except for the region that is exposed to the cylinder gas at that time and the region corresponding to the oil-ring gap. The resolution of the oil domain can be different from the KIVA computational domain. A mapping technique is used for connecting the properties between the two domains.

2.1.8.2 Lube oil film dynamics model

The wall film dynamics model was implemented to solve oil-film motion on the oil-film domains. Using the gas and piston velocities as boundary conditions, and the lube-oil addition as the source terms of mass and momentum, the mass and momentum conservation equations are solved in the vertical direction only, neglecting motions in the azimuthal direction [22, 23]. It is modeled that lube-oil is accumulated in the top-end cells

in the piston oil-film domain such that lube-oil is stripped when the accumulation exceeds a threshold value, as shown in **Figure 16**.

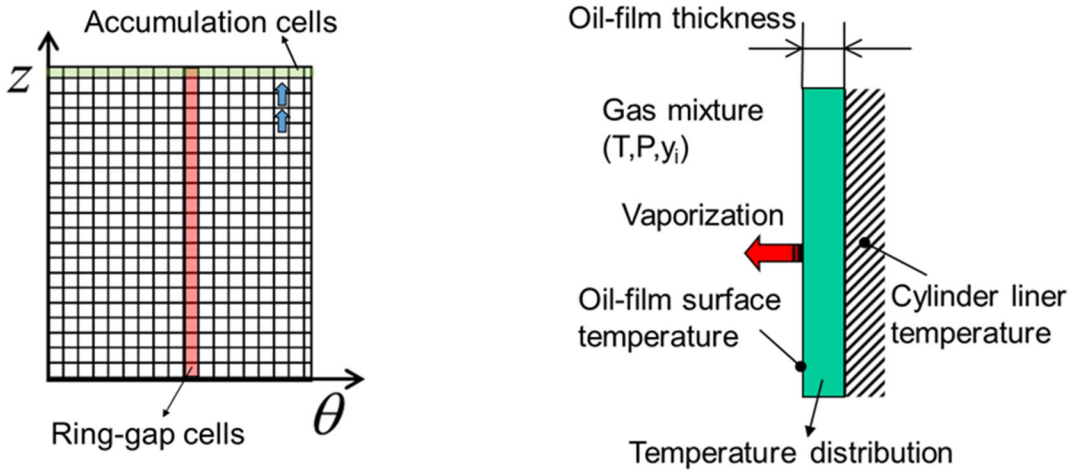

Figure 16: Oil film dynamics and evaporation model

2.1.8.3 Lube oil stripping model

Maroteaux et al. [42] has studied the factors which lead to stripping conditions of fuel (dodecane) using Rayleigh-Taylor instabilities. Specifically, they looked at liquid film atomization on sharp edges. For a disturbance $\delta(x,t) = \delta_o e^{(ikx+\omega t)}$, the disturbance growth rate (ω) is given by the dispersion equation **Eq. 23**.

$$\omega = \left(\frac{\sigma - \left({}^{\Delta\rho a}/_{k^2}\right)}{2\mu_l h}\right)\left(\frac{(kh)\,sinh(kh)\,cosh(kh) - k^2h^2}{cosh^2(kh) + k^2h^2}\right) \qquad \text{Eq. 23}$$

where $\Delta\rho = \rho_l - \rho_g$ is the difference in densities of liquid and gas, a is the acceleration applied to the liquid film, μ_l is the viscosity of the liquid, h is the thickness of the film, and k is the wave number. Acceleration a is caused by the body force as the liquid film negotiates the change in geometry. It is given by **Eq. 24**

$$a = \frac{U_{film}^2}{R_b} \quad \text{Eq. 24}$$

where U_{film} is the film velocity and R_b is the radius of curvature of an imaginary trajectory along which the film moves while it curves along the edge. Maroteaux et al [42]. used a correlation for calculating R_b as shown in **Eq. 25**

$$\frac{R_b}{h} = \frac{\pi}{\alpha_{geo}} + 1 \quad \text{Eq. 25}$$

where α_{geo} is the angle created with the horizontal. Film separation or stripping (**Eq. 26**) is modeled to occur when

$$\frac{\delta}{\delta_o} > (\frac{\delta}{\delta_o})_{critic} \quad \text{Eq. 26}$$

The critical ratio $(\frac{\delta}{\delta_o})_{critic}$ can have different values. However, as a selection of 20 gave the best agreement with experiments it has been adopted as the critical ratio in the present study. To express this in another way the stripping condition/criteria is written as in **Eq. 27**

$$\alpha_{critic} < \alpha_{geo} \quad \text{Eq. 27}$$

The critical angle α_{critic} is dependent on maximum wave growth rate ω_m, film velocity U_{film}, film height h_{film} and is given by **Eq. 28**

$$\alpha_{critic} = \frac{U_{film}}{\omega_m h_{film}} log(\frac{\delta}{\delta_o})_{critic} \quad \text{Eq. 28}$$

Note that ω_m is the obtained by maximizing **Eq. 23**

Once stripping is established 90 % of the original piston wallfilm mass accumulated at the ring gap top cell is used to create droplets [43]. The remaining 10 % stays as residual film, from which the new film height is calculated. The stripped mass is considered as the mass

of a blob that is injected from the ring gap into the region just above the piston. The radius (r_p) of the injected blob is calculated using the following **Eq. 29**

$$r_p = \sqrt{\frac{h_{film} w_{gap}}{2\pi}} \qquad \text{Eq. 29}$$

w_{gap} is the ring-gap width taken as 0.008 times engine bore [44, 45]. 50 % of the ring gap is used in **Eq. 29** as an approximate reduction of the ring gap due to the expansion of the piston ring. The total number of drops in the parcel is calculated by dividing the 90% of mass from the ring gap top cell by mass of injected blob.

2.2 Wall film evaporation

In this section, the wallfilm evaporation model [20] is explained for a simplified wallfilm setup. The analytical expression for the external heat flux to the liquid vapor interface, which is the main emphasis in this work is then derived based on this simplified setup explained in the following **Sec. 2.2.1**.

2.2.1 Model setup and formulation

Consider a liquid wallfilm of thickness L exposed to vapor (gas) phase as shown in **Figure 17.** During evaporation or condensation process, latent heat is involved, and it is supplied from/added to the wall (q_w) or the ambient mixture (q_o). Δm_{evap} is the evaporated mass, Δm_{cond} is the condensed mass. T_w, T_f, T_s and T_∞ are the wall, wallfilm interior, wallfilm surface and ambient gas temperatures, respectively. The model proposed in this work aims to obtain an analytical expression for the temperature gradient at the wallfilm-gas interface, which will in turn be used to calculate q_o. **Figure 18 (a) & (b)** show an example of the

physical temperature and concentration fields in the vapor boundary layer and within the wallfilm. **Figure 18 (c) & (d)** show the numerical thermal and concentration fields in the vapor boundary layer and within the wallfilm. The temperature distribution is linearly interpolated between the wallfilm surface, wallfilm interior, and wall temperatures. Note that species concentration is assumed constant throughout the wallfilm. The Soret [46], Dufour [47] effects and pressure gradient diffusion are considered negligible. Assuming mechanical equilibrium at the interface and quasi steady state process, the gas phase equations can be written for N liquid species as follows.

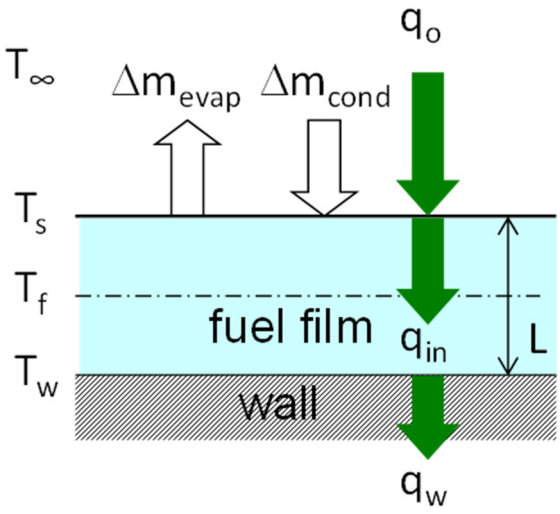

Figure 17: Problem setup

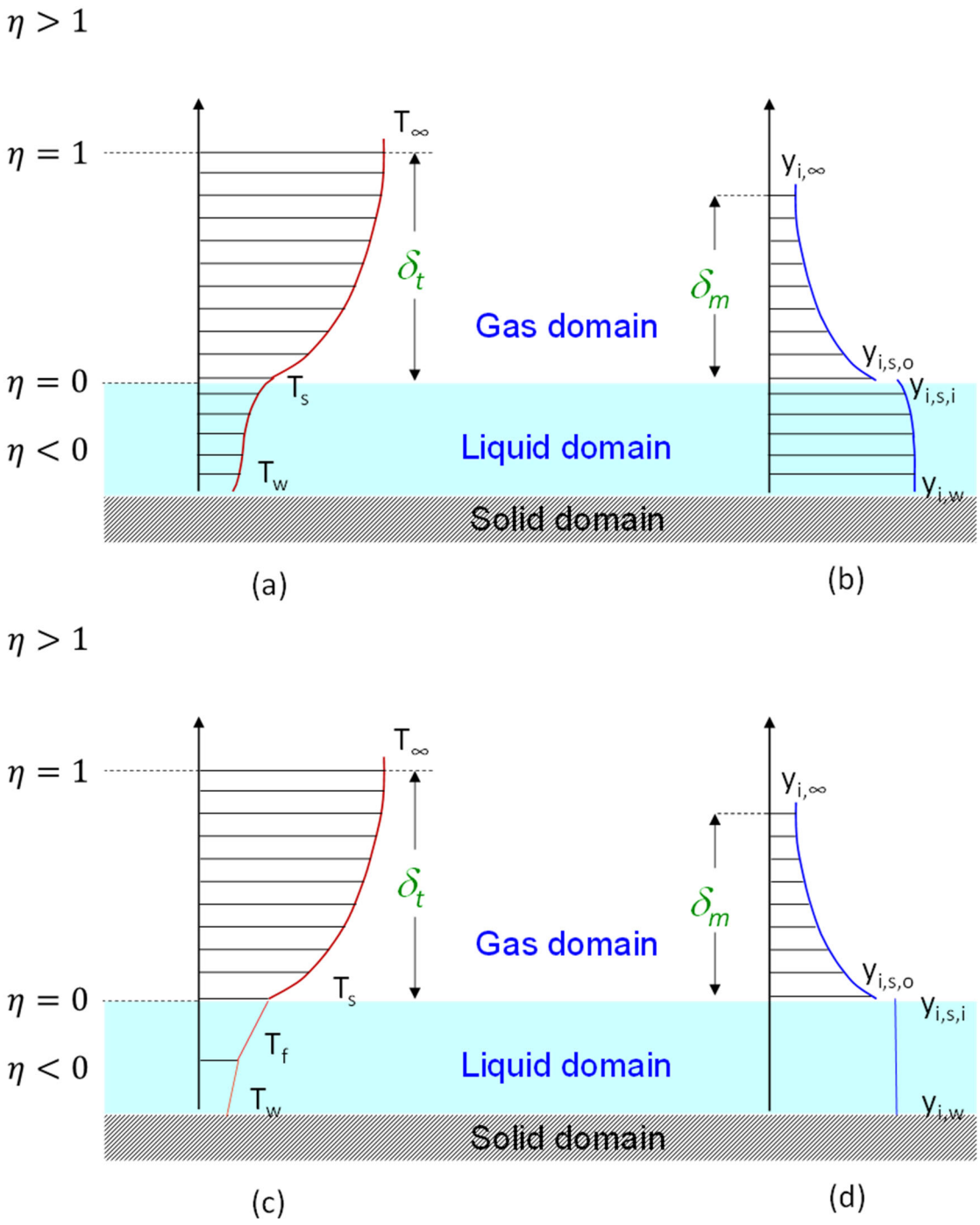

Figure 18: a) Analytical temperature distribution, b) Analytical distribution of species-i mass fraction, c) Numerical domain temperature distribution d) Numerical domain distribution of species-i mass fraction

Continuity equation

$$\nabla.(\rho v) = 0 \qquad \text{Eq. 30}$$

Energy conservation equation is given as

$$\nabla \cdot \left[\rho v \left(\int_{T_o}^{T} c_p dT\right) + \rho \sum_{i=1}^{N} y_i V_i \left(\int_{T_o}^{T} c_{p,i} dT\right) - \lambda \nabla T\right] = -\sum_{i=1}^{N} h_i^o w_i \qquad \text{Eq. 31}$$

Species conservation equation is given as

$$\nabla \cdot (\rho v y_i - \rho D \nabla y_i) = w_i \quad i = 1, \ldots N \qquad \text{Eq. 32}$$

where ρ is the averaged gas density of all species, v is the Stefan flow mean velocity vector, c_p and $c_{p,i}$ is the average specific heat and species specific heat, respectively, y_i is the species mass fraction, V_i is the diffusion velocity vector. Thus

$$y_i V_i = -D \nabla y_i \qquad \text{Eq. 33}$$

D is the average diffusion coefficient, λ is the thermal conductivity, T is the temperature. h_i^o and w_i is the standard heat of formation per unit mass and the rate of production of species i respectively.

Simplifying the 2nd term in **Eq. 31**

$$\rho \sum_{i=1}^{N} y_i V_i \left(\int_{T^o}^{T} c_{p,i} dT\right) = \sum_{i=1}^{N} \rho y_i V_i \left(\int_{T^o}^{T} c_{p,i} dT\right) = -\sum_{i=1}^{N} \rho D \nabla y_i \left(\int_{T^o}^{T} c_{p,i} dT\right) \qquad \text{Eq. 34}$$

Further, from the product rule of differentiation

$$\nabla y_i \int_{T^o}^{T} c_{p,i} dT = \nabla \left(y_i \int_{T^o}^{T} c_{p,i} dT\right) - y_i \nabla \left(\int_{T^o}^{T} c_{p,i} dT\right) \qquad \text{Eq. 35}$$

Substituting **Eq. 35** in **Eq. 34**

$$\nabla \cdot \left[-\sum_{i=1}^{N} \rho D \nabla y_i \left(\int_{T^o}^{T} c_{p,i} dT \right) \right] = \nabla \cdot \left[-\sum_{i=1}^{N} \rho D \nabla \left(y_i \int_{T^o}^{T} c_{p,i} dT \right) + \sum_{i=1}^{N} \rho D y_i \nabla \left(\int_{T^o}^{T} c_{p,i} dT \right) \right] \quad \text{Eq. 36}$$

Let $\int_{T^o}^{T} c_{p,i} dT = h_i$, then **Eq. 36** becomes

$$\nabla \cdot \left[-\sum_{i=1}^{N} \rho D \nabla y_i \left(\int_{T^o}^{T} c_{p,i} dT \right) \right] = \nabla \cdot \left[-\rho D \nabla \left(\sum_{i=1}^{N} y_i h_i \right) + \rho D \sum_{i=1}^{N} y_i \nabla (h_i) \right] \quad \text{Eq. 37}$$

If $\sum_{i=1}^{N} y_i h_i = h$ then **Eq. 37** becomes

$$\nabla \cdot \left[-\sum_{i=1}^{N} \rho D \nabla y_i \left(\int_{T^o}^{T} c_{p,i} dT \right) \right] = \nabla \cdot \left[-\rho D \nabla h + \rho D \sum_{i=1}^{N} y_i \nabla (h_i) \right] \quad \text{Eq. 38}$$

As $c_{p,i}$ is not a function of position, $\nabla(h_i)$ becomes

$$\nabla (h_i) = c_{p,i} \nabla T$$

Then **Eq. 38** becomes

$$\nabla \cdot [-\rho D \nabla h + \rho D \textstyle\sum_{i=1}^{N} y_i \nabla (h_i)] = \nabla \cdot \left[-\rho D \nabla h + \rho D \textstyle\sum_{i=1}^{N} y_i c_{p,i} \nabla T \right] = \nabla \cdot \left[-\rho D \nabla h + \rho D c_p \nabla T \right] \quad \text{Eq. 39}$$

Putting **Eq. 39** in **Eq. 31** and neglecting the effects of chemical reactions the following is obtained.

$$\nabla \cdot \left[\rho v h - \rho D \nabla h + \rho D c_p \nabla T - \lambda \nabla T \right] = 0 \quad \text{Eq. 40}$$

2.2.2 Unity Lewis number model

Lewis number is defined as the ratio of thermal to mass diffusivity. If *Le* denotes Lewis number, then unity Le number means

$$Le = \frac{\alpha}{D} = \frac{\lambda}{\rho c_p D} = 1 \qquad \text{Eq. 41}$$

where α is the thermal diffusivity. Assuming unity Lewis number, **Eq. 40** becomes

$$\nabla \cdot [\rho v h - \rho D \nabla h] = 0 \qquad \text{Eq. 42}$$

For one-dimensional (only x – direction) case **Eq. 42** becomes

$$\frac{d}{dx}\left[\rho v h - \frac{\lambda}{c_p}\frac{d}{dx}(h)\right] = 0 \qquad \text{Eq. 43}$$

If x is non-dimensionalized by the boundary layer thickness to make η, i.e., $\eta = \frac{1}{\delta}(x - x_o)$, where x_0 is the reference location, which is taken as the top surface of the liquid wall film (**Figure 18**) and δ is the boundary layer thickness (=δ_m for the species conservation equation or δ_t for the energy conservation equation). Thus $0 < \eta < 1$ indicates the region within the boundary layer. $\eta < 0$ indicates liquid and $\eta > 1$ is the ambient gas outside the boundary layer. Then **Eq. 43** becomes

$$\frac{d}{d\eta}\left[\rho v h - \frac{\lambda}{\delta_t c_p}\frac{d}{d\eta}(h)\right] = 0 \qquad \text{Eq. 44}$$

To simplify the expressions, if all the species can be classified as a summation of all wallfilm species components (y_F) and non wallfilm (air) species (y_A), then

$$\sum y_i = y_F + y_A = 1 \qquad \text{Eq. 45}$$

The species conservation equation (**Eq. 32**) for all individual wallfilm species then becomes

$$\frac{d}{d\eta}(\rho v y_F) - \frac{d}{d\eta}\left(\frac{\rho D}{\delta_m}\frac{dy_F}{d\eta}\right) = 0 \qquad \text{Eq. 46}$$

Note that non-reacting case is considered as the chemistry effect on heat transfer is not coupled and is not part of this study. Thus in **Eq. 32** $w_i = w_F = 0$. Substituting $\rho v = \rho_o v_o = m_o$ where v is the velocity of the Stefan flow, o, indicates the values at the surface of the wall film.∞ indicates values at the end of the boundary layer. Solving the equation with boundary conditions $y_F(\eta_\infty) = y_{F\infty}, y_F(\eta = 0) = y_{F,o}$, the following expression for y_F is obtained

$$y_F = \frac{y_{F,\infty} - y_{F,o}}{e^{m_o f(\eta_\infty)} - 1}\left(e^{m_o f(\eta)} - 1\right) + y_{F,o} \quad \text{Eq. 47}$$

Differentiating y_F with respect to η

$$\frac{dy_F}{d\eta} = \frac{m_0 \delta_m}{\rho D}\frac{\left(y_{F,\infty} - y_{F,0}\right)}{exp[m_0 f(\eta_\infty)] - 1} e^{m_o f(\eta)} \quad \text{Eq. 48}$$

where the function $f(\eta) = \int_0^\eta \frac{\delta_m}{\rho D} d\eta$

Solving the energy equation (**Eq. 44**) with boundary conditions $h(\eta = 0) = h_0, h(\eta = \eta_\infty) = h_\infty$ gives

$$h = \frac{h_\infty - h_0}{e^{m_o f(\eta_\infty)} - 1}\left(e^{m_o f(\eta)} - 1\right) + h_o \quad \text{Eq. 49}$$

where the function $f(\eta) = \int_0^\eta \frac{\delta_t}{\rho D} d\eta$

Derivative of enthalpy h with respect to η is

$$\frac{dh}{d\eta} = \frac{m_o \delta_t}{\rho D}\frac{h_\infty - h_0}{e^{m_o f(\eta_\infty)} - 1} e^{m_o f(\eta)} \quad \text{Eq. 50}$$

Derivative of enthalpy can also be written as

$$\frac{dh}{d\eta} = \frac{d}{d\eta}\left(\int_{T^o}^{T} c_p dT\right) = c_p \frac{dT}{d\eta} + \sum_{i=1}^{N} h_i \frac{dy_i}{d\eta} \quad \text{Eq. 51}$$

Considering only wallfilm components (F) and air (A) as species and substituting **Eq. 48** in **Eq. 51** and rearranging **Eq. 51**

$$\frac{dT}{d\eta} = \frac{m_0 \delta_t}{\lambda} \frac{\left[(h_\infty - h_0) - (h_F - h_A)\left(y_{F,\infty} - y_{F,0}\right)\right]}{e^{m_o f(\eta_\infty)} - 1} e^{m_o f(\eta)} \quad \text{Eq. 52}$$

Note that $f(\eta = 0) = 0$, $f'(\eta) = \frac{\delta_t}{\rho D} = \frac{\delta_t c_p}{\lambda}$, and $f''(\eta) = \frac{\delta_t}{\lambda} \frac{dc_p}{d\eta}$

The evaluation of $f(\eta)$ is provided in the **Appendix A.1.** The mixture specific heat is given as

$$c_p = c_{p,F} y_F + c_{p,A} y_A = \left(c_{p,F} - c_{p,A}\right) y_F + c_{p,A} \quad \text{Eq. 53}$$

Differentiating c_p with respect to η gives the gradient of the specific heat as

$$\frac{dc_p}{d\eta} = \left(c_{p,F} - c_{p,A}\right) \frac{dy_F}{d\eta} \quad \text{Eq. 54}$$

Differentiating **Eq. 47** and substituting in **Eq. 54**

$$\frac{dc_p}{d\eta} = \left(c_{p,F} - c_{p,A}\right) \frac{m_0 \delta_m}{\rho D} \frac{(y_{F,\infty} - y_{F,0})}{e^{m_0 f(\eta_\infty)} - 1} e^{m_0 f(\eta)} \quad \text{Eq. 55}$$

The heat flux from the surrounding gas mixture to the film is calculated as

$$q_o = \lambda \frac{dT(x = x_0)}{dx} = \frac{\lambda}{\delta_t} \frac{dT(\eta = 0)}{d\eta} = \frac{m_0 \left[(h_\infty - h_0) - (h_F - h_A)\left(y_{F,\infty} - y_{F,0}\right)\right]}{exp[m_0 f(\eta_\infty)] - 1} \quad \text{Eq. 56}$$

To make this formulation more rigorous the Lewis number assumption is relaxed which is discussed in the following section

2.2.3 Non unity Lewis number model

For non-reacting case with non-unity Le, **Eq. 31** can be rewritten in 1-dimensional Cartesian coordinate system as

$$\frac{d}{dx}\left[\rho v h - \rho \sum_{i=1}^{N}\left(D_i \frac{dy_i}{dx}\right) h_i - \lambda \frac{dT}{dx}\right] = 0 \qquad \text{Eq. 57}$$

Integrating **Eq. 57** gives

$$\rho v h - \rho \sum_{i=1}^{N}\left(D_i \frac{dy_i}{dx}\right) h_i - \lambda \frac{dT}{dx} = C_1 \qquad \text{Eq. 58}$$

where C_1 is the integral constant.

Assuming constant specific heat for all species, i.e., $c_{p,i} = \text{constant}$, the enthalpy of individual species and mixture can be expressed as

$$h_i = c_{p,i} T \qquad \text{Eq. 59}$$

Further considering all species as either from wallfilm components (F) or air (A), **Eq. 59** becomes

$$h = h_F y_F + h_A y_A = \left(c_{p,F} y_F + c_{p,A} y_A\right) T = \left[\left(c_{p,F} - c_{p,A}\right) y_F + c_{p,A}\right] T \qquad \text{Eq. 60}$$

where $c_{p,F}$ and $c_{p,A}$ are average wallfilm components specific heat and air specific heat, respectively. Inserting **Eq. 59** and **Eq. 60** into **Eq. 58** and using a non-dimensional variable, $\eta = (x - x_0)/\delta_t$, **Eq. 58** after rearranging becomes

$$\frac{dT}{d\eta} + \left\{\frac{\rho D}{\lambda}\left[\left(c_{p,F} - c_{p,A}\right)\frac{dy_F}{d\eta}\right] - \frac{\rho v \delta_t}{\lambda}\left[\left(c_{p,F} - c_{p,A}\right) y_F + c_{p,A}\right]\right\} T - C_1 = 0 \qquad \text{Eq. 61}$$

or

$$\frac{dT}{d\eta} + g(\eta) T = C_1 \qquad \text{Eq. 62}$$

where

$$g(\eta) = \frac{\rho D}{\lambda}\left[\left(c_{p,F} - c_{p,A}\right)\frac{dy_F}{d\eta}\right] - \frac{\rho v \delta_t}{\lambda}\left[\left(c_{p,F} - c_{p,A}\right) y_F + c_{p,A}\right] \qquad \text{Eq. 63}$$

Using **Eq. 47** and **Eq. 48**, **Eq. 63**becomes

$$g(\eta) = m_o(\delta_m - \delta_t)\frac{A}{\lambda}\left(c_{p,F} - c_{p,A}\right)e^{m_o f(\eta)} - \frac{m_o\delta_t}{\lambda}\left[\left(c_{p,F} - c_{p,A}\right)(y_{F,o} - A) + c_{p,A}\right] \quad \text{Eq. 64}$$

or

$$g(\eta) = B_1 e^{m_o f(\eta)} + B_2 \quad \text{Eq. 65}$$

where $A = \frac{y_{F,\infty} - y_{F,o}}{e^{m_o f(\eta\infty)} - 1}$, $B_1 = m_o(\delta_m - \delta_t)\frac{A}{\lambda}\left(c_{p,F} - c_{p,A}\right)$ and $B_2 = -\frac{m_o\delta_t}{\lambda}\left[\left(c_{p,F} - c_{p,A}\right)\left(y_{F,o} - A\right) + c_{p,A}\right]$.

The solution of the differential equation [48], **Eq. 62** is obtained as

$$T(\eta) = e^{-s}\left(\int C_1 e^{s} d\eta + C_2\right) \quad \text{Eq. 66}$$

Where

$$s = \int g(\eta) d\eta = \int \left(B_1 e^{m_o f(\eta)} + B_2\right) d\eta \quad \text{Eq. 67}$$

and C_2 is another integral constant. Applying Taylor series expansion to s about $\eta = 0$

$$s(\eta) = s(0) + \frac{s'(0)\eta}{1} + R \quad \text{Eq. 68}$$

Evaluating $s(0)$ from **Eq. 67**, gives the following

$$s(0) = \int \left(B_1 e^{m_o f(\eta)} + B_2\right) d\eta = B_1 \int e^{m_o f(\eta)} d\eta + B_2(0) \quad \text{Eq. 69}$$

If $f(\eta)$ is linearly approximated to $\frac{\delta_t \eta}{\rho D}$, and then applied to **Eq. 69**, $s(0)$ becomes

$$s(0) = \frac{\rho D B_1}{m_0 \delta_t} \quad \text{Eq. 70}$$

Similarly, $s'(0)$ is evaluated to give

$$s'(\eta = 0) = \frac{d\int g(\eta = 0) d\eta}{d\eta} = g(\eta = 0) = (B_1 + B_2) \quad \text{Eq. 71}$$

Substituting **Eq. 70** & **Eq. 71** in **Eq. 69** , the expression for $s(\eta)$ is

$$s(\eta) = \frac{\rho D B_1}{m_0 \delta_t} + (B_1 + B_2)\eta + R \quad \text{Eq. 72}$$

where R is the residual error. Then $s(\eta)$ can also be written as

$$s = E_1\eta + E_2 \quad \text{Eq. 73}$$

where $E_1 = B_1 + B_2$. $E_2 = \frac{\rho D B_1}{m_0 \delta_t} + R$

Then, temperature distribution is obtained as

$$T(\eta) = e^{-(E_1\eta + E_2)}\left(\int C_1 e^{(E_1\eta + E_2)}\, d\eta + C_2\right) \quad \text{Eq. 74}$$

Inserting **Eq. 74** back to **Eq. 62** gives

$$\frac{dT}{d\eta} = -\left(B_1 e^{m_o f(\eta)} + B_2\right)\left[e^{-(E_1\eta + E_2)}\left(C_1 \frac{e^{E_1\eta + E_2}}{E_1} + C_2\right)\right] + C_1 \quad \text{Eq. 75}$$

Applying the boundary conditions, $T(\eta = 0) = T_0$, $T(\eta = 1) = T_\infty$ to **Eq. 74**

$$T_o = \left(\frac{C_1}{E_1} + C_2 e^{-E_2}\right) \quad \text{Eq. 76}$$

$$T_\infty = e^{-(E_1 + E_2)}\left(\frac{C_1}{E_1} e^{E_1 + E_2} + C_2\right) \quad \text{Eq. 77}$$

where $C_2 = \frac{T_\infty - T_o}{e^{-(E_1 + E_2)} - e^{-E_2}}$, $C_1 = (T_o - C_2 e^{-E_2})E_1$

Therefore, the external heat flux is given as

$$q_o = \frac{\lambda}{\delta_t}\frac{dT(\eta = 0)}{d\eta} = \frac{\lambda}{\delta_t}[C_1 - (B_1 + B_2)(\frac{C_1}{E_1} + C_2 e^{-E_2})]$$

or

$$q_o = \frac{\lambda}{\delta_t}\frac{dT(\eta = 0)}{d\eta} = \frac{\lambda}{\delta_t}[C_1 - (B_1 + B_2)T_0] \quad \text{Eq. 78}$$

2.2.4 Non unity Lewis number with correction

The unity Le model (**Sec. 2.2.2**) and the non-unity Le model (**Sec. 2.2.3**) were derived in slightly different ways where certain assumptions are made at different stages of the derivation. For the unity-Le model $c_{p,i}$ is assumed to be a function of temperature only and enthalpy is expressed as an integral form with respect to temperature. In comparison for the non-unity Le model, $c_{p,i}$ is assumed to be a constant, which is reasonable for a boundary layer with relatively small temperature change. As a result, $h_i = c_{p,i}T$.

For a flow condition that meets unity Le strictly, the solution from the unity-Le model is thought to be more rigorous, and thus it can be used as a reference to check the performance of the non-unity Le model. However, it is notable that the unity Le model is not valid for flows with non-unity Le, while the non-unity Le model is expected to capture the effect of Le variation although it cannot give exact solutions quantitatively because of the assumption of constant $c_{p,i}$. Hence, if the quantitative agreement at unity Le condition is made to the non-unity Le model, it ensures that the non-unity Le model can reliably capture the phase change behavior at arbitrary Le conditions. A correction factor is used to make this quantitative agreement.

The difference in external heat flux values q_o at Lewis number 1 between U-Le and NU-Le models is the amount to be adjusted in NU-Le model, which is defined as the correction factor K_a. Then,

$$K_a = \frac{\lambda}{\delta_t}\left[\left(\left.\frac{dT}{d\eta}\right|_0\right)_u - \left(\left.\frac{dT}{d\eta}\right|_0\right)_{nu(\delta_m=\delta_t)}\right] \quad \text{Eq. 79}$$

where $\left(\left.\frac{dT}{d\eta}\right|_0\right)_u$ is the temperature gradient at the liquid-vapor interface obtained from U-Le model and $\left(\left.\frac{dT}{d\eta}\right|_0\right)_{nu(\delta_m=\delta_t)}$ is the temperature gradient obtained from NU-Le model.

Substituting the values for temperature gradient from **Sec. 2.2.2** and **Sec. 2.2.3** K_a becomes

$$K_a = \frac{m_0\delta_t}{\lambda}\frac{\left[(h_\infty - h_0) - (h_F - h_A)\left(y_{F,\infty} - y_{F,0}\right)\right]}{e^{m_o f(\eta_\infty)} - 1} + B_2C_2e^{-E_2} \quad \text{Eq. 80}$$

The corrected external heat flux q_{corr} is

$$q_{corr} = q_{nu} + K_a$$

$$= \frac{m_0\delta_t}{\lambda}\frac{\left[(h_\infty - h_0) - (h_F - h_A)\left(y_{F,\infty} - y_{F,0}\right)\right]}{e^{m_o f(\eta_\infty)} - 1} + B_2C_2e^{-E_2} - E_1C_2e^{-E_2}$$

$$= \frac{m_0\delta_t}{\lambda}\frac{\left[(h_\infty - h_0) - (h_F - h_A)\left(y_{F,\infty} - y_{F,0}\right)\right]}{e^{m_o f(\eta_\infty)} - 1} - B_1C_2e^{-E_2}$$

$$= \frac{m_0\delta_t}{\lambda}\frac{\left[(h_\infty - h_0) - (h_F - h_A)\left(y_{F,\infty} - y_{F,0}\right)\right]}{e^{m_o f(\eta_\infty)} - 1} - \frac{(T_\infty - T_o)B_1}{e^{E_1} - 1} \quad \text{Eq. 81}$$

2.2.5 Energy balance equation

The energy balance equation at the interface between liquid and gas domains (**Figure 18**) can be written as

$$q_o + q_{in} = m_0L \quad \text{Eq. 82}$$

q_0 is the external heat flux calculated in **Sec. 2.2.2/Sec. 2.2.3**. L is the latent heat of vaporization. For non-boiling conditions and low evaporation rates m_0 is given by Spalding's equation

$$m_0 = h_y \, ln\left(\frac{1 - y_\infty}{1 - y_s}\right) \quad \text{Eq. 83}$$

where h_y, y_∞, y_s is the mass transfer coefficient, ambient gas wallfilm species mass fraction, wallfilm species mass fraction at the vapor side of the interface, respectively. y_s is function of the wallfilm surface temperature and determined using Raoults law [27]. Internal heat flux q_{in} is calculated by

$$q_{in} = h_i(T_s - T_f) \quad \text{Eq. 84}$$

where h_i, T_s, T_f is the film heat transfer coefficient, wallfilm surface, and wallfilm interior temperature, respectively.

For boiling case, the wallfilm surface temperature T_s is fixed as the saturation temperature and the wallfilm species mass fraction at the vapor side of the interface becomes unity, i.e., $y_s = 1$, where **Eq. 83** is not valid. Therefore, the evaporation rate is determined based on the energy balance at the wallfilm surface only. The internal heat transfer coefficient for both boiling and non-boiling case is given in Ref. [27, 49]

As the wall temperature is assumed to be known from the Dirichlet boundary condition at the liquid wallfilm-solid wall interface, wall heat transfer is modeled as a conduction process and its flux is given by

$$q_w = \frac{2\lambda_f}{L}(T_w - T_f) \quad \text{Eq. 85}$$

where T_w, T_f, λ_l, L are the wall temperature, wallfilm interior temperature, thermal conductivity of film and film height, respectively. Note $\frac{L}{2}$ is used as the characteristic length.

3 Results and discussions

This section is divided into two sub-sections. **Sec. 3.1** presents results related to the pre-ignition and **Sec. 3.2** presents the results pertaining to the wall film evaporation model.

3.1 Pre-ignition

First, the models described in **Sec. 2.1** is validated with experimental data which is described from **Sec. 3.1.1** onwards. After validation of the model, methane gas injection in CVCC along with simultaneous lube oil drop injection studies are carried out. Next, results with respect to oil film dynamics in engines are presented which is followed by a pre-ignition case demonstration in a marine engine.

3.1.1 Mixing fan simulation

The fan region was defined with dimensions shown in **Figure 3**. The z-velocity (upward suction) of 3 m/s was assigned to those nodes that fall in the fan blade region for every cycle (**Figure 4**). The initial pressure and temperature were $25e^5$ Pa and 730 K (same as for CVCC experiment). Non-adiabatic simulation was run to capture experimental conditions until steady state was obtained. **Figure 19 (a)** shows the steady state velocity field produced by the mixing fan in the plane passing through the center of the fan. The overall velocity field plot indicates there is suction towards the fan from the lower regions of the chamber. The maximum velocity is just upstream of the fan, slightly higher than the set velocity (3 m/s). The effect of the wall on vortex generation can be seen in the region to the right of the fan. This is more clearly shown in **Figure 19 (c)**. The region to the left of the fan, has a much larger vortex pattern tracing the wall as can be seen in **Figure 19 (b)**. This steady

state velocity field is used as the initial condition through which oil drop is injected. All other cell centered variables (temperature, species density, pressure, turbulent kinetic energy and turbulence dissipation rate) are recorded to be mapped as initial conditions for drop injection and ignition simulations explained in the following section.

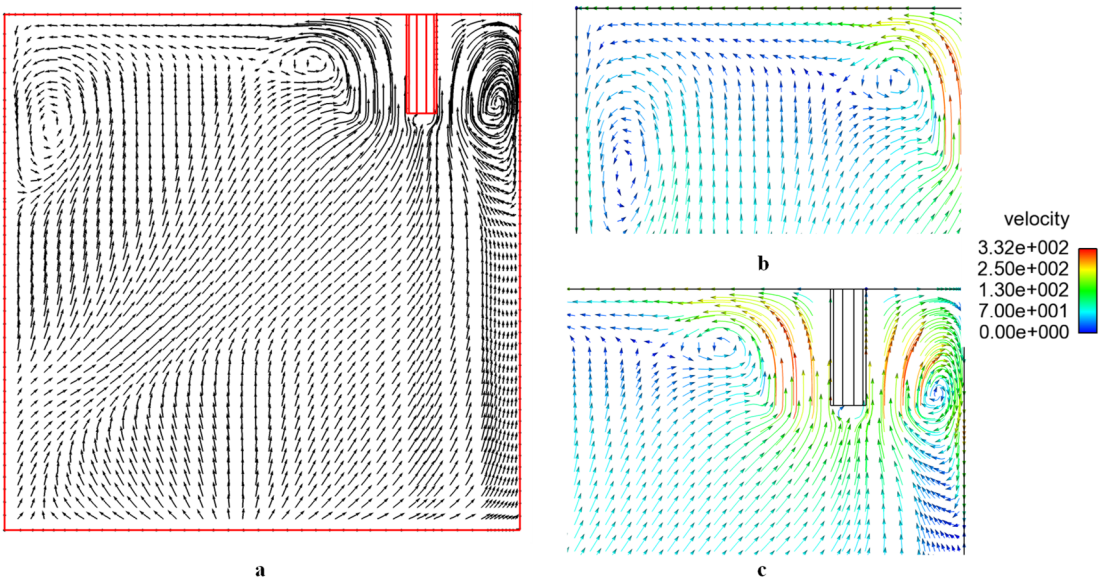

Figure 19: a) Flow velocity field produced by fan b), c) flow velocity field in more detail

3.1.2 Drop ignition

A single drop of lube oil was injected from the center of the right wall, where the injector is located in the experimental setup. The drop diameter obtained from experiments through advanced imaging techniques was approximately $220e^{-6}$ m. The oil drop was injected into a pre-burn mixture with composition indicated in **Table 1**. Although the experiment contains many drops injected, the drop of concern is marked in red as seen in **Figure 20 (a)**, which is captured at 2 ms after injection. This drop is isolated from other drops and hence was chosen to model as a single drop in the simulation. The experimental data

presented here is obtained after conducting many trials to isolate a single drop. The initial drop injection velocity was 2.53 m/s, initial drop temperature was 586 K. The ambient conditions are mapped from the steady state simulation of the fan. The drop path depends on the flow field produced by the fan, the ambient conditions, drop initial velocity and drop initial temperature. **Figure 20 (b)** shows the drop encircled by red at 4-time intervals (2ms, 4.6ms, 8.8ms and 23.4 ms) sequentially from right to left until ignition. The ignition time measured for this drop was 23.4 ms as indicated by the luminous white spot. In **Figure 20 (c)**, the experimental drop path is compared to the simulation path. The red circles indicate the location of the experimental drops. The yellow line indicates the simulated drop path. The match is considered within acceptable limits of accuracy. It should be noted that there is some uncertainty in the path with respect to the exact location as a simplified model for the fan was used. Using the models described in **Sec. 2.1**, the ignition time for the simulation was 23.02 ms, in comparison to the experimental ignition time of 23.4 ms.

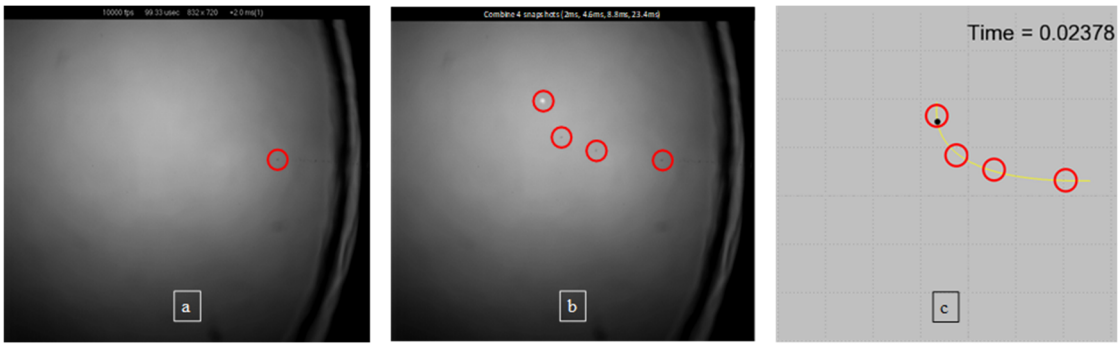

Figure 20: a) drop simulated b) Experimental and c) simulation drop path and ignition comparison

3.1.3 Effect of methane on ignition

With the SPIC model predicting good agreement with experimental data, a parametric study was done by varying the ambient composition of methane gas in the pre-burn mixture. The motivation for this was to study the effect of drop ignition in different equivalence ratios, which is expected in natural gas engines. These cases were run in adiabatic mode as only a simulation study is considered. 5 equivalence ratios were studied namely 0.5, 0.65, 0.7, 1.0 and 1.3. Note that the gas engine of interest runs at an equivalence ratio of 0.65. Equivalence ratios are varied by changing the methane and N_2 mole fractions accordingly. In all these simulations, drop initial injection velocity used was 2.53 m/s, drop diameter was $220e^{-6}$ m and drop temperature of 531 K was used. The fan parameters were unchanged. The drop ignition times obtained from the simulation are provided in **Table 3** below. From the table, it is seen there is only a small effect as all times are between 19 to 20 ms.

Table 3: Ignition times for different equivalence ratios

Progressive equivalence ratio	Ignition times (ms)
0.5	19.76
0.65	19.22
0.7	19.19
1.0	19.15
1.3	19.46

Although the initial conditions were the same, change in ambient composition affects the lube drop vaporization rates. This is evident in **Figure 21** showing total vapor vs. time for

different equivalence ratios (phi). The accumulated vapor is highest for equivalence ratio of 1.3 and lowest for equivalence ratio of 0.5. It is proportional to equivalence ratio. In 1.3 equivalence ratio case, the subcell has the largest amount of methane. Due to higher specific heat capacity of methane compared to air the temperature drop for this case is the lowest. Higher temperature thus implies higher vaporization rate.

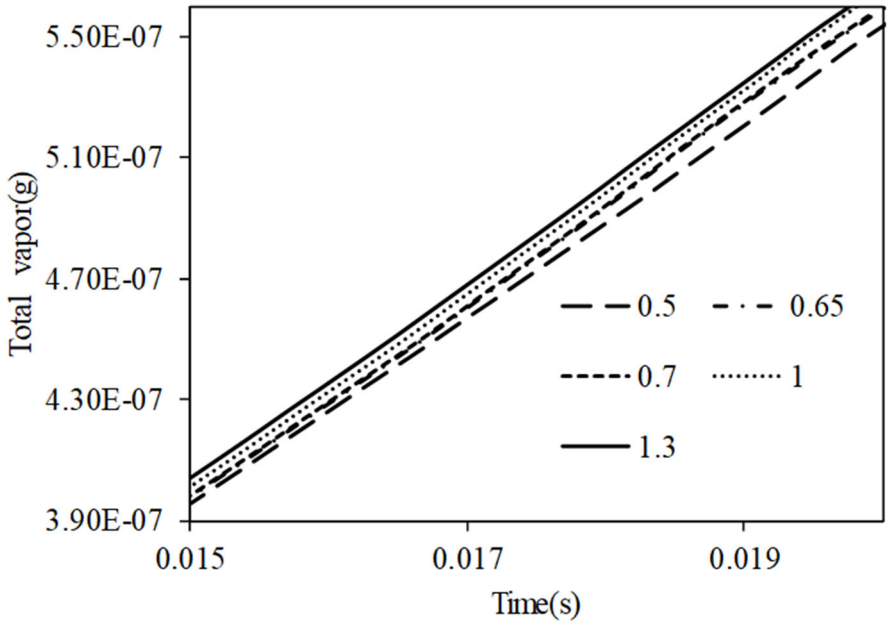

Figure 21: Total accumulated vapor for various different equivalence ratios

In order to understand the small differences in ignition time, the kinetics of the ignition cell is studied in more detail. **Figure 22 (a)** shows the profiles of lube-oil density in the ignition subcell for various equivalence ratios. In all cases, lube-oil vaporization causes initial increase, after which consumption and reactions start causing the curve to decrease. Thus, the nature of the curve is determined by the speed of addition and consumption of lube oil

species. Although the overall evaporation rate of lube-oil is highest for an equivalence ratio of 1.3, the time spent in the ignition subcell is much smaller when compared to the other cases. This is evident from lower peak value of lube oil density for initial methane equivalence ratio of 1.3 in **Figure 22 (a)**. Similarly, equivalence ratio of 0.5 produces the highest peak of lube density. The varied time distribution among the curves indicates that the drop enters the ignition cells at different times. **Figure 22 (b)** shows the peak species density of lube oil and methane present at that time with respect to initial methane equivalence ratio.

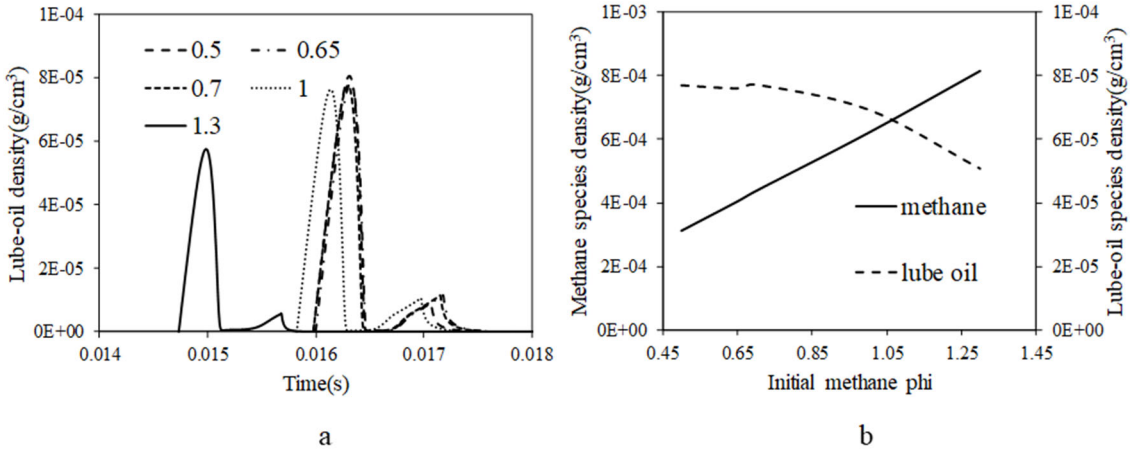

Figure 22: a) Profiles of lube-oil density in the ignition subcell for different initial methane equivalence ratios. b) Variation of peak lube-oil and corresponding methane density with initial methane equivalence ratio

The reactivity of the ignition subcell when the drop enters it is studied by comparing ignition delays of the mixtures before lube oil addition. For simplicity only three cases are plotted in **Figure 23 (a)**. Before the drop enters the ignition cells, they contain methane and the pre-burn mixture according to the initial composition. As expected among these three cases, the reactivity of the mixture with an initial methane phi = 1.0 is the highest,

indicated by the shortest ignition delay time, and that of the mixture with initial methane phi =0.65 is the lowest. The criteria used for ignition delay was a temperature rise of 400K from the initial temperature. To study the effect of lube oil addition to pre-burn mixtures containing constant amount of methane (phi = 1), ignition delay of mixtures with varying lube-oil amounts was calculated and compared in **Figure 23 (b)**. The existence of lube oil in the mixture substantially increases the mixture reactivity, compared to methane only cases (**Figure 23 (a)**). Ignition delay decreases as the amount of lube-oil is increased. Also seen in both figures is substantial effects of mixture temperatures on the ignition delay.

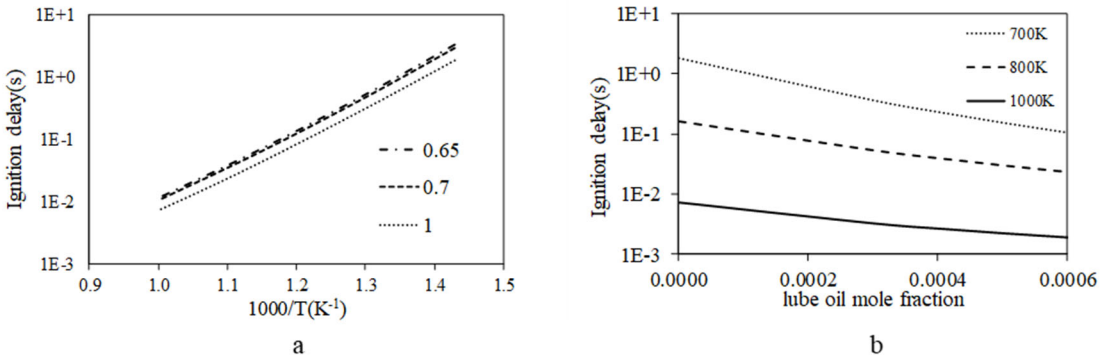

Figure 23: Reactivity of ignition cells (a) without, and (b) with lube oil vapor (with unity initial methane equivalence ratio).

A U-pattern behavior was observed between the drop ignition time (the time a drop takes until ignition after entering a subcell) and equivalence ratio, as shown in **Figure 24**. This is attributed to the combined effects of methane and lube-oil amounts in the mixture. As shown above (see **Figure 22 (b)**), mixtures with less initial methane tend to have more lube-oil. Increasing lube-oil amounts should shorten ignition delays. However, the effects of decreasing methane cancel off the mixture reactivity increase, resulting in longer ignition delay with decreasing methane (or increasing lube-oil). Hence the ignition delay

reaches a minimum for a certain mixture condition. In the present study, it was found to be around initial methane phi of 0.8. Overall, however, varying equivalence ratio of the ambient gases has minor effect on the total ignition time (time between start of injection and ignition), as they are between 19 to 20 ms in all cases.

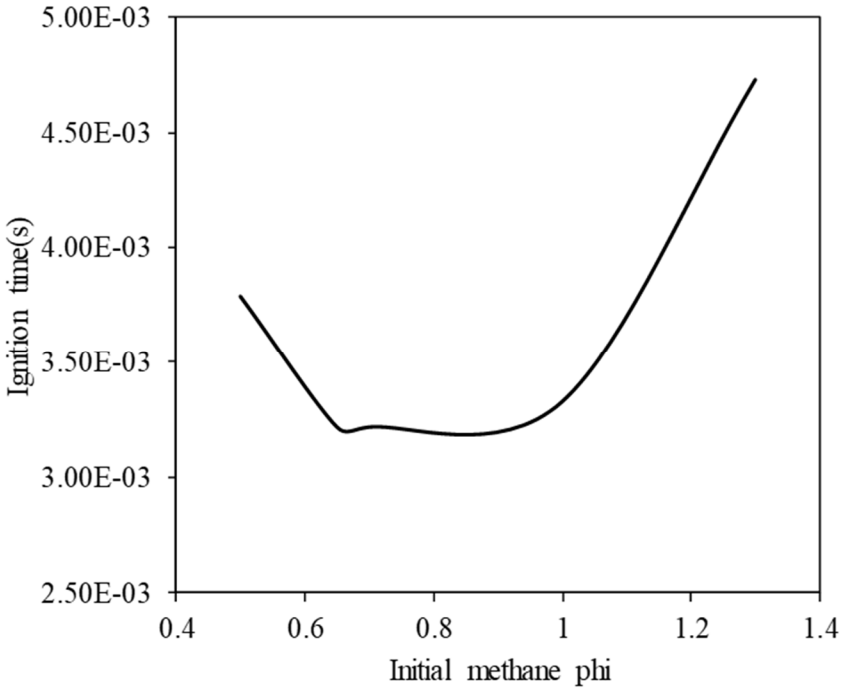

Figure 24: Ignition time pattern on drop entering subcell for different initial methane conditions

3.1.4 Flame propagation

Once ignition is determined, the center of the subcell containing the droplet is considered as the point of flame kernel initiation. The DPIK model is used to calculate the kernel growth [36]. The Level set method is used to track the flame surface. Once the kernel is large enough, the model is switched to turbulent flame propagation [50].

3.1.5 Gas injection

In the previous sections, drop injection in homogenous methane mixtures was considered. In this section drop injection in heterogeneous methane mixtures are studied. For this purpose, methane gas injection simulation [51] is used. Three cases in adiabatic condition are initially investigated, each with different drop injection timing to decouple wall heat loss effect. Lastly non-adiabatic gas injection is compared to understand the wall heat loss effect on the flow field and drop ignition. The gas injection parameters are provided in **Table 4**. These parameters are maintained the same for all simulations. The gas injector is located at the center of the bottom wall of the CVCC. The fan parameters were kept the same. In **Figure 25**, the velocity vectors at different times are shown after gas injection. The magnitude of these vectors is much larger than those produced by the fan alone, indicating that gas injection will mainly affect drop particle motion. The injected methane flows to the top of the chamber and trickles down along the sides.

Table 4: Gas injection parameters

Injector cone angle	14°
Injector nozzle area	1.97×10^{-3} cm^2
Jet stagnation pressure	100 bar
Jet temperature	300 K
Injected mass	0.55 g
Injection duration	50 ms
Nozzle discharge coefficient	1
Nozzle friction coefficient	0.85
Coefficient for jet core length	12.5
Coefficient for velocity scaling for TKE calculation in jet core	0.12
Coefficient for energy dissipation rate in jet core and fully developed region	0.25

Coefficient for velocity scaling for TKE calculation in fully developed jet	0.2
Coefficient for axis velocity calculation	0.043
Fraction of cell velocity compared to jet axis velocity to determine if the cell is reached by jet	0.01

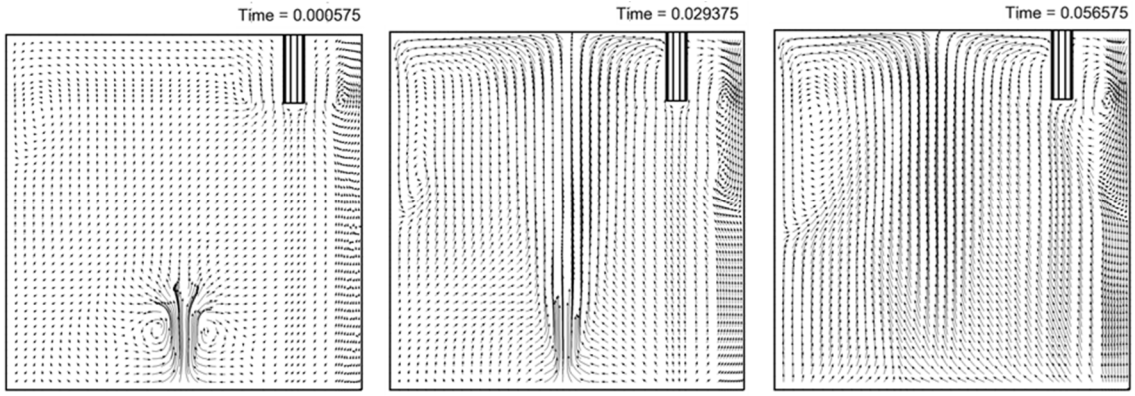

Figure 25: Velocity vectors caused by the fan and gas injection

All top and front view figures of the three cases explained below are taken in the plane containing the drop with time in seconds. The drop size in the figures is not to scale. In case 1, the drop temperature was 537 K, drop diameter was $220e^{-6}$ m and drop injection velocity was 2.53 m/s. The drop was injected at 55 ms, 5 ms after the gas injection was completed. **Figure 26 (a-c)** show the drop motion in the CVCC as well as the methane species density. **Figure 26 (d-i)** shows comparison of temperature and equivalence ratios with time of refined and parent cells respectively. The saw tooth pattern in these figures is due to the drop entering new refined cells. The stratification effect is still seen when the drop enters the combustion chamber as shown in **Figure 26 (a)**. The drop is initially injected horizontally and on moving further is affected by the fan and methane injection flow field, being redirected upwards. In **Figure 26 (d)** and **Figure 26 (e)**, as the drop is

initially injected at 55 ms, it is seen it traverses many refined cells in a short time (seen by the dense profiles) owing to the initial injection velocity. The refined cell temperatures drop once the drop enters them, due to the evaporative cooling. On its way upward, it flows through the lean region indicated by the blue region. From approximately 75 ms, the drop starts getting directed towards back wall of the chamber as can be seen from the top view (**Figure 26 (a)**). However, as the drop velocity is very fast, it reaches the top wall of the chamber, without ignition (**Figure 26(a)**). The drop does not spend enough time in any of the refined cells, as result of which the maximum equivalence ratio does not exceed 0.55 (**Figure 26 (e)**). Consequently, the refined cell temperature does not go over 730 K.

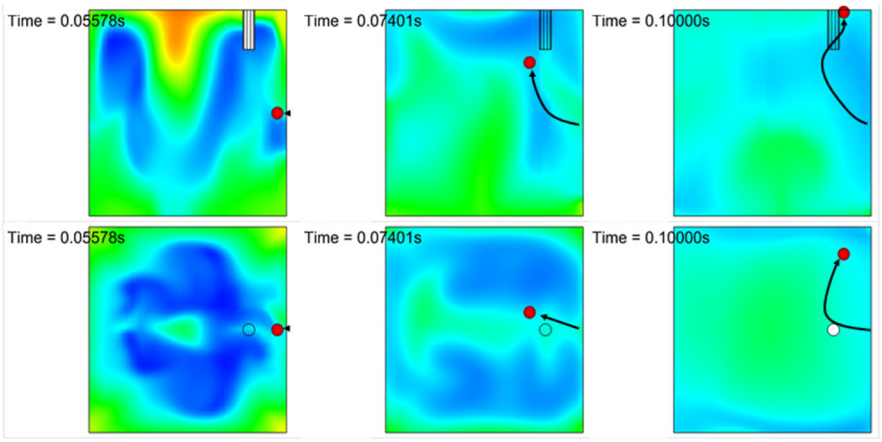
Time = 0.05578s
Time = 0.07401s
Time = 0.10000s
Time = 0.05578s
Time = 0.07401s
Time = 0.10000s

a

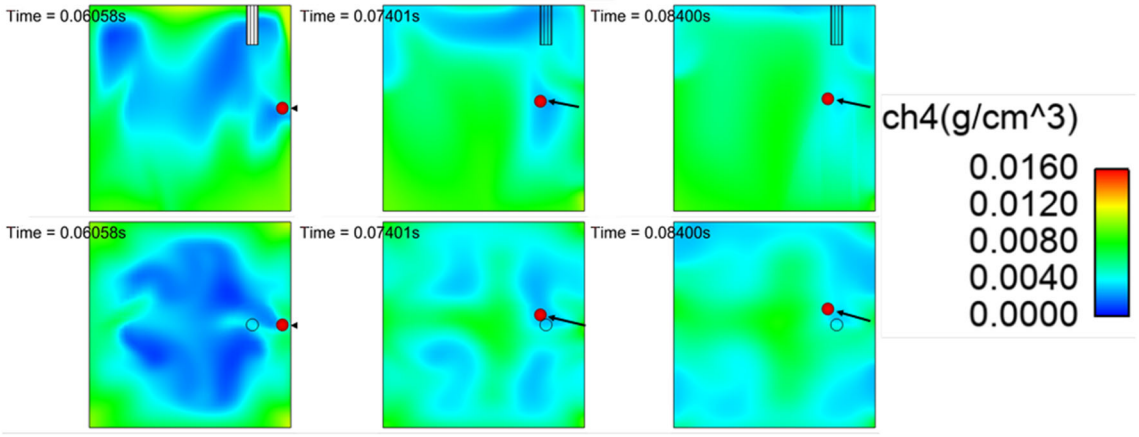
Time = 0.06058s
Time = 0.07401s
Time = 0.08400s
Time = 0.06058s
Time = 0.07401s
Time = 0.08400s
ch4(g/cm^3)
0.0160
0.0120
0.0080
0.0040
0.0000

b

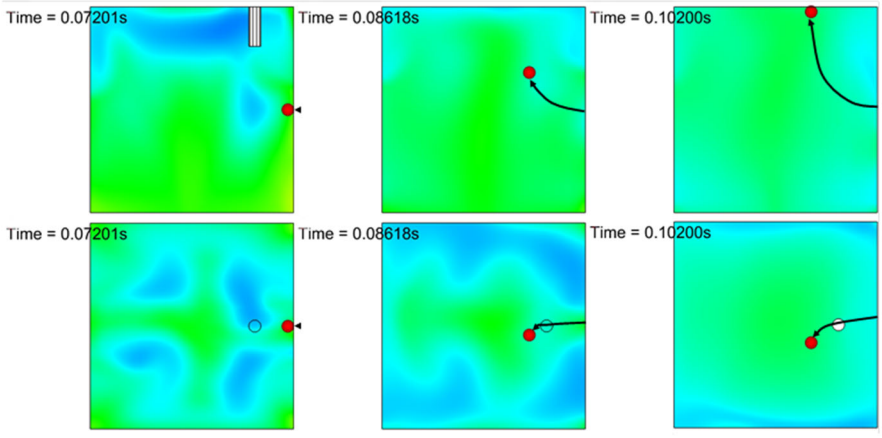
Time = 0.07201s
Time = 0.08618s
Time = 0.10200s
Time = 0.07201s
Time = 0.08618s
Time = 0.10200s

c

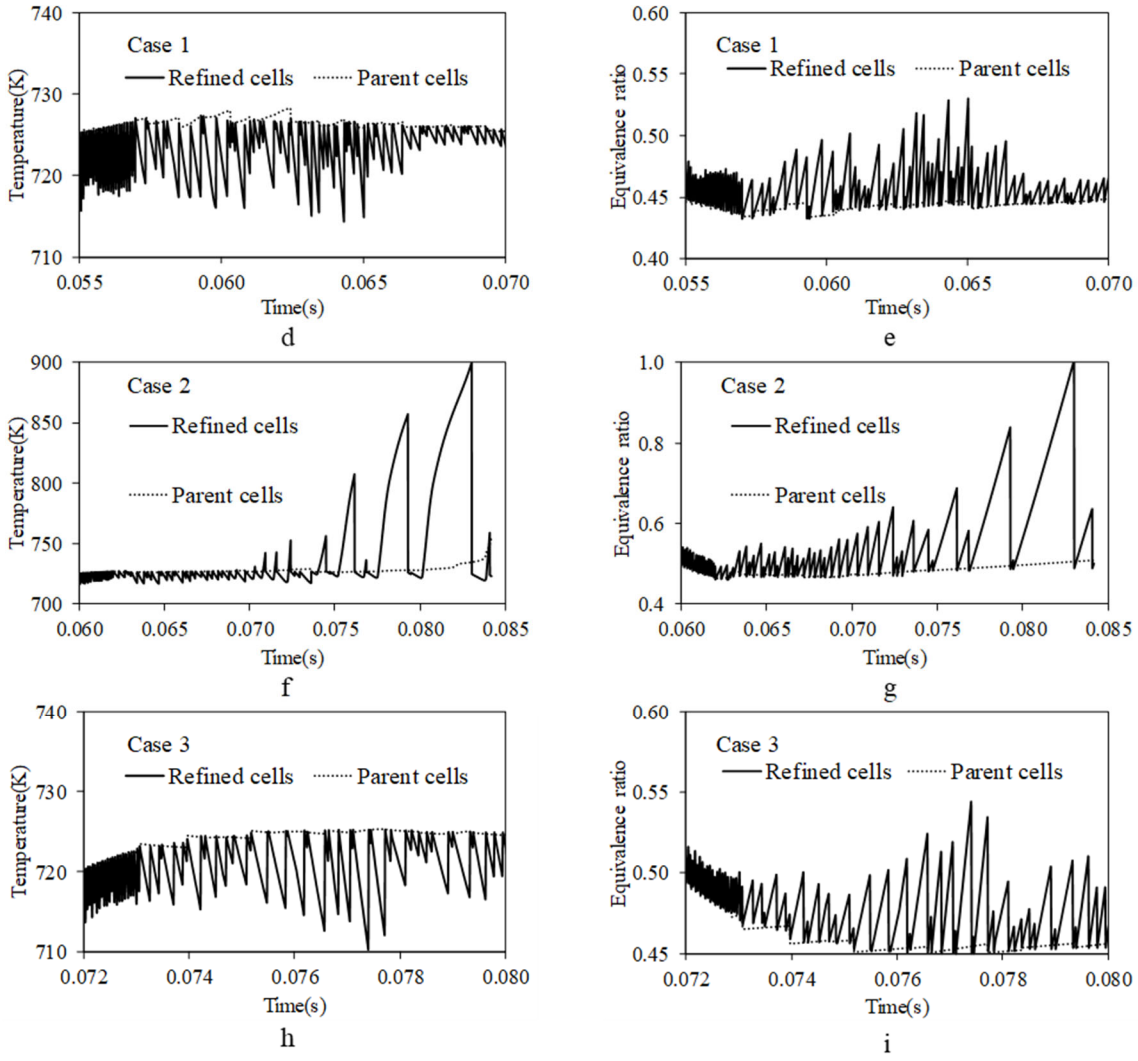

Figure 26: front and top views of a) Case 1 55 ms drop injection with drop velocity 2.53 m/s b) Case 2 60 ms drop injection with drop velocity 2.53 m/s c) Case 3 72 ms drop injection with drop velocity 5 m/s d) Case 1 refined and parent cell temperature vs time e) Case 1 refined and parent cell equivalence ratio f) Case 2 refined and parent cell temperature vs time g) Case 2 refined and parent cell equivalence ratio h) Case 3 refined and parent cell temperature vs time i) Case 3 refined and parent cell equivalence ratio

In case 2, the drop injection time was delayed by 5 ms and injected at 60 ms as shown in **Figure 26(b)**. Hence, the ambient mixture conditions are expected to be slightly different, exerting more resistance to slow down the drop in the injection direction. The drop at 74

ms keeps traveling in the lean region. The local velocity flow field surrounding the drop does not push the drop upwards as in the earlier case. Thus, the drop approximately maintains its horizontal motion. **Figure 26 (f)** and **Figure 26 (g)** confirm this trend. The equivalence ratio is steadily increasing, and towards 82 ms, crosses the threshold value of 0.9, which leads to ignition. The same pattern is observed in the temperature (**Figure 26 (f)**). After the initial decrease, as the refined cell becomes richer with fuel, the temperature starts rising rapidly. This is in sharp contrast to the parent cell temperature and equivalence ratio's which do not show significant increase. From the top view (**Figure 26 (b)**), it is also evident that the drop is still in the center of the chamber and has not moved to the back wall as in the previous case. At 84 ms, the drop containing cell ignites, and flame kernel is initiated. Thus, slower the drop motion, more deposition of lube oil vapor into the cell, which then leads to ignition.

In order to make the drop move to relatively rich regions, i.e. towards the center (green region) as shown in **Figure 26 (c)**, for case 3 the drop injection velocity was doubled to 5 m/s and the drop was injected later at 72 ms. This is 22 ms after the end of gas injection. **Figure 26 (c)** shows the front and top views of the drop path at various times. The higher initial drop velocity makes the drop move towards the richer (green) region. This can also be seen in **Figure 26 (i)** with refined cell equivalence ratios upwards of 0.5 just after injection. Due to the flow field disturbance created by the fan and the gas injection, the drop moves upwards and tilts slightly towards the front wall of the chamber as can be seen in snapshots at 86 ms (**Figure 26 (c)**). It then continues its vertical motion upwards until it hits the wall. The drop due to fast motion also did not ignite in this case. As a result, the

refined cell temperatures do not rise (**Figure 26 (h)**) after the initial fall due to evaporative cooling.

As part of further analysis, using the ignition case (Case 2) parameters, a non-adiabatic simulation was carried out. For the non-adiabatic simulation, a fixed wall temperature of 423 K was used. On running the simulation, no ignition was observed. The predicted drop path was similar to cases 1 and 3, where the drop was sucked upwards to the top of the chamber, which indicates that wall boundary conditions significantly affect drop ignition behavior through the change of flow field. **Figure 27 (a) and (b)** show the top view of the flow field in the plane of the drop when it is just injected for adiabatic and non-adiabatic cases respectively. The difference in location and nature of the vortices towards the left of the fan can be clearly seen. Thus, drop motion and hence ignition delay is also indirectly sensitive to pattern of heat loss variation

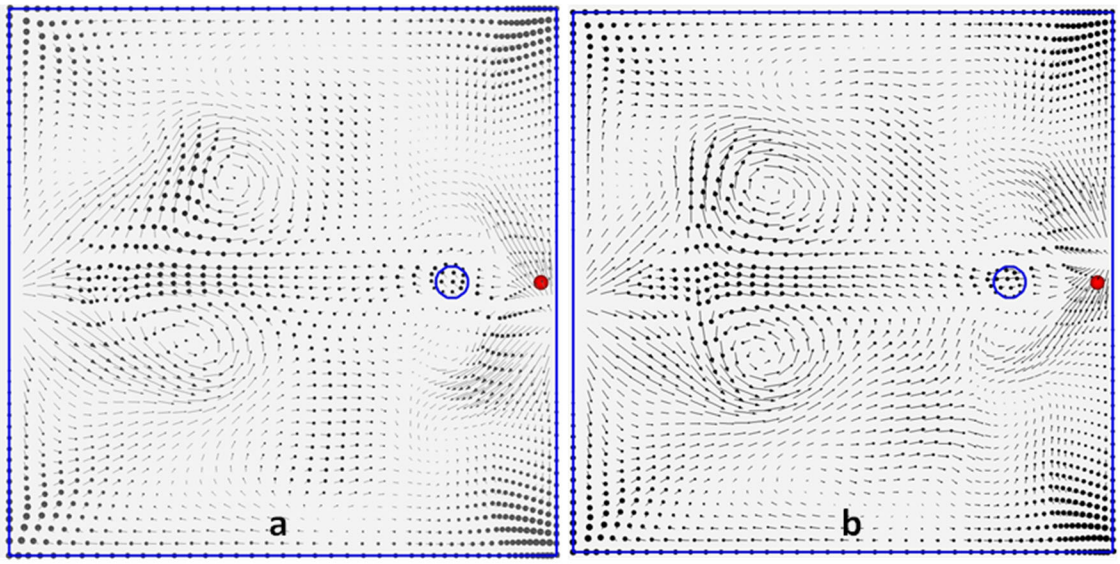

Figure 27: Flow field in plane of drop at injection a) adiabatic b) non-adiabatic

After several trials, an ignition case was obtained for a non-adiabatic case. The drop injection velocity was reduced to 2 m/s and the initial angle of injection was changed to 40 ° from the wall, instead of the original 90 ° in case 2, as shown in **Figure 28 (a)**. The overall initial internal energy was increased by 20 % to compensate for the wall heat loss. The path of the droplet is shown in **Figure 28** for times of 66 ,74, 80, 82 and 86 ms. The drop starts moving downwards but is soon redirected towards the back of the chamber. This redirection is due to the flow field created by the methane gas injection. It continues moving along and begins to suddenly decelerate around 82 ms, due to the increasing resistance from the flow in the opposite direction. This is illustrated in **Figure 28 (c)**. The droplet velocity at 82 ms along with the initial droplet injection velocity is plotted (green arrow) for comparison. This eventually causes the drop to stop and reverse its direction. Due to this motion sequence, the drop stays in a particular location for a longer time, resulting in more deposition of reactive lube vapor in the location. The vapor reaches the threshold value and ultimately ignition occurs at 85.15 ms, which confirms that the local deposition of lube oil vapor is one of the ignition driving factors.

After ignition, the flame kernel initiation is done at the center of the igniting subcell. The kernel growth is tracked by particles. **Figure 29 (a)** shows the increasing kernel radius after ignition. After 88 ms, the kernel development stage is transitioned to the turbulent flame propagation stage, where the turbulent flame speed is calculated and used to update the location of local flame front. Simulated average turbulent flame speed is shown in **Figure 29 (b)**. The flame speed decreases with time. This is mainly due to the decreasing turbulence intensity in the chamber, cancelling the effects of temperature increase of

unburned gases with increase of burned mixture. **Figure 29 (c) and (d)** show plots of decreasing turbulent kinetic energy of gas mixtures in the chamber from 95 ms to 116 ms respectively. This is also evident from **Figure 29 (e) and (f)** which indicates the laminar flame speed and decreasing ratio of turbulent to laminar flame speed with time. **Figure 30** shows the stages of flame propagation in the chamber. At 95 ms (**Figure 30 (a)**), the flame surface is relatively spherical. As the flame front propagates further, the spherical shape is lost. This change in the flame front shape can be attributed to the effect of methane gas injection and the fan on the flow field as shown in **Figure 30 (b), (c)**. **Figure 30 (c)** also shows the flame surface breaking on reaching the top wall.

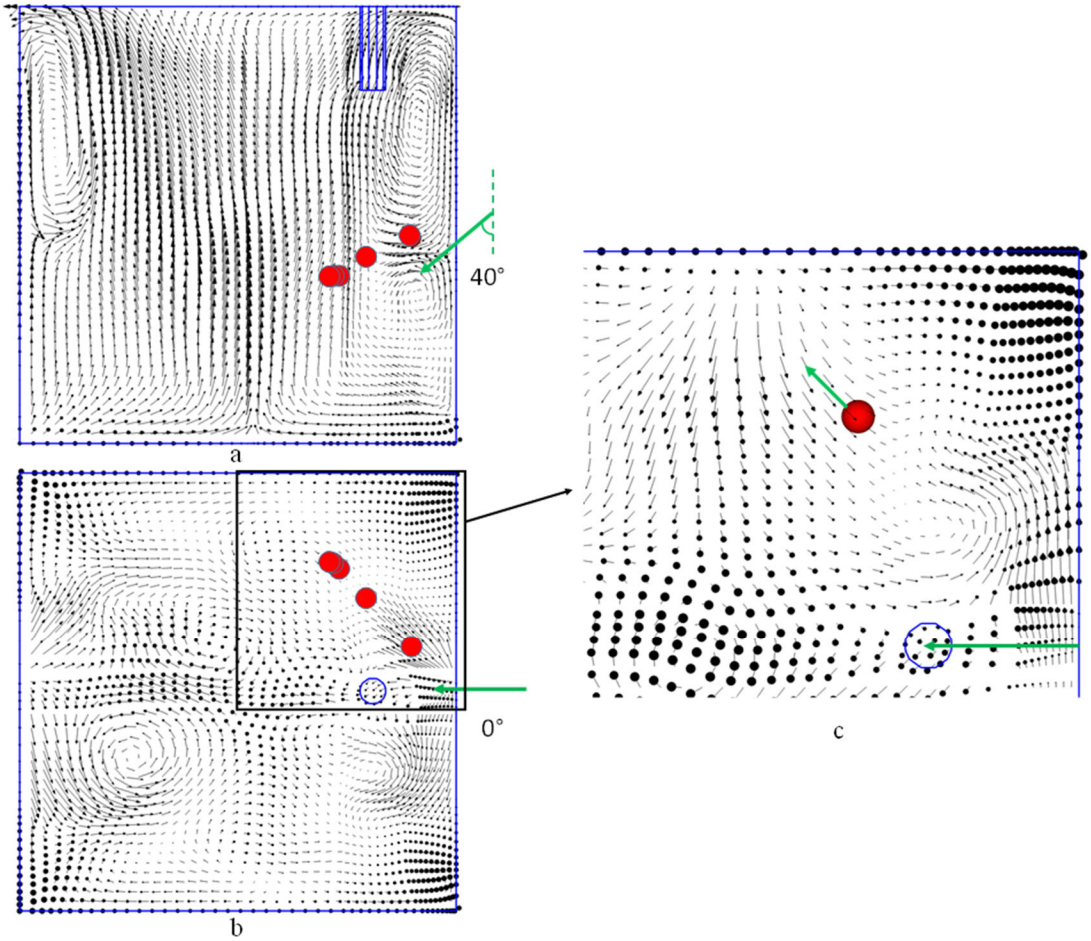

Figure 28: Drop path tracing a) front view b) top view at 66, 74, 80 82, 86 ms for non-adiabatic ignition case c) enlarged view showing flow and drop velocity at 82 ms

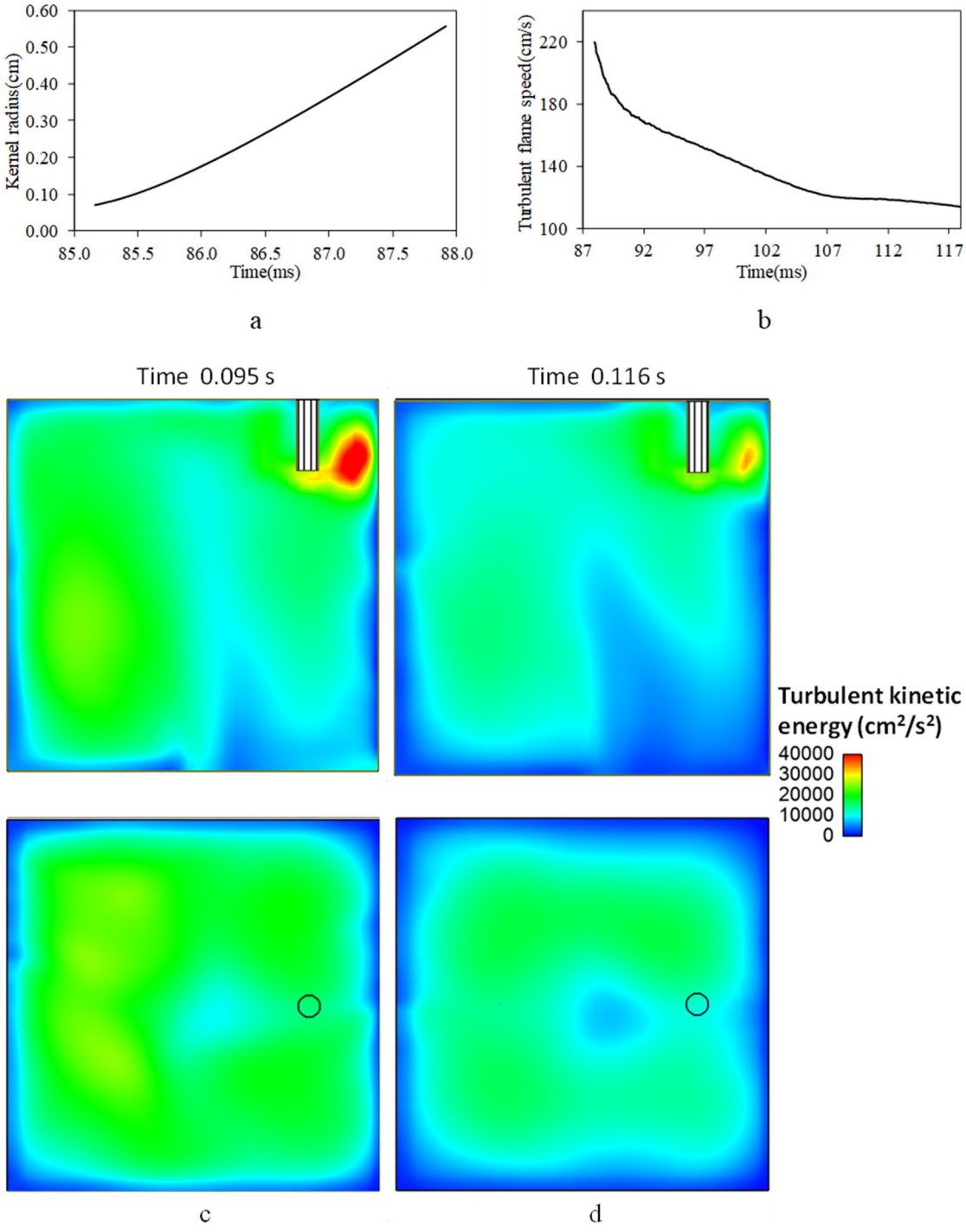

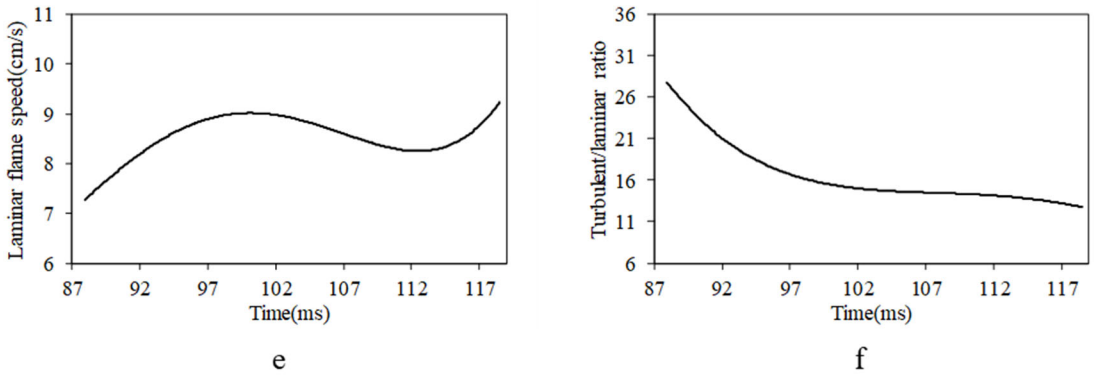

Figure 29: a) kernel growth after ignition b) flame speed after transition to turbulent flame propagation model c) turbulent kinetic energy plots in chamber at 95 ms d) turbulent kinetic energy plots in chamber at 116 ms e) Laminar flame speed f) ratio of turbulent to laminar flame speed vs time

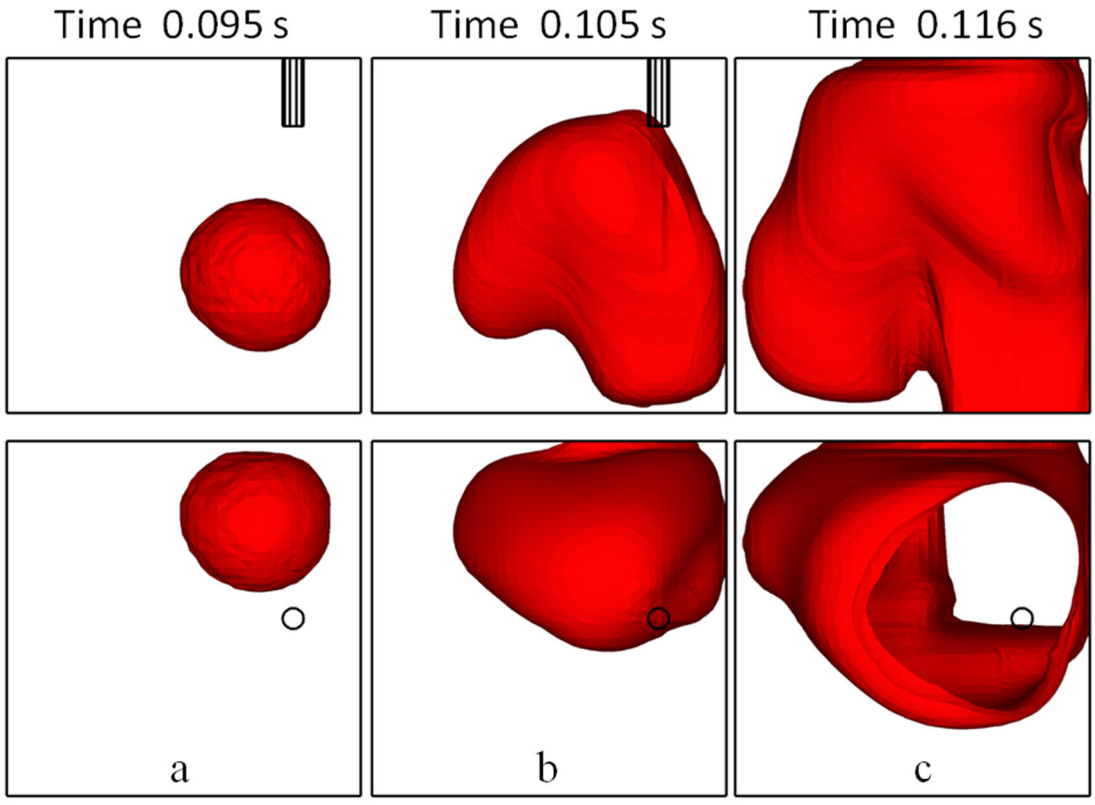

Figure 30: flame surface tracking in chamber at a) 95 ms b) 105 ms c) 116 ms

For this non-adiabatic ignition case, the sensitivity of initial drop temperature on ignition was studied. Keeping all other parameters, the same, the initial drop temperatures were varied from the original 537 K as shown in **Table 5**. All the cases showed ignition with very small variations in their respective ignition times (**Table 5**). Thus, the pre-ignition process is insensitive to initial drop temperature, once other initial drop conditions fall in favorable ranges to drive the ignition of the drop.

Table 5: Ignition time with change in initial drop temperature

Initial drop temperature (K)	Ignition time (ms)
575	85.45
550	85.69
537	85.15
533	84.89
530	84.68
525	84.87
510	85.99
500	87.43

3.1.6 Oil film dynamics

After the models relevant to the moving grids explained in **Sec. 2.1.7** and **2.1.8** were implemented, tests were conducted. A marine natural gas production grid is used for this. The grid was generated using ANSYS ICEM software. The grid specifics are shown in **Figure 31**. The head region is meshed as a separate block, with much higher resolution compared to the squish region due to the difference in the piston bowl and head geometry.

The typical cell height at Bottom dead center (BDC) in the squish region just above the crevice is approximately 1.89 cm. **Figure 31 (d)** shows how the crevice geometry is considered. The crevice has 11 and 2 layers in the Z and the radial directions, respectively. The cell height in the crevice region is 0.133 cm. **Table 6** shows the grid details.

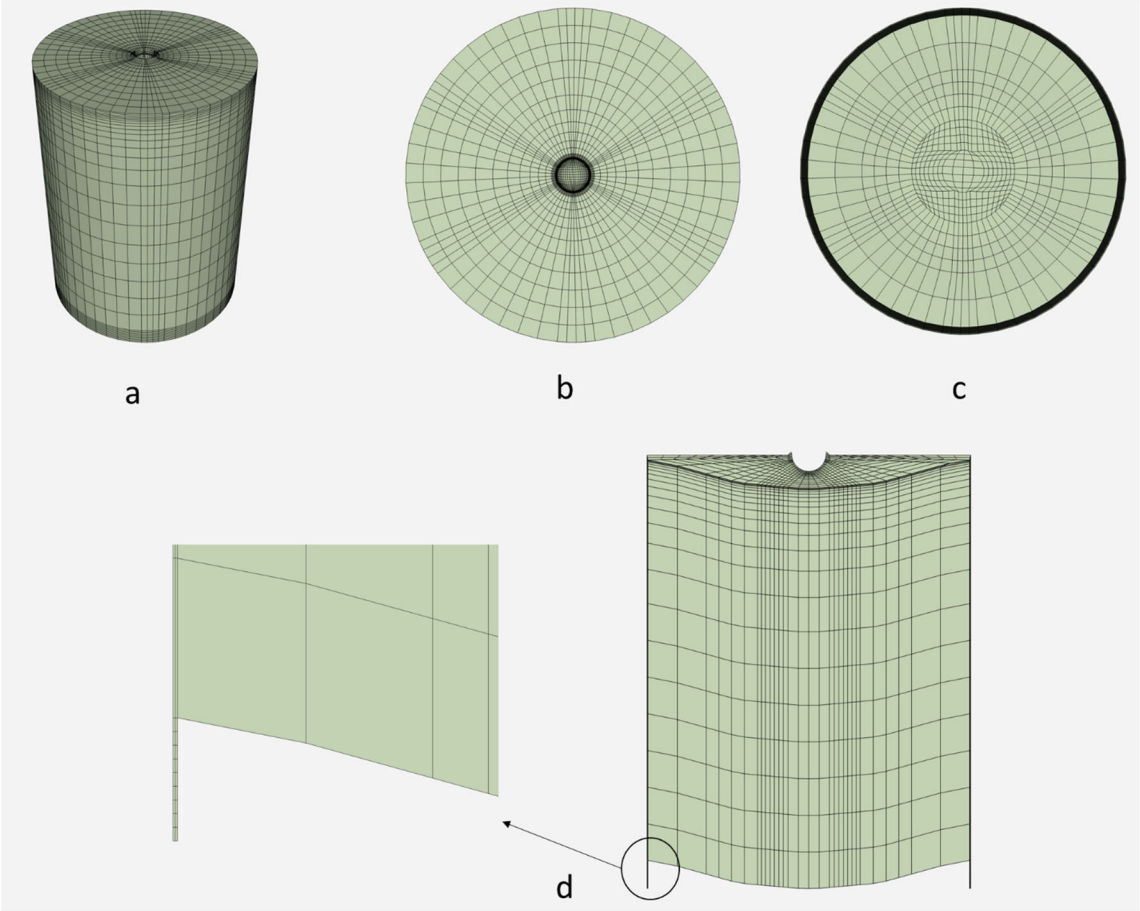

Figure 31: Grids used a) Isometric view b) Top view c) bottom view d) Cut section with crevice detail

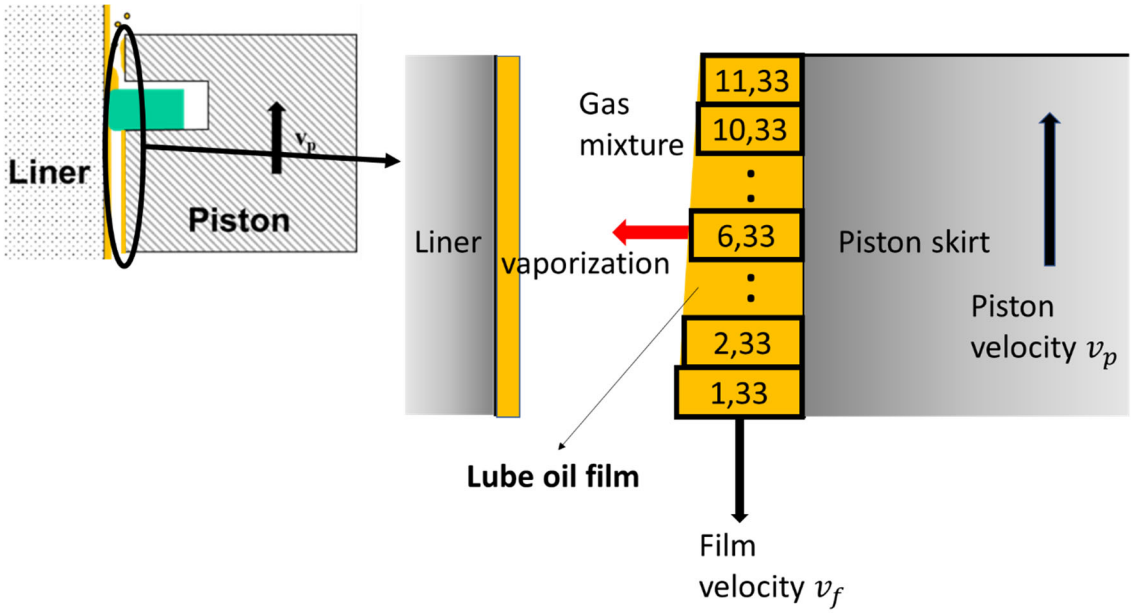

Figure 32: Zoomed in view of oil film cell dynamics

Table 6: Grid properties

Bore (cm)	17.0
Stroke (cm)	21.93
Connecting rod length (cm)	40.0
Compression ratio	12.92
Squish (cm)	0.1
Number of cells	30714
Number of vertices	33398
Crevice height (cm)	1.47

Understanding the variation of oil film thickness, temperature and velocity with piston motion is important to determine critical angle for stripping condition (**Eq. 28**). The engine speed was 60 rpm. The initial film temperature and thickness are 363.15 K and 0.019 cm, respectively. The initial film thickness is the same throughout the Z-direction. The initial ambient gas temperature and pressure at BDC (-180^{o} atdc) was 339.5 K and 1.66 bar. The ambient composition was of natural gas and air with an equivalence ratio of 0.6. The temperature of the piston skirt and liner was 510 K. The chemistry calculations were deactivated in this section to demonstrate only film motion and heating. **Figure 32** shows the zoomed in view of the simplified crevice ring gap region in the engine. To study factors affecting oil film dynamics three representative oil film cells (out of a total of 11) namely film (11,33), film (6,33) and film (1,33) are monitored. The number 33 in film (11,33) indicates the azimuthal index for the oil film. The azimuthal index 33 is considered as the ring gap column, which is expected to be the thickest because more lube oil is supplied than the other locations though the ring-gap opening. Therefore, it can be assumed that the oil film distribution on the skirt surfaces will be uniform azimuthally, except for the one column aligned with the ring gap. Only the ring gap column is of interest and is monitored here. **Figure 33 (a)** shows the comparison of piston ($\boldsymbol{v_p}$) and oil film velocity ($\boldsymbol{v_f}$) for film (11,33). The initial film velocity at BDC was zero for this case. As the piston moves up from BDC, it starts accelerating. The oil film (11,33) by virtue of its inertia slightly lags and thus has a lower velocity compared to the piston. The bottom film (1,33), compared to middle film (6,33) and top film (11,33) lags the piston the most, as all the mass flux

accumulates from the upper layers. The lag is indicated by the magnitude of negative relative velocity (**Figure 33 (b)**) of the film with respect to the piston ($\boldsymbol{v_p - v_f}$).

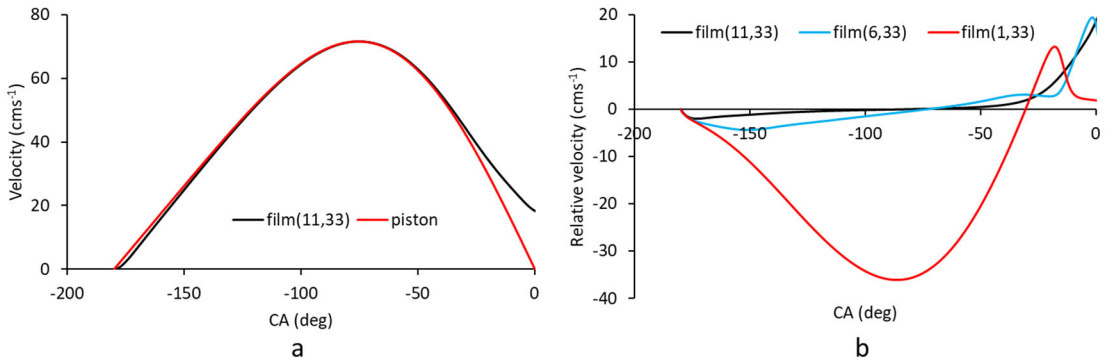

Figure 33: a) velocity of piston and film (11,33) b) relative velocity of film with respect to piston

The piston reaches maximum velocity and zero acceleration at around -75° atdc (**Figure 33 (a)**). By this time, the top oil film (11,33) has caught up with the piston as indicated by zero film relative velocity value (**Figure 33 (b)**). In contrast the bottom oil film (1,33) is lagging much behind. From -75° atdc onwards the piston starts decelerating. The film (11,33), now increasing in mass due to the accumulation of flux from the lower oil film cells, does not decelerate as quickly as the piston. This leads to larger divergence between the piston and film (11,33) velocity (indicated by larger relative velocity) at the top dead center (TDC 0° atdc).

Figure 34 (a) shows the variation of film thickness with piston motion for the corresponding film cells whose location is shown in **Figure 32**. The initial film velocity for all these cells is zero. As the piston moves upwards, by virtue of the film's inertia, with respect to the piston, mass from the upper film cells (film (11,33)) move towards the lower

ones (film (1,33)). This results in the increase and decrease of film (1,33) and film (11,33) thickness, respectively. The mid film cell (6,33) thickness lies in between the top and bottom cell thickness. Film thickness is also dependent on film temperature in addition to the mass flux motion. **Figure 34 (b)** shows the variation of the film temperatures. Film temperature increase is due to heating from the piston skirt wall which is at 510 K. The thinner upper film (11,33) heats up much faster than the thicker lower film (1,33). Once the piston crosses -50° atdc, there is a sharp decrease in thickness for film (1,33) and vice versa for film (11,33) as the mass flux within the cells reverses direction as seen by the change in sign and steepness of the slope of the relative velocity (**Figure 33 (b)**). The thickness of the mid film (6,33) increases, or decreases based on the amount of flux entering or leaving it. After -50° atdc all films show an increase in temperature as they are now heated by the ambient gas mixture, which is now greater than piston wall temperature of 510 K and increasing due to piston compression. Again, the thinner film (1,33) heats up much faster than thicker film (11,33).

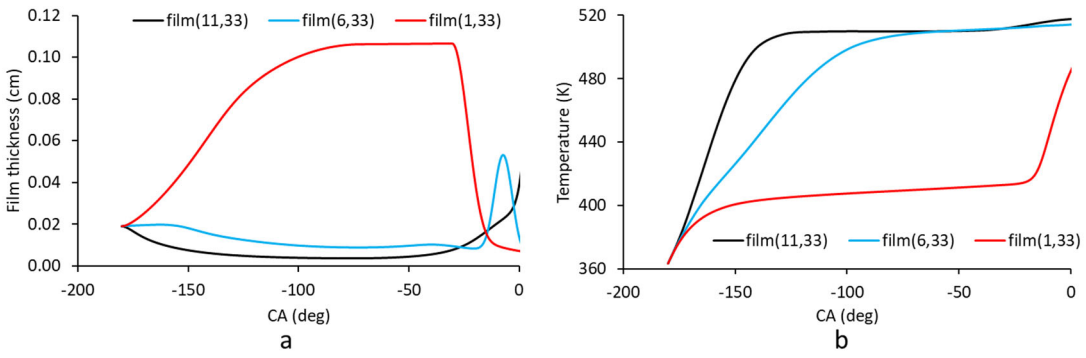

Figure 34: a) Film thickness b) Film temperature vs CA

3.1.6.1 Effect of initial film thickness

As the engine runs many cycles, piston ring or top land wear can lead to different initial film thicknesses and velocity at BDC. In this section only initial thickness is changed keeping the initial film velocity zero. The effect of reducing the initial film thickness from the original 190 μm to 140 and 90 μm is studied. Note that decrease in initial film thickness also results in decrease of film mass. **Figure 35 (a)** shows the variation of film thickness for film (11,33) with crank angle for the three initial film thickness cases. The film thickness is dependent on the net mass flux into and out of the film cell. In the case of film (11,33), as it is the last film cell, the net mass flux into the film cell is equal to the mass flux from the film cell below (i.e., film (10,33)). The mass flux from film (10,33) is directly proportional to the relative velocity of film (10,33) which is plotted vs crank angle in **Figure 35 (b)**. The net mass flux out of film (11,33) into the below film (10,33) is dependent on the relative velocity of film (11,33) which is plotted in **Figure 35 (c)**. In short, film thickness of film (11,33) increases when relative velocity of film (10,33) is positive and decreases when relative velocity of film (11,33) is negative. The thinner the initial film, the lower the relative velocity variation, meaning that it keeps up with the piston motion. From BDC to -75 atdc, the relative velocity of film (11,33) is negative for all the three cases (**Figure 35 (c)**). Thus, the film (11,33) thickness reduces as mass is transferred to the lower film (10,33). The mass transfer to the lower film (10,33) continues until the relative velocity of film (11,33) approaches 0 at -75 atdc. This is where the film (11,33) has its lowest thickness (**Figure 35 (a)**). After -75 atdc, the relative velocity of film (10,33) is positive, meaning mass is now transferred to the upper film (11,33).

Consequently, the thickness of film (11,33) increases until TDC, tracking the behavior of the relative velocity of film (10,33). **Figure 35 (d)** shows the film temperature variation for the three initial film thickness cases. The thinner initial film (90 μm) heats up faster and reaches the piston skirt wall temperature of 510 K compared to the thicker 190 μm film. After -30 atdc, the film (11,33) temperature is increased due to heating from the ambient gas.

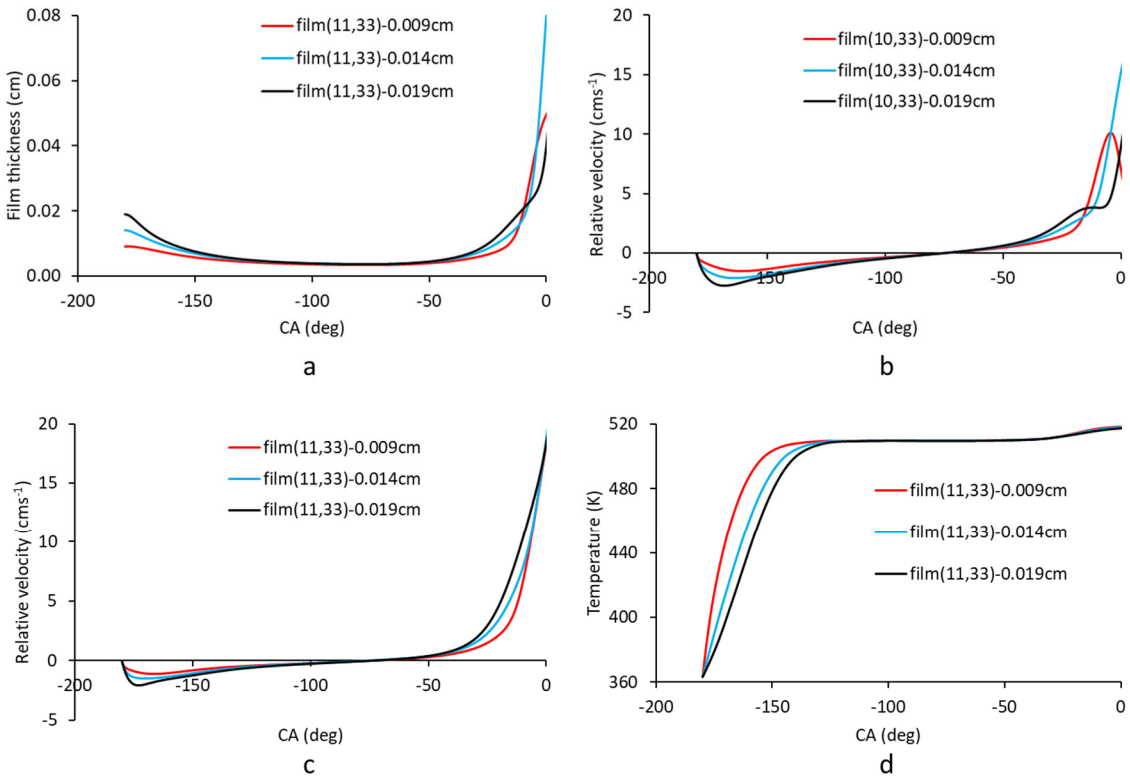

Figure 35: Effect of initial film thickness on a) film (11,33) thickness, b) relative velocity of film (10,33), c) relative velocity of film (11,33), d) film (11,33) temperature

3.1.6.2 Effect of initial film velocity

Until now for all cases discussed the initial film velocity was zero at BDC. In this section, the initial film thickness is kept constant at 190 μm and two initial film velocities of 80

cm/s and 40 cm/s are compared with the earlier 0 cm/s (stationary) case. Note that all the oil film cells are initialized to the same initial velocity value. **Figure 36 (a) & (b)** shows the relative film velocities of film (11,33) & film (1,33) for three initial film velocity cases. For 80 cm/s and 40 cm/s cases the film (11,33) is initially moving upwards faster than the piston as indicated by the positive relative velocity. **Figure 36 (c) & (d)** shows the film (11,33) and film (1,33) thickness variation. For film (11,33) due to the positive relative velocity of film (10,33) at BDC as shown in **Figure 36 (e)**, there is mass influx. This causes sharp increase in the film (11,33) thickness proportional to the initial film velocity. This sharp increase in the mass/thickness of film (11,33) causes its relative velocity to decrease from its initial value at BDC. The thickness of film (11,33) stabilizes as seen by the plateau in the black (80 cm/s) & blue (40 cm/s) curve at (-172° to -125° CA) & (-174° to -125° CA) respectively in **Figure 36 (c)** due to the steep drop of relative velocity of film (10,33) in the corresponding periods (**Figure 36 (e))** from its initial values. Once the relative velocity of film (11,33) becomes negative, its thickness starts to decrease as it loses mass to the lower film (10,33). This happens at around -125° and -155° CA for the black (80 cm/s) and blue (40 cm/s) curves respectively. The film (11,33) thickness remains stable again (black-(-109° to -31° CA), blue-(-140° to -3° CA) as the relative film (11,33) velocity approach zero. Finally, once relative velocity of film (10,33) becomes positive again and starts increasing (below -50° CA for black) as seen in **Figure 36 (e),** film (11,33) thickness begins to rise again before TDC. Similarly for the blue curve (40 cm/s), the rise is delayed and just begins at TDC. The bottom film (1,33), in **Figure 36 (d)**, initially at BDC loses mass (thickness decreases) to film (2,33) above it, due to positive relative velocity of film

(1,33). However, the positive relative velocity of film (1,33) and film (2,33) [**Figure 36 (b) & Figure 36 (f)**] immediately falls to zero and becomes negative. This again causes the mass flux from the above film (2,33) back into film (1,33) increasing its thickness again (**Figure 36 (b) & (d)**). As the relative velocity of film (2,33) gets closer to zero (at ~ -75 CA), the thickness of film (1.33) stabilizes. Eventually due to the positive relative velocity of film (1,33), the thickness starts decreasing again (-45° CA for 80 cm/s, -27° CA for 40 cm/s) as it loses mass to the upper film (2,33). As the piston moves closer to TDC, the larger initial film velocity cases (80 cm/s, 40 cm/s) are seen to have larger relative film (11,33) velocity and thickness, which also increases the probability of lube oil stripping as indicated by **Eq. 28**.

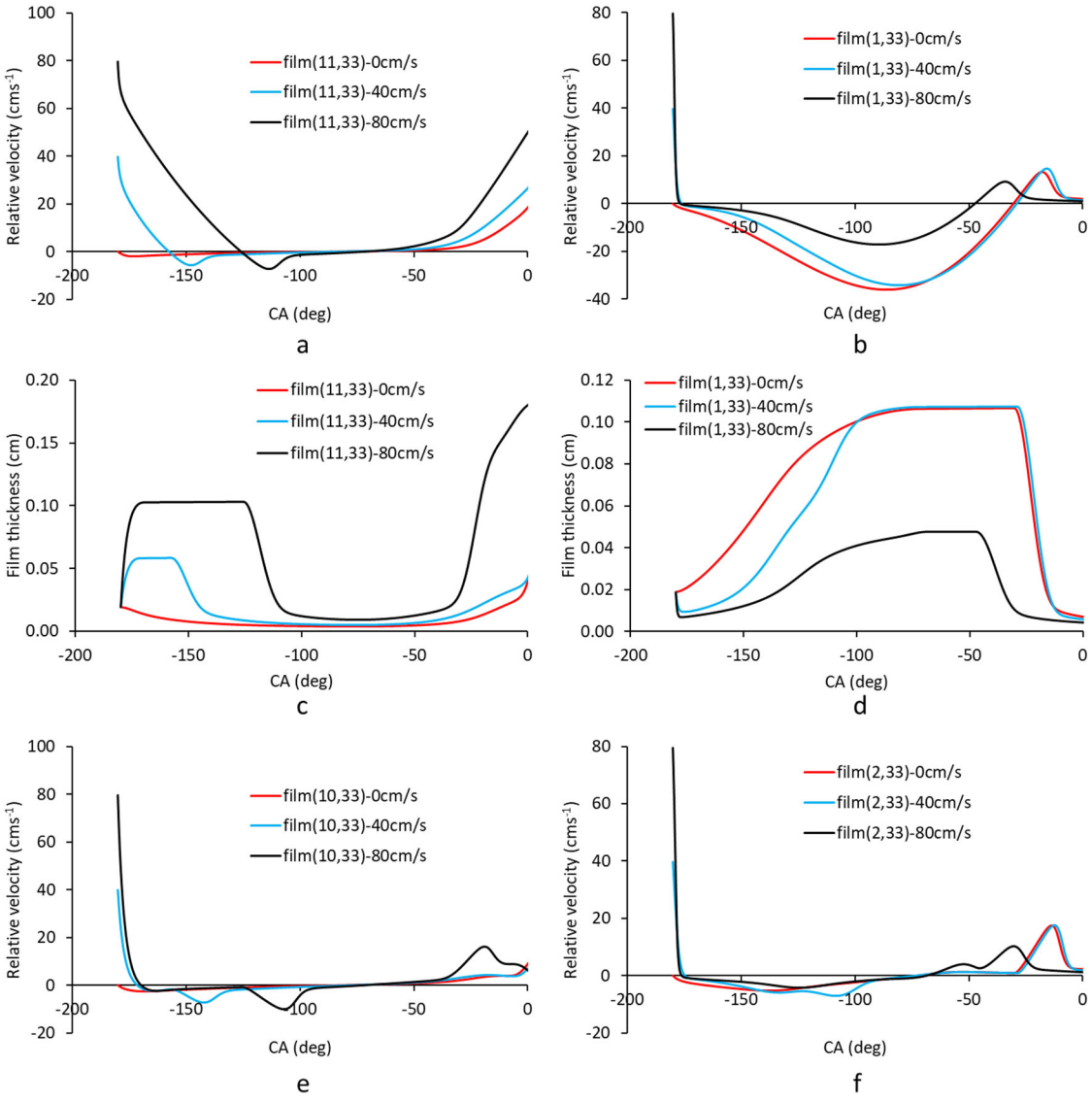

Figure 36: Effect of initial film velocity on a) relative film (11,33) velocity, b) relative film (1,33) velocity, c) film (11,33) thickness, d) film (1,33) thickness, e) film (10,33) relative velocity, f) film (2,33) relative velocity

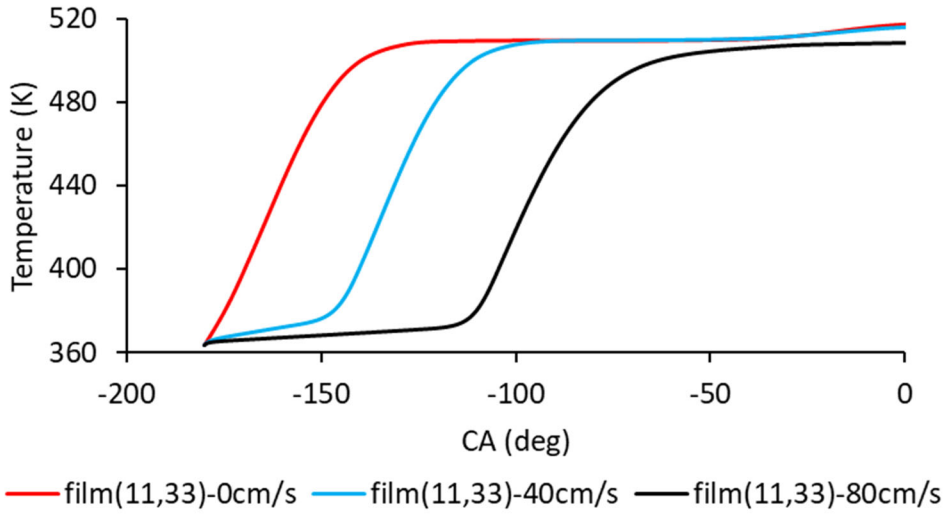

Figure 37: Effect of initial film velocity on film (11,33) temperature

Figure 37 shows the variation of film (11,33) temperature. The thinner film case (0 cm/s) has faster rise compared to thicker 80 cm/s case. The 40 cm/s case expectedly lies in between the 0 and 80 cm/s case.

3.1.7 Lube oil stripping

The α_{geo} angle for grid 1 shown in **Figure 31** is 90° ($\frac{\pi}{2}\ radians$). The droplet stripping conditions is satisfied if the critical angle, which is calculated every cycle of the simulation for the top film cell (film (11,33)) is less than $\frac{\pi}{2}$. In **Eq. 28,** U_{film} is the relative film (11,33) velocity, h_{film} is the film (11,33) thickness and ω_m is the maximum wave growth rate computed. For the zero initial film velocity cases with different initial film thickness, (namely 190 μm and below) no stripping occurred from BDC (-180° atdc) to TDC (0° atdc). Note that film thickness in actual marine engines is in the range of 10 μm for the 1st top land/ring [52], much smaller than the shown cases (90 μm, 190 μm). Possibility of

higher film thickness may be present in the ring-gaps of the piston rings which is the main source of thicker films leading to stripping. For different initial film velocity cases the critical angle for initial film thickness of 190 μm is shown in **Figure 38.**

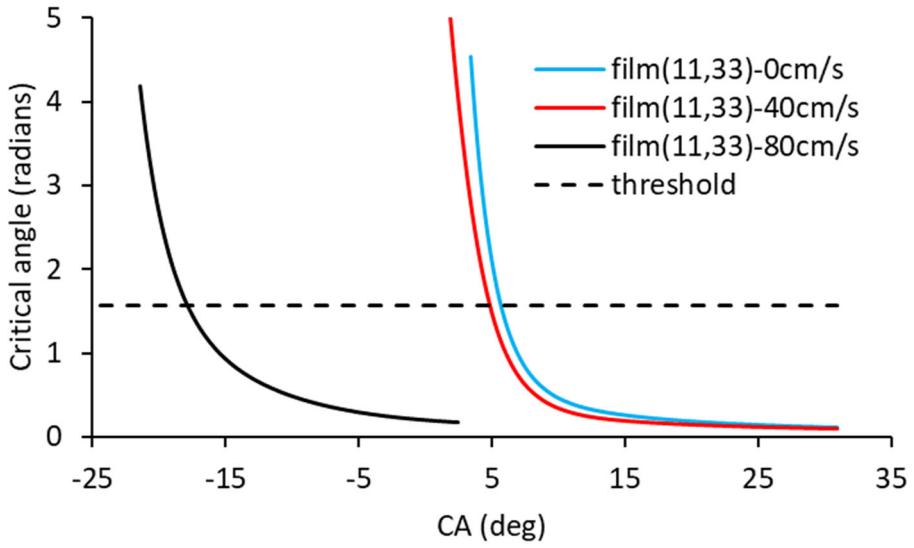

Figure 38: Critical angle vs CA for different initial film velocity of film (11,33)

The critical angle is calculated and plotted only when $\omega_m > 0$ and can be computed. For example, in **Figure 38** for 80 cm/s below -20° atdc ω_m is negative, hence not computed and is not shown.

Stripping occurs before TDC (0° atdc) at -17.9° CA only for 80 cm/s case as the critical angle goes below $\frac{\pi}{2}$ which is indicated by the threshold line in **Figure 38**. For the other cases it happens after TDC, which is not of interest because it is likely to be after the start of ignition timing. This indicates that lube oil stripping is a rare event and occurs in a combination of high initial film thickness and velocity.

3.1.8 SPIC model in engine

Although many cases/simulations were run, only the ignition case will be presented and studied. The initial film thickness and film velocity were 190 μm and 80 cm/s, respectively. The piston skirt temperature was 590 K (increased from 510 K in **Sec. 3.1.6**). Stripping occurs when the computed critical angle is less than $\frac{\pi}{2}$, which is at -20.97° CA. At stripping condition, the injected parcel radius is calculated using **Eq. 29**. The calculated parcel radius is 482 μm. Based on the drop and cell size, refinement level 1 (8 sub cells) was chosen. The film (11,33) temperature is used as the parcel injection temperature. This value was 579 K (note piston skirt temperature 590 K). The parcel injection location was the 33rd cell azimuthally as shown in **Figure 39 (a)**. The parcel was injected at 135 ° angle to the z-axis as shown in **Figure 39 (b)**. The parcel in this figure is not to scale and is shown in red. The head and piston grid details can also be seen. The total number of drops in a parcel was 26. Thus 1 parcel representing 26 drops is injected. The injection velocity vectors for the parcel, which were calculated from the film (11,33) velocity in the x, y, z directions were 41.11, -44.20 and 19.37 cm/s, respectively.

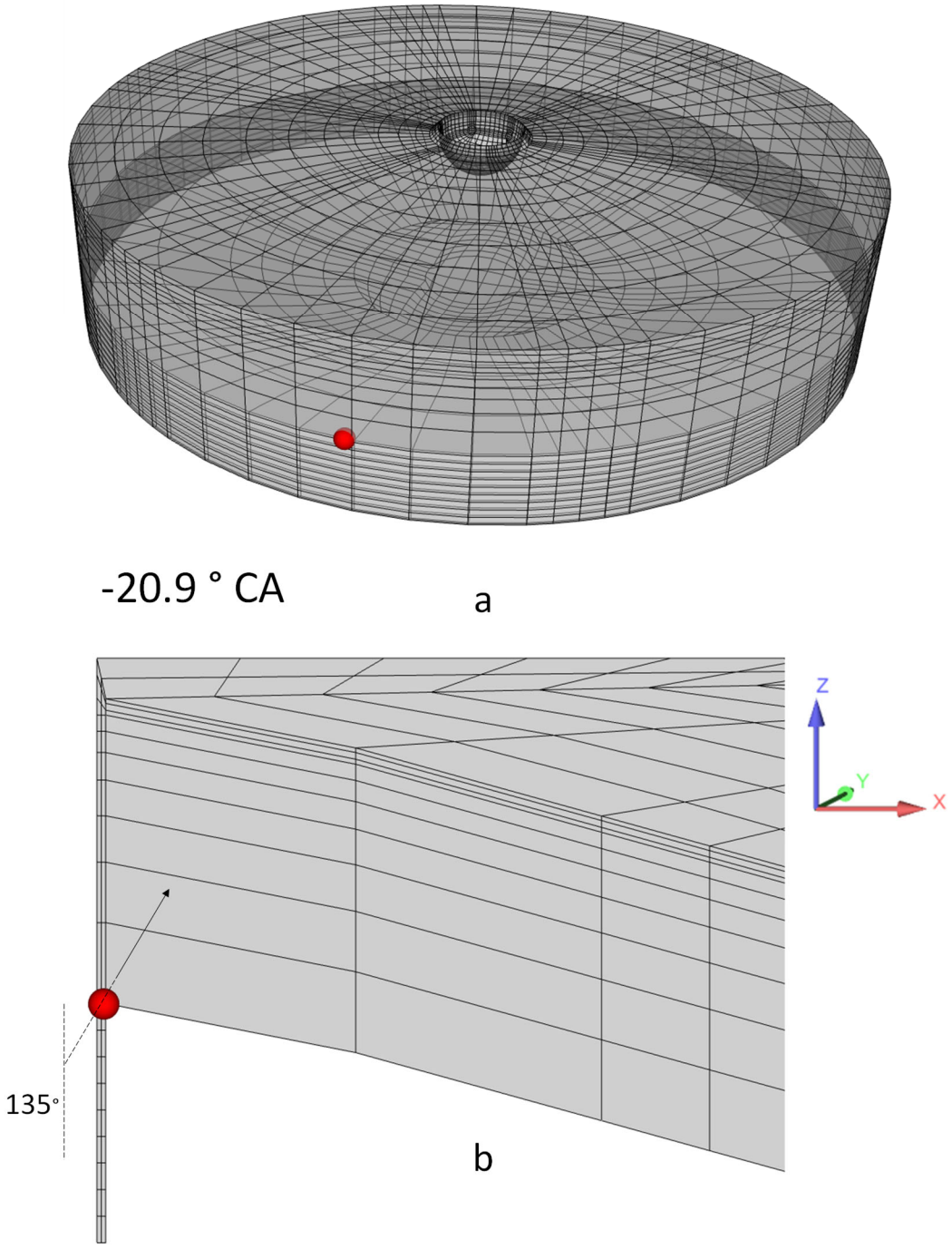

Figure 39: Stripped parcel (not to scale) injection detail a) 3D grid, b) at cut plane y=0

Figure 40 shows the progress of the lube parcel after stripping into the combustion chamber at the cut plane y=0. The grid lines represent the parent cells. Before stripping the

chamber contains only methane and air at an equivalence ratio of 0.6. Once the parcel is stripped at -20.97° CA, it moves from the wall region cells into the interior squish region, vaporizing along its path. **Figure 40 (a)** shows the diffusion and advection of lube vapor (mass fraction) from the stripped drop at -18° CA. **Figure 40 (b)** shows the corresponding temperature field. The cells near the liner and crevice are cooler than the core, due to heat loss to the wall. As the parcel moves further into the chamber, the lube vapor starts getting consumed as shown by the light blue shade in **Figure 40 (c)** at -9 ° CA. **Figure 40 (d)** shows the parcel now moving towards the core region having higher temperature. Close to TDC, i.e., -3 ° CA, the drop reaches the head region of the engine, and most of the lube vapor initially deposited is reacting (consumed) as seen in **Figure 40 (e)**. The ambient temperature at -3° CA as seen in **Figure 40 (f)** is approximately equal to 860 K. However, the cell just above the piston, where the stripped parcel initially deposited lube vapor (circled in **Figure 40 (f)**) has a higher temperature comparatively. This is due to the reacting lube vapor. The lube vapor in this cell eventually leads to pre-ignition as will be discussed in the following paragraphs. The parcel temperature rises from 579 K to 600 K as the piston reaches TDC, which is shown in **Figure 41 (a)**. The parcel radius variation is shown in **Figure 41 (b)**. Though the parcel vaporizes, its radius increases due to the increase in its temperature, and thus the decrease in its density.

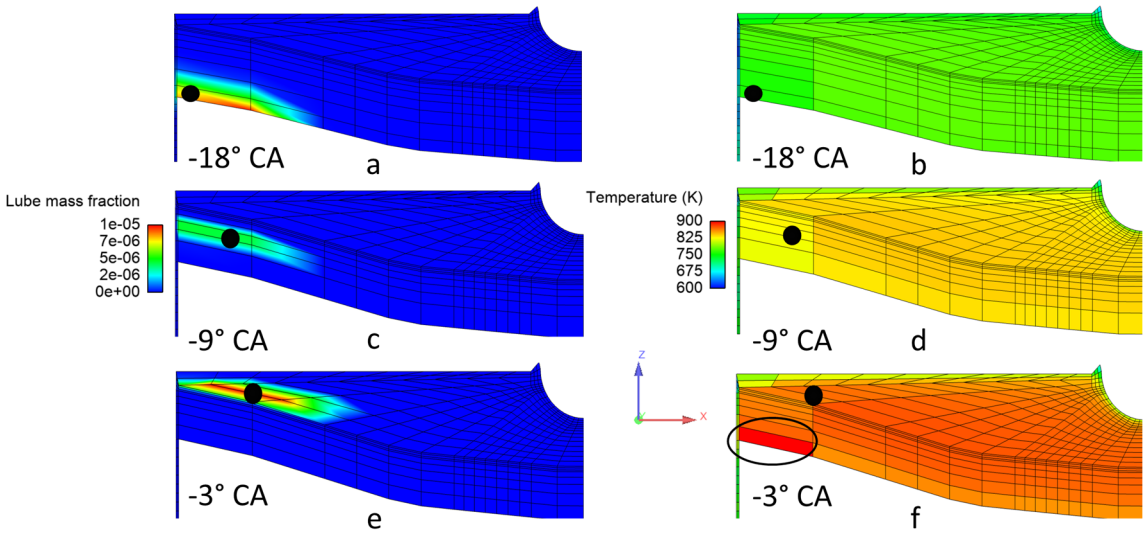

Figure 40: Cut plane y=0 distribution with parcel (black) of a) lube mass fraction b) parent cell temperature at -18° CA, c) lube mass fraction d) parent temperature at -9 ° CA, e) lube mass fraction b) parent cell temperature at -3° CA

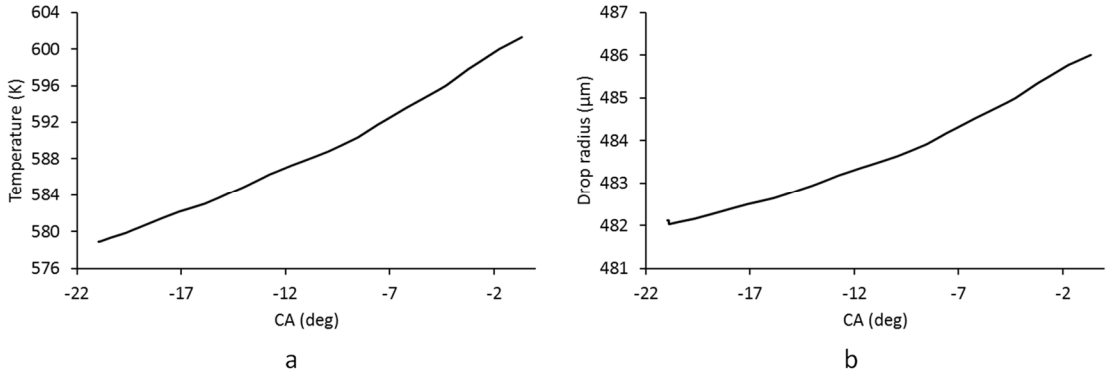

Figure 41: Variation of a) injected parcel temperature b) injected parcel radius with crank angle

Figure 42 (a) shows the equivalence ratio variation for refined and parent cells containing the parcel. At -20.97° CA before the parcel is stripped, the chamber contains methane (natural gas)/air mixtures at an equivalence ratio of 0.6. Once the parcel is stripped and evaporation begins, the lube vapor is assigned to refined cells as explained in Ref.[11]. The refined (red) cells equivalence ratio curve is steeper than the parent cell (blue) curve, as the

lube vapor is modeled to be uniformly distributed in the parent cell, which is 8 times larger. The sudden fall in the curves (blue and red) indicates that the parcel has moved to the next refined/parent cell. Two grid snapping events take place at -17.70° and -10.47°CA. The effect of snapping at -17.70° CA on the equivalence ratio is shown by black circles in **Figure 42 (a)**. The new values after snapping are calculated as explained in **Sec. 2.1.7.1.** There is a drop in equivalence ratio of both the parent and refined parcel-containing cells as grid snapping artificially diffuses the lube vapor when the two layers are combined into one. As the piston moves closer towards TDC, the equivalence ratio spikes become much shorter and steeper. The increase in steepness is due to the higher temperature of the core (which in turn heats the parcel) and the increase in temperature is due to compression. The shorter duration is due to the smaller size of the cells in the core region, compared to the outer chamber. **Figure 42 (b)** shows the comparison of the refined and parent cell temperatures of the parcel-containing cell. Overall, there is an increase in the temperature due to compression and the parcel's moving closer to the hotter center of the chamber (**Figure 40**). The decrease in the cell temperature as the parcel progresses in a new cell is due to evaporative cooling and it is more pronounced in the refined cells due to its smaller heat capacity ($1/8^{th}$ of parent). As piston reaches closer to TDC, the average temperature reaches 860 K.

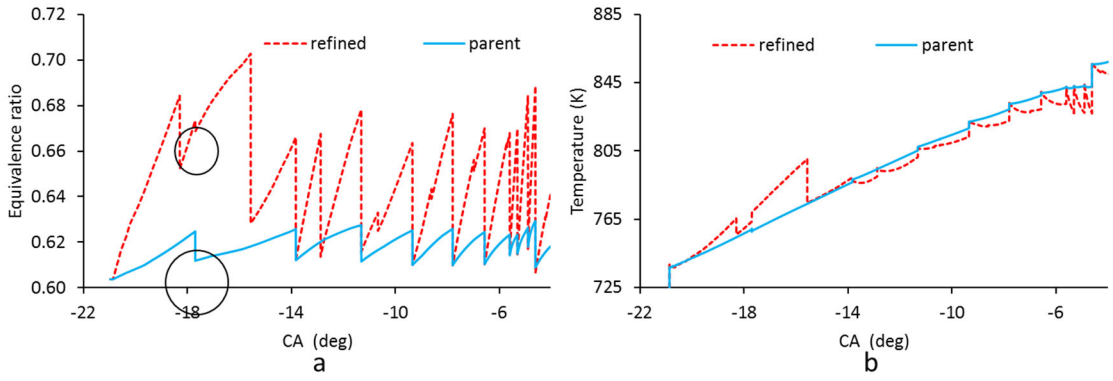

Figure 42: a) Equivalence ratio b) Temperature variation of parcel-containing cell vs crank angle

The cell into which the parcel was injected, pre-ignites (refined cell reaches 2000 K) at -3.13 CA. The igniting parent cell is shown in **Figure 43** by the red legend. On reaching pre-ignition, the center of the igniting refined cell is chosen as the kernel initialization point for flame propagation as explained in Ref. [11].

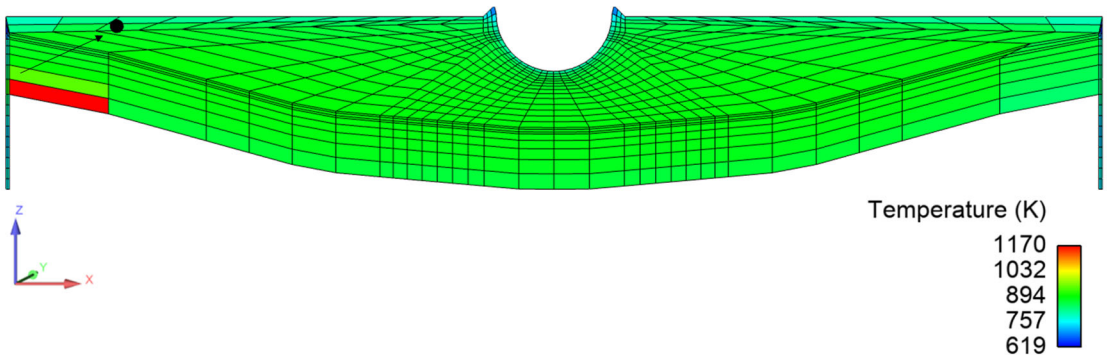

Figure 43: Igniting parent cell (red legend) location in the chamber at 0 CA

Figure 44 shows temperature profile of the igniting refined cell from -10 CA onwards. Once the temperature crosses 1000 K, there is an exponential rise to reach 2000 K within 1 CA. The factors leading to pre-ignition for this cell are attributed the following reasons.

1) Firstly, higher parcel temperatures increase the chances for pre-ignition. The higher vapor pressure due to higher parcel (surface) temperature results in increase in shedding of lube vapor. The stripped parcel temperature is subject to the piston skirt wall temperature. The piston skirt wall temperature was raised from 510 to 590 K to obtain a pre-ignition case.

2) As the stripped parcel spends most of its time in this (igniting) cell, the most lube vapor is added to the cell, which can be seen from the initial high peaks in **Figure 42**. Thus, a parcel must be moving slowly, so it can deposit lube vapor and create a locally rich region. Drawing from the same argument, highly turbulent flow field with swirl would move the parcel quickly and tend to hinder ignition.

3) Although lube vapor is highly reactive, it requires sufficient time to react to reach ignition temperatures of 2000 K. In the current case, as the igniting cell was the first cell into which the stripped parcel was injected, it has ~ 21 CA before TDC to react which is more time compared to other higher temperature core region cells, into which the parcel enters much later.

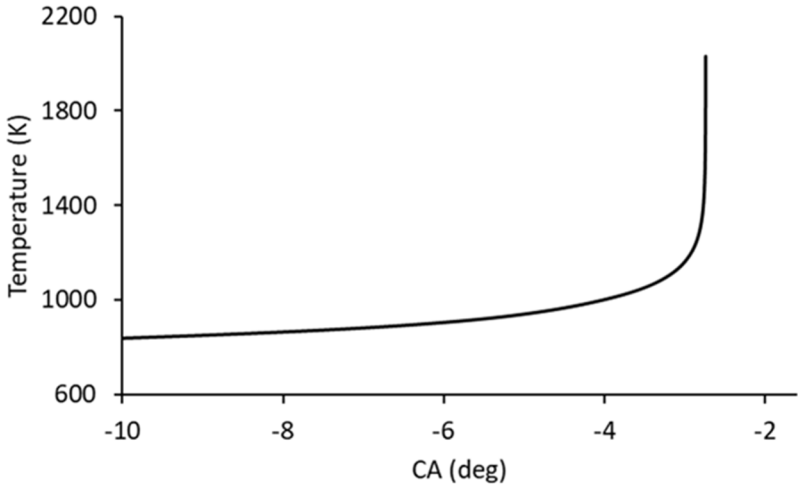

Figure 44: Igniting refined cell temperature vs crank angle

3.2 Wall film evaporation

The heat flux calculation models explained in **Sec. 2.2.2** to **Sec. 2.2.4** were implemented in an in-house version of CFD code. The computational grid of a long channel was used, which (shown in **Figure 45**) has a x-y-z dimension of 100 cm x 5 cm x 5 cm. The grid size of one cell in the z and y direction was 1 cm and, in the x direction was 20 cm. The wallfilm indicated by red circle is placed in one of the computational cells (shown in **Figure 45**-size is not to scale). The resolution of the cells was intentionally chosen such that, it was large enough to provide enough thermal capacity for the evaporation of the local wallfilm. For all the cases presented in this work the initial ambient pressure and temperature was 2 bar and 600 K, respectively. The initial ambient air composition used is shown in **Table 7.** The transient numerical simulation was run from initial conditions up to a time of 13 ms. At time 0, the steady state velocity profile of channel flow shown in **Figure 46** was initialized. The wallfilm was placed in the third cell (indicated by black dot in **Figure 46**) at 10 ms.

Table 7: Initial composition of ambient gas

Species	Mole fraction
O_2	0.215
N_2	0.785

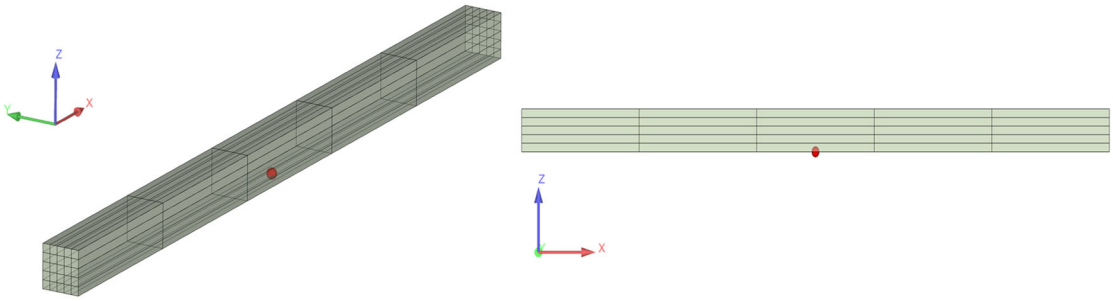

Figure 45: Isometric and section views of a square channel with wallfilm

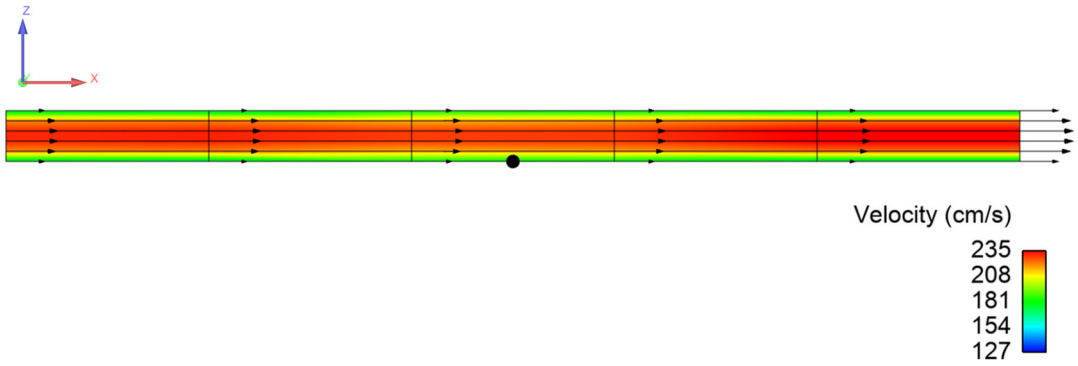

Figure 46: Steady state velocity field in wallfilm containing x-z cut plane

The steady state entrance velocity just above the wallfilm was approximately 217 cm/s. For study of single component liquids, iso-octane (iC_8H_{18}) [denoted by iC8 henceforth] and n-heptane (nC_7H_{16}) [denoted by nC7 henceforth] are chosen. The composition of

multicomponent liquid was chosen as 50-50 blend of n-heptane and iso-octane (50nC7/50iC8), i.e., 50 % n-heptane and 50 % iso-octane ($50nC_7H_{16}/50iC_8H_{18}$) by mass. For these, the initial wallfilm interior temperature was 298 K with wall temperature of 295 K (cold wall condition). The saturation temperatures for nC_7H_{16}, iC_8H_{18} and $50nC_7H_{16}/50iC_8H_{18}$ were 396.46 K, 398.33 K and 397.31 K, respectively. Lewis number within the boundary layer (**Figure 18**) needed to compute external heat flux is calculated as explained in Appendix **5.2A.2** and plotted for Nu-Le model in **Figure 47 (b)**. For all three compositions, Lewis numbers are greater than unity and show similar trends with time. Lewis number is affected by the boundary layer temperature. This temperature is calculated by weighted average having one-third contribution from the ambient gas temperature (**Figure 47 (a)**) and the other two-third contribution from the wallfilm surface temperature (**Figure 48 (a)**). The variation of ambient gas temperature with time is shown in **Figure 47 (a)**. The ambient temperature decreases with time, because of the latent heat used for wallfilm evaporation. The variation of the Lewis number components, namely thermal conductivity, density, specific heat and diffusivity is shown in **Figure 49 (a-d)**, respectively. All these properties decrease with time, due to decrease in the boundary layer temperature, thus increasing the Lewis number. The wallfilm interior temperature profiles of the three liquid compositions are shown in **Figure 48 (b).** The wallfilm interior temperature initially decreases rapidly due to heat loss to the cold wall which is at 295 K. It then reaches a steady temperature slightly above 295 K. Throughout the transient period the temperatures of 50nC7/50iC8 case lie in between those of nC7 and iC8 cases. **Table 8** gives the quantitative comparison of the temperatures for the three cases at 13 ms.

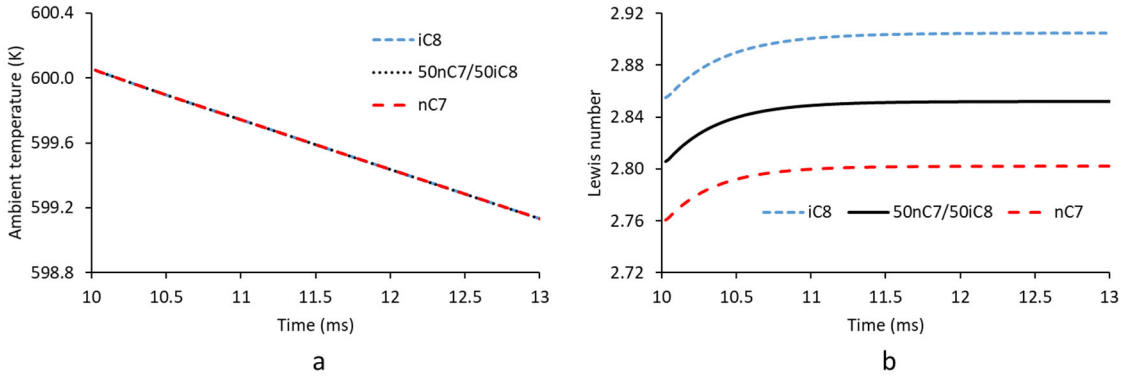

Figure 47: a) Ambient temperature variation, b) Lewis number variation for NU-Le model

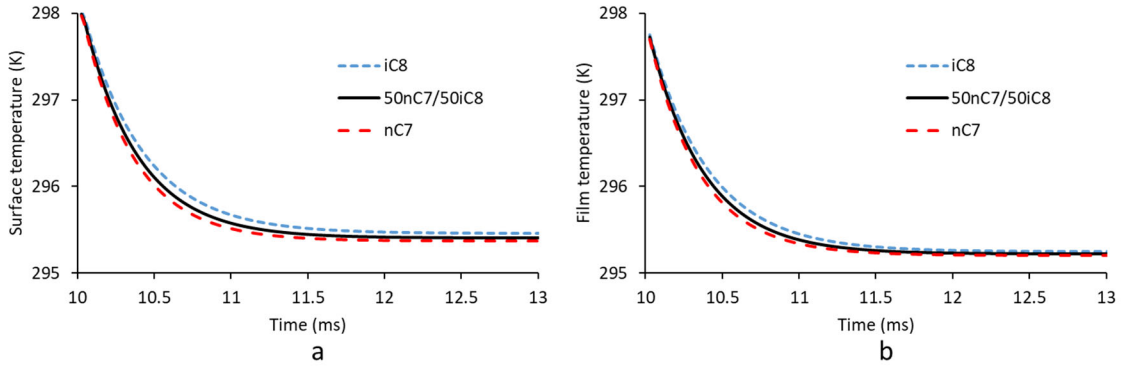

Figure 48: a) Wallfilm surface temperature variation for NU-Le model, b) Wallfilm interior temperature variation for NU-Le model

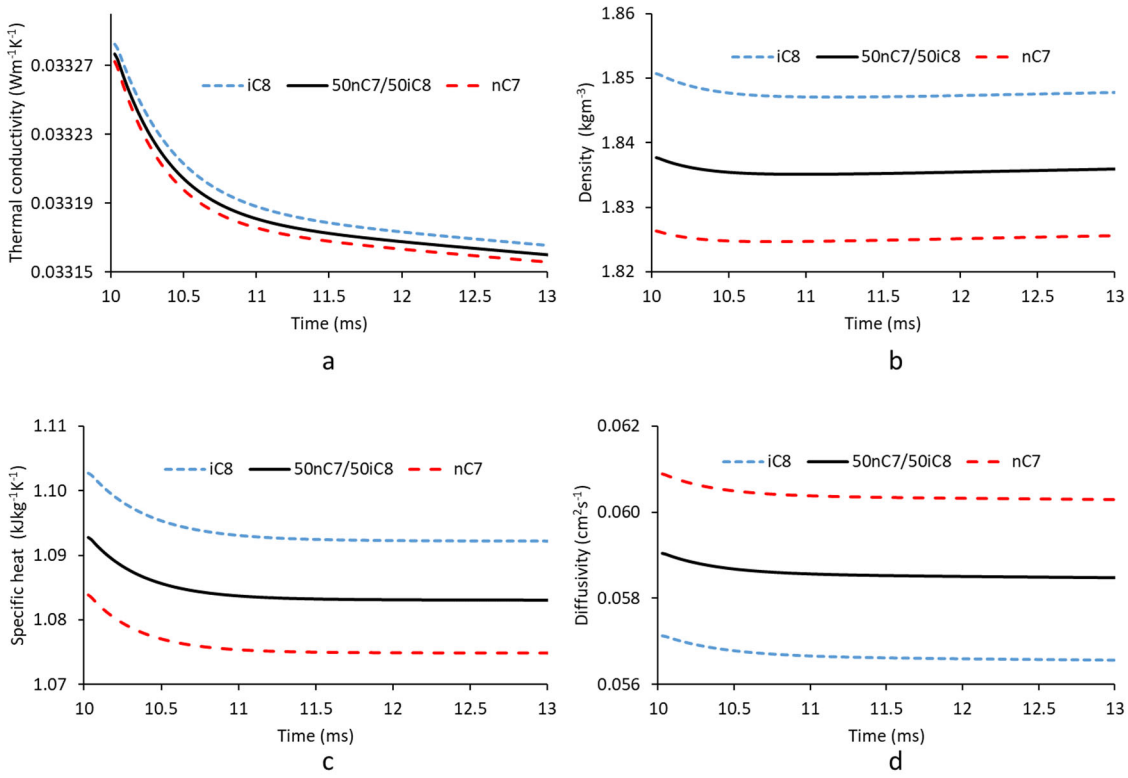

Figure 49: Variation of properties used in Lewis number a) thermal conductivity, b) density, c) specific heat, d) diffusivity

Table 8: wallfilm surface and wallfilm interior temperatures at 13 ms

	nC7	iC8	50nC7/50iC8
T_s (K)	295.37	295.46	295.41
T_f (K)	295.20	295.25	295.22

Figure 50 (a) shows the external heat flux variation with time for U-Le model, NU-Le model, and NU-Le model with correction (NU-Le-corr). All the models capture the increasing transient behavior of external heat flux. In terms of relative quantitative comparison of external heat flux at 13 ms, NU-Le-corr and U-Le model are 7.8 % higher and 0.41 % lower than NU-Le model. The 7.8 % difference between NU-Le-corr and NU-

Le models is due to the different assumptions made in the derivations (**Sec. 2.2.2/Sec. 2.2.3**). On the other hand, the 8.21 % difference between U-Le and NU-Le-corr models is attributed to the effect of varying Le number, i.e., non-unity Lewis number effect. In other words, at 13 ms, the Lewis number effect on external heat flux is 8.21 % for this n-heptane setup. **Figure 50 (b)** shows the wallfilm surface temperature (T_s) and wallfilm interior temperature (T_f) for nC7 case using NU-Le model. The wallfilm interior temperature is the temperature at half the thickness of the wall film. T_f initially is 298 K. On solving the interface energy equation, T_s is estimated. As the ambient temperature (T_∞) is 600 K, T_s is always greater than T_f. The transient pattern of both T_s and T_f eventually settles close to the wall temperature which is kept constant at 295 K.

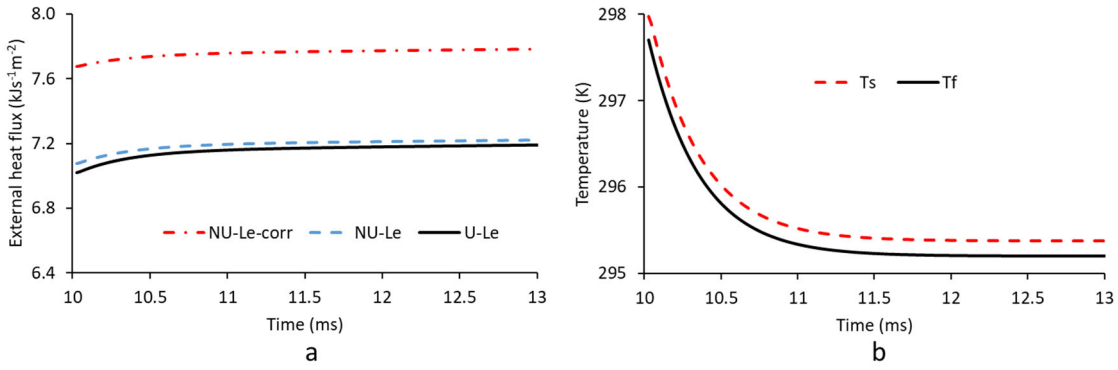

Figure 50: a) External heat flux for neat n-heptane, b) wallfilm surface and wallfilm interior temperature for neat n-heptane for NU-Le model

Figure 51 (a) shows the external heat flux of the models for iC8 case. The pattern and the quantities are very similar to nC7 case. This is due to iC_8H_{18} and nC_7H_{16} having very similar vapor pressures. At 13 ms, the relative comparison of external heat fluxes of NU-Le-corr and U-Le models to NU-Le was 9.02 % higher and 1.26 % lower, respectively. The difference between NU-Le-corr and U-Le models is 10.28 %, indicating the effect of

Lewis number. In **Figure 51 (b)**, the value of T_f and T_s at 13 ms is 295.25 K and 295.46 K (also shown in **Table 8**), respectively. **Figure 52 (a)** shows the external heat flux for 50nC7/50iC8, and at 13 ms, the relative comparison of external heat fluxes of NU-Le-corr and U-Le models to NU-Le model was 8.3 % higher and 0.75 % lower, respectively. The Lewis number effect on the external heat flux is 9.05 %, which lies in between the neat film cases (nC7-8.21 %, iC8-10.28 %). **Figure 52 (b)** shows the comparison of multicomponent fuel composition on external heat flux for NU-Le model. The heat flux of the multicomponent case lies between the single component values.

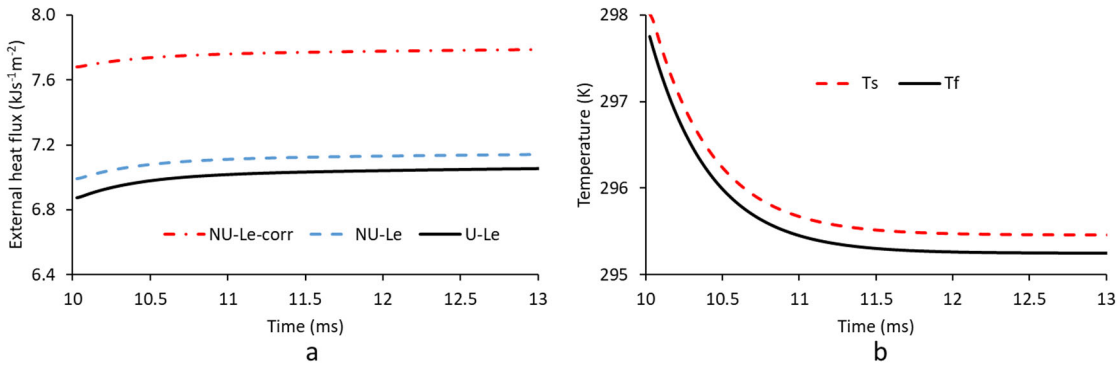

Figure 51: a) External heat flux for neat iso-octane, b) wallfilm surface and wallfilm interior temperature for neat iso-octane for NU-Le model

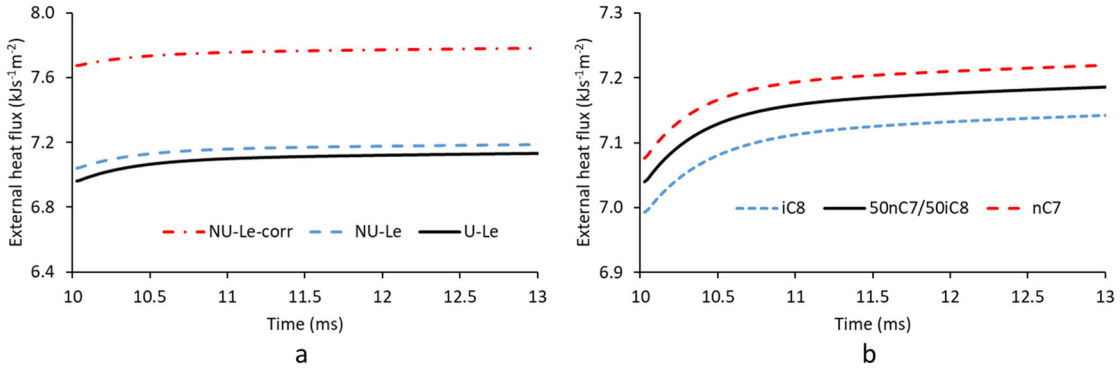

Figure 52: a) External heat flux of the 50nC7/50iC8 blend, b) External heat flux for comparison for NU-Le model

Figure 53 shows the evaporation rate comparison for nC7, iC8 and 50nC7/50iC8 cases for NU-Le model. Evaporation rate is calculated based on the energy balance and phase equilibrium at the liquid-vapor interface and is mainly governed by the wallfilm surface temperature. From the initial temperatures of wall, wallfilm interior, and ambient gas, the wallfilm surface temperature decreases due to heat loss to the wall, and the evaporation rate at the wallfilm surface also decreases eventually attaining a steady state value. It is seen that the evaporation rate profile of 50nC7/50iC8 case lies between the two neat liquid cases, but closer towards nC7 case. This behavior is consistent with the pattern of the wallfilm surface temperature, as shown in **Table 8.**

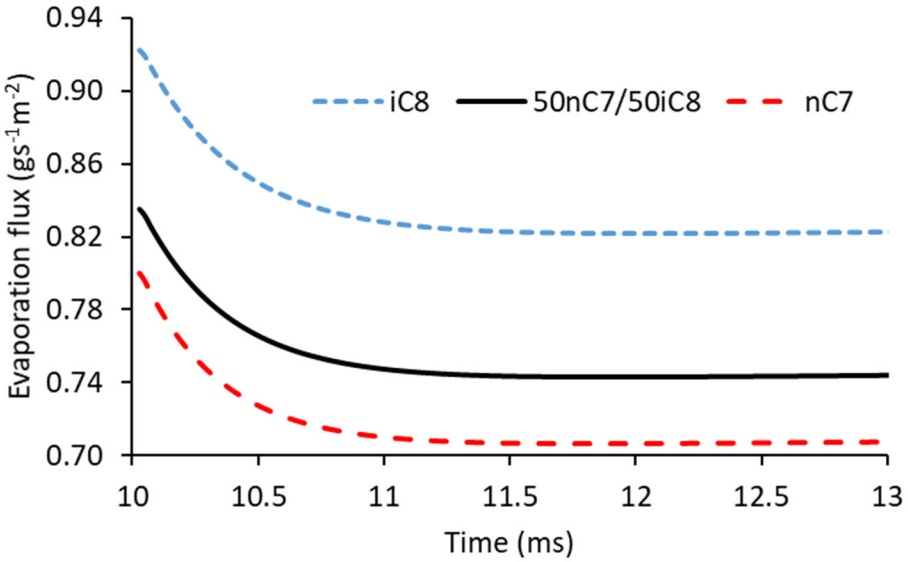

Figure 53: Evaporation flux variation for NU-Le model

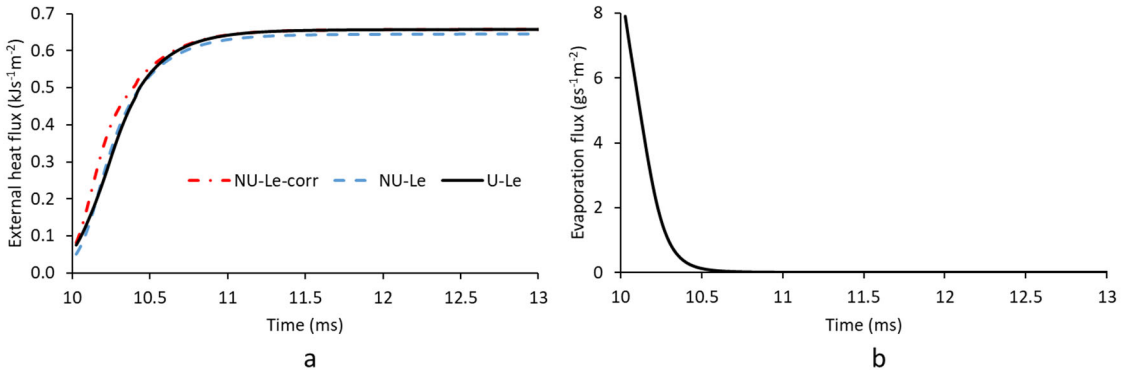

Figure 54: a) External heat flux for tetradecane, b) Evaporation flux of tetradecane for NU-Le model

For the study of heavy alkanes, n-tetradecane ($nC_{14}H_{30}$) was chosen. The case is referred as C14 from here on. Initial wallfilm interior temperature T_f was chosen as 540 K to encompass a wide Lewis number variation, and the wall temperature T_w was kept constant at 340 K. The wall temperature was increased from 295 K (used for nC7, iC8, and 50nC7/50iC8) to 340 K for C14 to enhance evaporation rate to a noticeable level. The saturation temperature of n-tetradecane for this condition is 558.95 K. **Figure 54 (a)** shows that external heat fluxes for various models for C14 case. Initially the external heat flux is very low, although the wallfilm interior temperature is close to the boiling condition. **Figure 54 (b)** shows the evaporation flux variation with time. The film initially being close to boiling condition (high wallfilm surface temperature), has a large evaporation flux m_0, causing the exponential term $e^{m_0 f(\eta)}$ in the denominator of the external heat flux Q_o expression to be large. In addition, the temperature difference between ambient and film is only 60 K, which limits the external heat flux. Most of the latent heat for evaporation comes from the film, initially when the external heat flux is low. With time, as the film loses heat through the cooler wall, its temperature starts decreasing. The ambient temperature remains

close to the initial value of 600 K due to the large heat capacity of the film containing computational cell. This leads to increasing temperature differential between the ambient and wallfilm surface, thus increasing heat flux (**Figure 54 (a)**). **Figure 55 (a)** shows the variation of Lewis number in the thermal boundary layer. During the rapidly increasing heat flux phase, Lewis number also changes rapidly from 1.07 to a steady state value of 4.76. The difference among the models is also the greatest during this transition to steady state. **Figure 55 (b)** shows the variation of external heat flux vs Le. Comparing predictions by U-Le (black) and NU-Le-corr (red-dot-dash) models clearly shows the effect of Lewis number on external heat flux. The maximum difference was observed at a Lewis number of 2.86, where Nu-Le-corr model predicts 32 % higher heat flux compared to U-Le model (which neglects Lewis number effect). Close to unity Lewis number difference between the curves decreases, until they match at unity Lewis number. After Lewis number of 2.86, the difference in heat flux between NU-Le-corr and U-Le model starts decreasing. At 13 ms, the external heat fluxes by NU-Le-corr and U-Le models were 1.84 % and 1.63 % higher than NU-Le model, respectively. The comparison of NU-Le-corr with NU-Le curve shows that the importance of the simplifying assumptions made in the derivations also varies with Lewis number. These assumptions have more consequences at mid-range Lewis numbers.

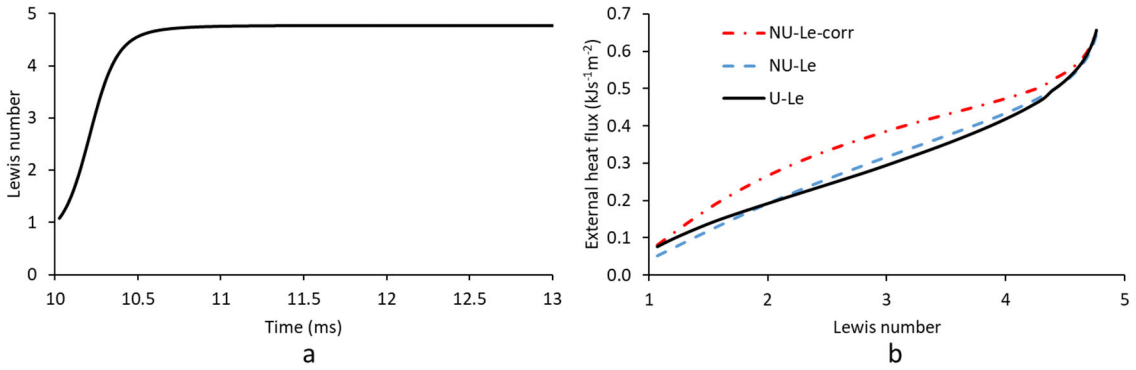

Figure 55: a) Lewis number variation of tetradecane for NU-Le model, b) External heat flux for tetradecane

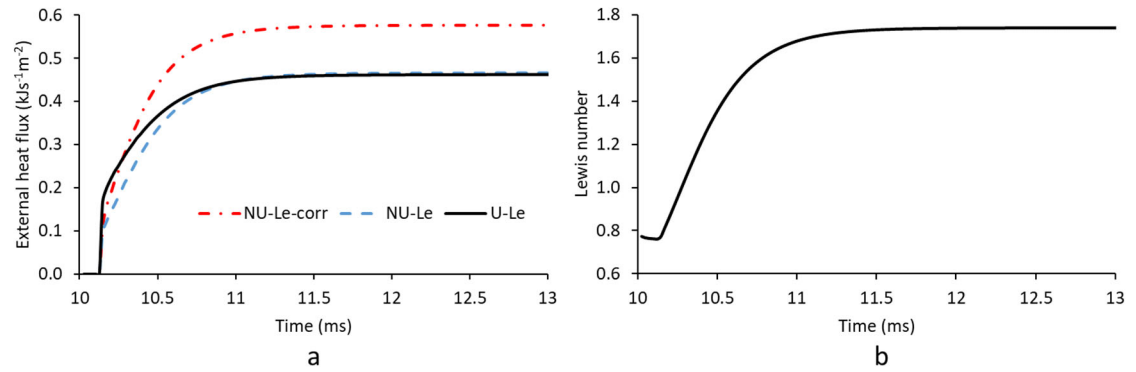

Figure 56: a) External heat flux for flash boiling of neat n-heptane, b) Lewis number variation for flash boiling of neat n-heptane

Neat n-heptane flash boiling case was also simulated. Initial wallfilm interior temperature of 420 K (saturation temperature 396.46 K) with wall temperature of 340 K was used. **Figure 56 (a)** shows the external heat flux for different models. Transient Lewis number variation is shown in **Figure 56 (b)**. Under the conditions considered, Le numbers of the n-heptane/air gas mixtures at 10 ms is smaller than unity. The mixture Le number initially decreases while the film is superheated (note that the wallfilm surface temperature is fixed at the boiling temperature) during the flash boiling state, and then increases to the steady

state value of 1.74 in the normal evaporation condition. All the models (NU-Le, U-Le, NU-Le-corr) show very small external heat flux when the wall film is in superheated state (up to 10.13 ms). This is due to the large value of the exponential term $e^{m_0 f(\eta)}$, caused due to the large flash boiling evaporation rates, which is shown in **Figure 57 (a) & (b)** for NU-Le model. **Figure 58** shows the variation of wallfilm surface, wallfilm interior, and saturation temperatures with time. The wallfilm surface temperature equals the saturation temperature in the flash boiling state which lasts up to 10.13 ms. Note that, due to a slight increase of chamber pressure caused by the flash boiling process, the saturation temperature is seen to slightly increase during the flash boiling period (**Figure 58 (b)**). The wallfilm interior temperature decreases from 420 K initially to saturation temperature of 396.46 K. Once entering the normal evaporation conditions, the wallfilm surface and wallfilm interior temperatures eventually reach steady state value close to the wall temperature of 340 K.

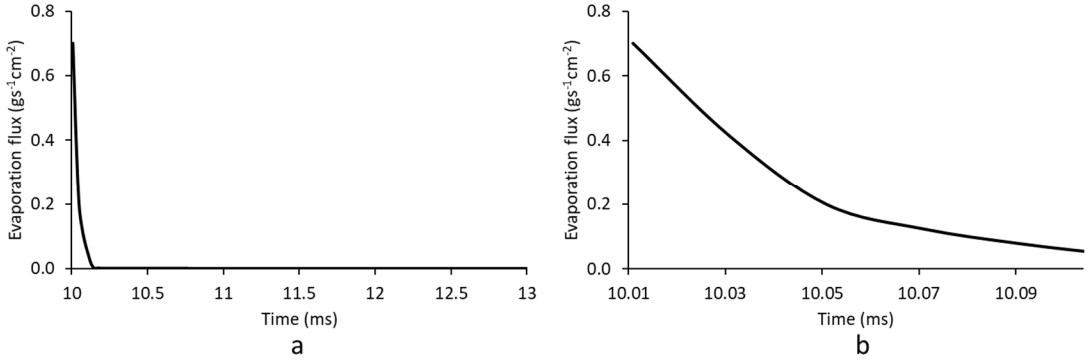

Figure 57: a) Evaporation flux of neat n-heptane flash boiling for NU-Le model, b) zoomed in view of (a)

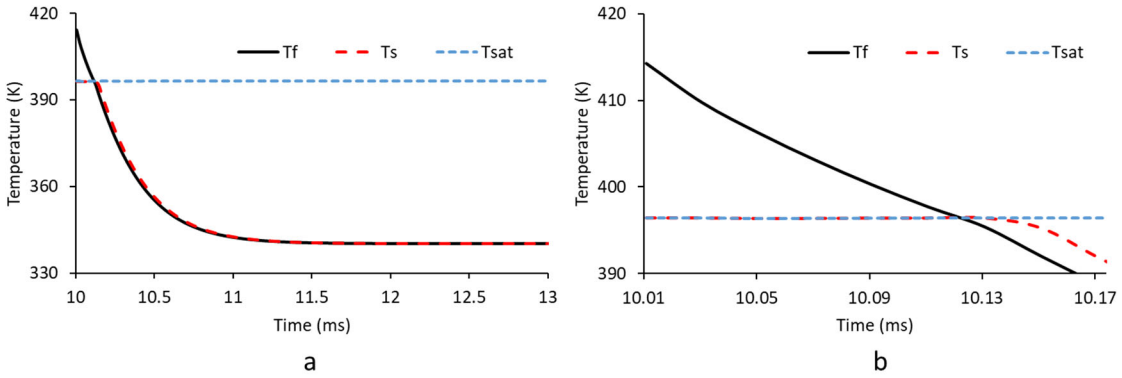

Figure 58: a) Wallfilm interior temperature (T_f), wallfilm surface temperature (T_s), saturation temperature (T_{sat}) variation for flash boiling of neat n-heptane, b) zoomed in view of (a)

4 Conclusions

4.1 Pre-ignition

In the present study, pre-ignition mechanism was investigated. In order to simulate the generation and ignition behavior of lube-oil drops, various sub-models were developed and implemented to the CFD code, including an inter-code-communication feature. The predicted drop motion and ignition were well validated against experiment data of single drop injection. Then, further simulations were performed to identify the factors which govern lube-oil drop ignition in a CVCC. Additionally, a model for snapping and rezoning of refined cells in moving grids was developed to be combined with the SPIC model and implemented into an in-house CFD code. An oil film stripping model was developed including oil film dynamics on the cylinder walls in a marine natural gas engine. The effects of variation of parameters such as initial film thickness and initial film velocity on the probability of stripping were discussed. Finally, after lube oil drops are stripped, the SPIC model was applied and factors affecting pre-ignition of oil drops were studied. The following conclusion/recommendations regarding lube oil stripping and pre-ignition and its prevention can be drawn.

1) The mechanism of pre-ignition occurring in a gas-engine could be identified though the present model to describe the combined processes of lube oil dynamics, stripping, two-phase motion and phase change, and the reaction chemistry of localized mixtures.

2) Stripping from lubricating oil film layers into the combustion chamber is a rare event and does not occur for normal/designed film thicknesses.

3) For stripping condition to be satisfied, i.e., critical angle less than $\frac{\pi}{2}$ radians in the present study, an initial film thickness required to be greater than190 μm with an initial film velocity of 80 cm/s or greater.

4) Once oil drops are stripped, the local mixture equivalence ratio in a refined-cell should meet a threshold in order to drive the pre-ignition process. Higher local equivalence ratio can occur when the oil drop stays stationary or moves at very low velocity in a high temperature region (e.g., the engine core) for a long time. Thus, combustion chamber must be free of hot spots to reduce the probability of pre-ignition.

5) Oil drops moving quickly through the chamber are not likely to cause pre-ignition as the equivalence ratio of local parent/refined cell mixtures stays low, even though the evaporation rates in those cells increase due to higher relative velocities between the ambient gas and the drops.

4.2 Wall film evaporation

Analytical expressions for heat fluxes to determine evaporation rate of multi-component liquid film were derived for unity and non-unity Lewis number conditions. The performance of the developed models was demonstrated for single (light and heavy alkanes) and multi-component wallfilms under the conditions of normal evaporation and flash boiling. NU-Le-corr model successfully predicts the effect of variable Le number in the evaporation process. The difference of predicted external heat flux between the non-unity Le models (NU-Le and NU-le-corr) and the unity Le model (U-Le) is inversely proportional to the Lewis number. Thus, the phase change predictions by models based on

unity Lewis number assumption become invalid, in particular, under low Lewis number conditions.

5 Future Work

5.1 Pre-ignition

In the present work, the physical properties of lube oil are modeled as n-heneicosane ($nC_{21}H_{44}$). However, the real composition of lube oil includes various additives (used for modifying properties) along with the base oil. Various literatures have shown that these additives affect pre-ignition behavior. Among additives, Calcium and sodium additives were shown to promote Low speed preignition (LSPI) under some conditions [53]. On the other hand, additives such as ZnDTp and MoDTC were found to reduce LSPI [12, 53]. The effect of such additives must be incorporated in the reaction mechanism. This needs to be investigated in the future.

As lube oil in engines age, it results in composition change due to oil degradation. Oxidation is the primary mechanism of oil degradation. It happens after depletion of antioxidant additives (used to prevent oil oxidation) present in the oil. During oxidative degradation phase, the formation of polar compounds such as ketones, alcohols, carboxylic acids and esters take place. This change in composition as a function of time (ageing) and its effect on pre-ignition needs to be studied further.

At higher loads, due to higher in-cylinder gas temperatures, there is increased NOx production which can cause increase in NO_2 in engine oil [54]. Kim et. al [55] also showed that oil nitration occurs in gasoline engines before oil oxidation. Lee et. al [56] showed there was oxidation for the lubricant in the piston top ring area and oil degradation was a function of load. Based on these results Spitter et al [57] have hypothesized the nitration

of lubricant oil effect on pre-ignition by running with RON 70 fuel blended with 6.5 % of nitro methane CH_3NO_2. They observed significantly higher pre-ignition. The methodology of incorporating the effect of oil nitration on the lube oil reactivity is to be further researched.

5.2 Wall film evaporation

The analytical expression for external heat flux from ambient surroundings to the wallfilm-gas interface was derived in the present work. Currently the wallfim temperature distribution along its height is modeled to be piecewise linear and its species concentration is assumed constant. To improve accuracy of the simulation, the wallfilm domain can be discretized and the temperature and species distribution can be obtained by solving the energy and mass (species) conservation equations. The wallfilm liquid phase can further be coupled with the solid wall by solving for the solid thermal field. Thus, all three phases namely gas, liquid and solid phases can be coupled.

References

1. Thomson, H., J.J. Corbett, and J.J. Winebrake, *Natural gas as a marine fuel.* Energy Policy, 2015. **87**: p. 153-167.
2. Burel, F., R. Taccani, and N. Zuliani, *Improving sustainability of maritime transport through utilization of Liquefied Natural Gas (LNG) for propulsion.* Energy, 2013. **57**: p. 412-420.
3. Jatana, G.S., et al., *Fuel property effects on low-speed pre-ignition.* Fuel, 2018. **230**: p. 474-482.
4. Zahdeh, A., et al., *Fundamental Approach to Investigate Pre-Ignition in Boosted SI Engines*. 2011, SAE International.
5. Gerendas, M. and S. Wittig, *Experimental and Numerical Investigation on the Evaporation of Shear-Driven Multicomponent Liquid Wall Films.* Journal of Engineering for Gas Turbines and Power, 2001. **123**(3): p. 580-588.
6. Hong, K., S.H. Lee, and H.S. Ryou, *Modelling of Wall Films Formed by Impinging Diesel Sprays.* SAE Transactions, 2001. **110**: p. 2031-2039.
7. Rosskamp, H., M. Willmann, and S. Wittig, *Heat up and evaporation of shear driven liquid wall films in hot turbulent air flow.* International Journal of Heat and Fluid Flow, 1998. **19**(2): p. 167-172.
8. Stanton, D.W., et al., *Influence of Spray-Wall Interaction and Fuel Films on Cold Starting in Direct Injection Diesel Engines.* SAE Transactions, 1998. **107**: p. 1540-1563.

9. Brown, M.A., H. McCann, and D.M. Thompson, *Characterization of the Oil Film Behaviour Between the Liner and Piston of a Heavy-Duty Diesel Engine*. 1993, SAE International.

10. Hashmi, A.A., et al. *Experimental Investigation of Lubrication Oil Film Dynamics in a Typical Aero-Engine Bearing Chamber Environment*. in *ASME 2011 Turbo Expo: Turbine Technical Conference and Exposition*. 2011.

11. Ullal, A., et al., *Numerical investigation of oil droplet combustion using single particle ignition cell model.* International Journal of Engine Research, 2021. **22**(5): p. 1465-1483.

12. Takeuchi, K., et al., *Investigation of Engine Oil Effect on Abnormal Combustion in Turbocharged Direct Injection - Spark Ignition Engines*. 2012, SAE International.

13. Fujimoto, K., et al., *Engine Oil Development for Preventing Pre-Ignition in Turbocharged Gasoline Engine.* SAE International Journal of Fuels and Lubricants, 2014. **7**(3): p. 869-874.

14. Park, S. and J.B. Ghandhi, *Fuel Film Temperature and Thickness Measurements on the Piston Crown of a Direct-Injection Spark-Ignition Engine*. 2005, SAE International.

15. Kuboyama, T., Y. Moriyoshi, and K. Morikawa, *Visualization and Analysis of LSPI Mechanism Caused by Oil Droplet, Particle and Deposit in Highly Boosted SI Combustion in Low Speed Range.* SAE International Journal of Engines, 2015. **8**(2): p. 529-537.

16. Amann, M., D. Mehta, and T. Alger, *Engine Operating Condition and Gasoline Fuel Composition Effects on Low-Speed Pre-Ignition in High-Performance Spark Ignited Gasoline Engines.* SAE International Journal of Engines, 2011. **4**(1): p. 274-285.

17. Ohtomo, M., et al., *Pre-Ignition of Gasoline-Air Mixture Triggered by a Lubricant Oil Droplet.* SAE International Journal of Fuels and Lubricants, 2014. **7**(3): p. 673-682.

18. Lauer, T., et al., *A Comprehensive Simulation Approach to Irregular Combustion*. 2014, SAE International.

19. Nishad, K.P., A. Sadiki, and J. Janicka, *A Comprehensive Modeling and Simulation of Gasoline Direct Injection using KIVA-4 code*. 2011, SAE International.

20. Ullal, A. and Y. Ra, *Analytical model for multicomponent wall film evaporation with non-unity Lewis number.* International Journal of Heat and Mass Transfer, 2021. **176**: p. 121485.

21. Haworth, S.T.a.D.C., *An Introduction to Combustion: Concepts and Applications*. 4th ed. 2021.

22. O'Rourke, P.J. and A.A. Amsden, *A Particle Numerical Model for Wall Film Dynamics in Port-Injected Engines*. 1996, SAE International.

23. O'Rourke, P.J. and A.A. Amsden, *A Spray/Wall Interaction Submodel for the KIVA-3 Wall Film Model.* SAE Transactions, 2000. **109**: p. 281-298.

24. Zeng, Y. and C.-F. Lee, *Multicomponent-Fuel Film-Vaporization Model for Multidimensional Computations.* Journal of Propulsion and Power, 2000. **16**(6): p. 964-973.

25. Lee, C.-f.F., W.L. Cheng, and D. Wang, *Finite diffusion wall film evaporation model for engine simulations using continuous thermodynamics.* Proceedings of the Combustion Institute, 2009. **32**(2): p. 2801-2808.

26. Yan, Y.a., et al., *A one-dimensional unsteady wall film evaporation model.* International Journal of Heat and Mass Transfer, 2015. **88**: p. 138-148.

27. Ra, Y. and R.D. Reitz, *A vaporization model for discrete multi-component fuel sprays.* International Journal of Multiphase Flow, 2009. **35**(2): p. 101-117.

28. Sazhin, S.S., O. Rybdylova, and C. Crua, *A mathematical model for heating and evaporation of a multi-component liquid film.* International Journal of Heat and Mass Transfer, 2018. **117**: p. 252-260.

29. Steeman, H.J., A. Janssens, and M. De Paepe, *On the applicability of the heat and mass transfer analogy in indoor air flows.* International Journal of Heat and Mass Transfer, 2009. **52**(5): p. 1431-1442.

30. Liye, S., et al., *A new approach to transient evaporating film heating modeling based on analytical temperature profiles for internal combustion engines.* International Journal of Heat and Mass Transfer, 2015. **81**: p. 465-469.

31. Liu, H., et al., *An analytical model of the heating and evaporation of bi-component wall film.* International Communications in Heat and Mass Transfer, 2019. **105**: p. 28-36.

32. Baniabedalruhman, A., *DYNAMIC MESHING AROUND FLUID-FLUID INTERFACES WITH APPLICATIONS TO DROPLET TRACKING IN CONTRACTION GEOMETRIES*, in *Department of Mathematical Sciences*. 2015, Michigan Technological University: Houghton.

33. Torres, D., P. J O'rourke, and A.A. Amsden, *Efficient multicomponent fuel algorithm*. Vol. 7. 2003. 66-86.

34. Weisstein, E.W. *Sphere-Sphere Intersection*. From MathWorld--A Wolfram Web Resource; Available from: https://mathworld.wolfram.com/Sphere-SphereIntersection.html.

35. Kee, R.J., F.M. Rupley, and J.A. Miller, *Chemkin-II: A Fortran chemical kinetics package for the analysis of gas-phase chemical kinetics*. 1989, ; Sandia National Labs., Livermore, CA (USA). p. Medium: X; Size: Pages: (127 p).

36. Fan, L., et al., *Modeling Fuel Preparation and Stratified Combustion in a Gasoline Direct Injection Engine*. 1999, SAE International.

37. Perini, F., et al., *An Efficient Level-Set Flame Propagation Model for Hybrid Unstructured Grids Using the G-Equation.* SAE International Journal of Engines, 2016. **9**(3): p. 1409-1424 %@ 1946-3944.

38. Ra, Y. and R.D. Reitz, *A combustion model for multi-component fuels using a physical surrogate group chemistry representation (PSGCR).* Combustion and Flame, 2015. **162**(10): p. 3456-3481.

39. Westbrook, C.K., et al., *A comprehensive detailed chemical kinetic reaction mechanism for combustion of n-alkane hydrocarbons from n-octane to n-hexadecane.* Combustion and Flame, 2009. **156**(1): p. 181-199.

40. Ra, Y., F. Chuahy, and S. Kokjohn, *Development and validation of a reduced reaction mechanism with a focus on diesel fuel/syngas co-oxidation.* Fuel, 2016. **185**: p. 663-683.

41. Torres, D.J. and M.F. Trujillo, *KIVA-4: An unstructured ALE code for compressible gas flow with sprays.* Journal of Computational Physics, 2006. **219**(2): p. 943-975.

42. Maroteaux, F., et al., *Liquid Film Atomization on Wall Edges—Separation Criterion and Droplets Formation Model.* Journal of Fluids Engineering, 2002. **124**(3): p. 565-575.

43. Friedrich, M.A., et al., *A Separation Criterion With Experimental Validation for Shear-Driven Films in Separated Flows.* Journal of Fluids Engineering, 2008. **130**(5).

44. Jiang, Y.K., et al., *3D EHD lubrication and wear for piston ring-cylinder liner on diesel engines.* International Journal of Automotive Technology, 2015. **16**(1): p. 1-15.

45. Zottin, W., P.V. Bacchin, and A.F. Garcia, *Numerical Simulation Study of Carbon Build-up and Oil Consumption in a Heavy Duty Diesel Engine.* SAE Int. J. Engines, 2012. **5**(3): p. 1477-1486.

46. Rahman, M.A. and M.Z. Saghir, *Thermodiffusion or Soret effect: Historical review.* International Journal of Heat and Mass Transfer, 2014. **73**: p. 693-705.

47. Ingle, S.E. and F.H. Horne, *The Dufour effect.* The Journal of Chemical Physics, 1973. **59**(11): p. 5882-5894.

48. Kreyszig, E., *Advanced engineering mathematics*. 1983: Fifth edition. New York : Wiley, [1983] ©1983.

49. Sirignano, W.A., *Fuel droplet vaporization and spray combustion theory.* Progress in Energy and Combustion Science, 1983. **9**(4): p. 291-322.

50. Tan, Z. and R.D. Reitz, *Modeling Ignition and Combustion in Spark-ignition Engines Using a Level Set Method*. 2003, SAE International.

51. Hessel, R.P., et al., *Gaseous Fuel Injection Modeling Using a Gaseous Sphere Injection Methodology*. 2006, SAE International.

52. Lu, X., et al., *Thermal analysis on piston of marine diesel engine.* Applied Thermal Engineering, 2013. **50**(1): p. 168-176.

53. Shibuya, M., et al., *Research on the Effect of Lubricant Oil and Fuel Properties on LSPI Occurrence in Boosted S. I. Engines*. 2016, SAE International.

54. Chamberlin, W.B., T.T. Curtis, and D.M. Smith, *Crankcase Lubricants for Natural Gas Transportation Applications.* SAE Transactions, 1996. **105**: p. 1340-1349.

55. Kim, J.-S., et al., *The Characteristics of Carbon Deposit Formation in Piston Top Ring Groove of Gasoline and Diesel Engine*. 1998, SAE International.

56. Lee, P.M., et al., *Extraction and tribological investigation of top piston ring zone oil from a gasoline engine.* Proceedings of the Institution of Mechanical Engineers, Part J: Journal of Engineering Tribology, 2006. **220**(3): p. 171-180.

57. Splitter, D., et al., *Fuel-Lubricant Interactions on the Propensity for Stochastic Pre-Ignition*. 2019, SAE International.

A Appendix: Calculation of $f(\eta)$ and Lewis number

A.1 Calculation of $f(\eta)$

Taking the definition of $f(\eta)$ from **Sec. 2.2.2**

$f(\eta) = \int_0^{\eta} \frac{\delta_m}{\rho D} d\eta$

Appling Taylor expansion to $f(\eta)$ around η=0 gives

$$f(\eta) = \int_0^{\eta=0} \frac{c_p \delta_t}{\lambda} + \frac{c_{p,0} \delta_t}{\lambda_0} \eta + \frac{\delta_t}{2\lambda_0} \left(c_{p,F} - c_{p,A}\right) \frac{dy_F(\eta = 0)}{d\eta} \eta^2 + R_3 \qquad \text{Aeq. 1}$$

where R_3 denotes higher order remaining terms. Since the analysis is limited within the boundary layer in the physical domain, i.e., $\eta \leq 1$, η_∞ is replaced with unity and the value of $f(\eta = 1)$ is approximated as

$$f(\eta = 1) = 0 + \frac{c_{p,0} \delta_t}{\lambda_0} + \frac{m_0 c_{p,0}}{2\lambda_0^2} \left(c_{p,F} - c_{p,A}\right) \frac{\left(y_{F,\infty} - y_{F,0}\right)}{e^{[m_0 f(\eta=1)]} - 1} {\delta_t}^2 \qquad \text{Aeq. 2}$$

Also, the exponential term in the denominator of the second term of the right-hand side of **Aeq. 2** can be approximated as

$$e^{m_o f(\eta=1)} \approx 1 + m_0 f(\eta = 1) + \kappa \qquad \text{Aeq. 3}$$

where κ is the constant to approximate the higher order remaining terms. Therefore, inserting **Aeq. 3** into **Aeq. 2** gives

$$f(\eta = 1) = \frac{c_{p,0} \delta_t}{\lambda_0} + \frac{m_0 c_{p,0}}{2\lambda_0^2} \left(c_{p,F} - c_{p,A}\right) \frac{\left(y_{F,\infty} - y_{F,0}\right)}{m_0 f(\eta = 1) + \kappa} {\delta_t}^2 \qquad \text{Aeq. 4}$$

Using a new form of the function defined in the physical domain, $g(\delta)$, to replace $f(\eta = 1)$ yields

$$g(\delta_t) = \frac{c_{p,0}}{\lambda_0} \delta_t + \frac{m_0 c_{p,0}}{2\lambda_0^2} \left(c_{p,F} - c_{p,A}\right) \frac{\left(y_{F,\infty} - y_{F,0}\right)}{m_0 g(\delta_t) + \kappa} {\delta_t}^2 \qquad \text{Aeq. 5}$$

Rearranging **Aeq. 5** gives

$$g^2(\delta_t) + \left(\frac{\kappa}{m_0} - \frac{c_{p,0}}{\lambda_0}\delta_t\right) g(\delta_t) - \left[\frac{\kappa}{m_0}\frac{c_{p,0}}{\lambda_0}\delta_t + \frac{c_{p,0}}{2\lambda_0^2}\left(c_{p,F} - c_{p,A}\right)\left(y_{F,\infty} - y_{F,0}\right){\delta_t}^2\right] = 0 \quad \text{Aeq. 6}$$

Solving **Aeq. 6** and considering the positive solution gives the functional form of $g(\delta)$ as

$$g(\delta_t) = \frac{c_{p,0}}{2}\frac{\delta_t}{\lambda_0}\left[1 + \sqrt{1 + 2\frac{\left(c_{p,F} - c_{p,A}\right)}{c_{p,0}}\left(y_{F,\infty} - y_{F,0}\right) + \frac{2\kappa}{m_0 c_{p,0}}\left(\frac{\lambda_0}{\delta_t}\right) + \frac{\kappa^2}{m_0^2 c_{p,0}^2}\left(\frac{\lambda_0}{\delta_t}\right)^2}\right] - \frac{\kappa}{2m_0} \quad \text{Aeq. 7}$$

For $g(\delta_t)$ we have 3 conditions to be satisfied, as below.

$$g(\delta_t) > 0 \quad \text{Aeq. 8}$$

$$\left(\frac{\kappa}{m_0} - \frac{c_{p,0}}{\lambda_0}\delta_t\right)^2 + 4\left[\frac{\kappa}{m_0}\frac{c_{p,0}}{\lambda_0}\delta_t + \frac{c_{p,0}}{2\lambda_0^2}\left(c_{p,F} - c_{p,A}\right)\left(y_{F,\infty} - y_{F,0}\right){\delta_t}^2\right] \geq 0 \quad \text{Aeq. 9}$$

$$\kappa > 0 \quad \text{Aeq. 10}$$

Aeq. 9 is a quadratic equation of the form $ax^2 + bx + c$

where

$$a = 1, b = \left(\frac{\kappa}{m_0} - \frac{c_{p,0}}{\lambda_0}\delta_t\right), c = -\left[\frac{\kappa}{m_0}\frac{c_{p,0}}{\lambda_0}\delta_t + \frac{c_{p,0}}{2\lambda_0^2}\left(c_{p,F} - c_{p,A}\right)\left(y_{F,\infty} - y_{F,0}\right){\delta_t}^2\right]$$

Thus, from the condition in **Aeq. 10** the solution has the form

$$\frac{-b \pm \sqrt{b^2 - 4ac}}{2a} > 0$$

$$-b \pm \sqrt{b^2 - 4ac} > 0$$

$$-b > \mp\sqrt{b^2 - 4ac}$$

$$b < \mp\sqrt{b^2 - 4ac}$$

The limiting solution is

$$b < -\sqrt{b^2 - 4ac}$$

Assuming, b is negative, then

$$ac > 0$$

Substituting for a and c and simplifying the following condition is obtained

$$-\left[\frac{\kappa}{m_0}\frac{c_{p,0}}{\lambda_0}\delta_t + \frac{c_{p,0}}{2\lambda_0^2}\left(c_{p,F} - c_{p,A}\right)\left(y_{F,\infty} - y_{F,0}\right){\delta_t}^2\right] > 0$$

$$\left[\frac{\kappa}{m_0}\frac{c_{p,0}}{\lambda_0}\delta_t + \frac{c_{p,0}}{2\lambda_0^2}\left(c_{p,F} - c_{p,A}\right)\left(y_{F,\infty} - y_{F,0}\right){\delta_t}^2\right] < 0$$

$$\frac{\kappa}{m_0} < -\frac{\left(c_{p,F} - c_{p,A}\right)\left(y_{F,\infty} - y_{F,0}\right)\delta_t}{2\lambda_0}$$

$$\kappa < -\frac{\left(c_{p,F} - c_{p,A}\right)\left(y_{F,\infty} - y_{F,0}\right)m_0\delta_t}{2\lambda_0}$$

$$\kappa < \frac{\left(c_{p,F} - c_{p,A}\right)\left(y_{F,0} - y_{F,\infty}\right)m_0\delta_t}{2\lambda_0}$$

An appropriate constant κ is determined to satisfy the above condition and used in the calculation using the model.

A.2 Calculation of Lewis number

For NU-Le model, the concentration boundary layer δ_m is evaluated from the thermal boundary layer δ_t and the Lewis number Le using the approximate relation as

$$\delta_m \approx \frac{\delta_t}{Le}$$

The Lewis number within the boundary layer is evaluated at $\eta = 0.333$ (**Figure 18**). If the properties at $\eta = 0.333$ is denoted by the suffix mix, then the Lewis number Le is given by

$$Le = \frac{\lambda_{mix}}{\rho_{mix} c_{p,mix} D_{mix,a}}$$

Where for m multi component liquid species and n total species, these properties evaluated at temperature $T_{mix} = \frac{2}{3}T_s + \frac{1}{3}T_\infty$ are

$$\lambda_{mix} = x_f \lambda_f + x_a \lambda_a$$

$$\rho_{mix} = x_f \rho_f + x_a \rho_a$$

$$c_{p,mix} = y_f c_{p,f} + y_a c_{p,a}$$

$$D_{mix,a} = \sum_1^m x_i D_{i,a}$$

$$x_f = \sum_1^m x_i \ , \ x_a = 1 - x_f \ , \ y_f = \sum_1^m y_i \ , \ y_a = 1 - y_f$$

$$y_i = \frac{2}{3} y_{i,s} + \frac{1}{3} y_{i,\infty} \ , \ x_i = \frac{2}{3} x_{i,s} + \frac{1}{3} x_{i,\infty}$$

$$\lambda_f = \sum_1^m x_i \lambda_i \ , \ \lambda_a = \sum_{m+1}^n x_i \lambda_i$$

$$c_{p,f} = \sum_1^m y_i c_{p,i}$$

$$\rho_f = \frac{P}{T_{mix} R_f} \ , \ \rho_a = \frac{P}{T_{mix} R_a}$$

$R_f = \frac{R_u}{\sum_1^m x_i MW_i}$, $R_a = \frac{R_u}{\sum_{m+1}^n x_i MW_i}$

where $T_s, T_\infty, D_{i,a}, x_i, y_i, y_{i,s}, y_{i,\infty}, x_{i,s}, x_{i,\infty}, \lambda_i, c_{p,i}, c_{p,a}, P, R_u, MW_i$ are the wallfilm surface temperature, free stream temperature, binary diffusion coefficient of liquid species i with respect to air, mole fraction of species i, mass fraction of species i, wallfilm surface mass fraction of species i, free stream mass fraction of species i, wallfilm surface mole fraction of species i, free stream mole fraction of species i, thermal conductivity of species i, specific heat capacity of air, free stream pressure, universal gas constant, molecular weight of species i, respectively.